UNIVERSITY OF COPENHAGEN
FACULTY OF SCIENCE

# PhD Thesis

Meghana Killi

# Morphology and Spectroscopy of High-redshift Galaxies

Galaxy evolution through multi-wavelength observations

Supervisor: Darach Watson

Submitted on: 25 September 2023

This thesis has been submitted to the PhD School of The Faculty of Science, University of Copenhagen.

DAWN

COSMIC DAWN CENTER

# Abstract

Recent results from *JWST* and the Atacama Large Millimeter-submillimeter Array (ALMA) have shown that the first galaxies in the Universe began forming within 500 Myr after the Big Bang. This means that over 13 billion years have passed since the first appearance of luminous objects. The past few decades in astronomy have outlined the general process by which modern galaxies like our Milky Way evolved from primordial structures - dark matter coalesced into halos where normal matter formed stars and galaxies, which then merged to create more massive structures. However, much of the detail still remains elusive - why, how, and when did primordial galaxies make their transformation into their modern counterparts? What were the conditions like within and without these galaxies that led them to evolve in this specific way? Which of the objects we observe in the distant Universe, i.e., in our distant past, were the ancestors of modern objects, including spiral galaxies like our Milky Way, dwarf galaxies, globular clusters, quiescent and elliptical galaxies, and the supermassive black holes at the centres of galaxies? Which of them played the biggest role in the major events in the history of our Universe such as reionisation? Are there objects that we have yet to discover that might completely change our understanding of how galaxies evolved?

The aim of this thesis is to attempt to answer these questions. I begin with an overview of our current understanding of the timeline and physics of galaxy evolution, along with relevant observational techniques and their limitations.

I then present our study of the physics of an early galaxy at $z \sim 7.13$ ($\sim$ 800 million years after the Big Bang). Using emission from the metal-enriched gas in the far-infrared, specifically from the [C II] 158μm, [N II] 122μm, [O III] 52 and 88μm lines, along with the underlying continuum emission from the dust, I estimate the metallicity, strength of ionisation, and gas density in the inter-stellar medium (ISM) of this galaxy. This analysis, the first of its kind at $z > 7$, provides a rare glimpse into the ISM of an early galaxy, and provides constraints on when it may have formed. By extension, this provides a timeline for the formation of the first galaxies in the Universe, and their dust and gas properties.

Next, I analyse the internal structure of $\sim$ 50 star-forming galaxies between cosmic noon and reionisation ($z \sim$ 4–6). I once again use the

[C II] 158μm line and emission from the dust continuum, along with the emission in the ultraviolet (UV) and optical. I estimate the centroids of these four emissions and their offsets relative to each other, and find that around $\sim 25\%$ of the galaxies in the study display significant offsets. As the [C II] emission arises from the gas in the galaxy, continuum from the dust, and UV and optical emission directly from stars, an offset between the emissions implies an offset between the gas, dust, and stars in the galaxies, which reveals the conditions within the ISM such as the strength of feedback from stellar radiation, the distribution of dust across the galaxies, and also the general morphological structure of galaxies in this epoch.

Later, I investigate the nature of an enigmatic object at $z \sim 4.53$. The spectrum includes features from a star-forming galaxy, and also from a supermassive black hole i.e., an active galactic nucleus (AGN). This object seems to be one among a growing list of a new class of objects called little red dots that were unknown prior to *JWST*. While a galaxy with an AGN is nothing new, pre-*JWST* observations used to show either a star-formation dominated or an AGN-dominated galaxy. These objects, however, seem to be caught exactly in between these two phases, which means that we may be witnessing the earliest stages of supermassive black hole formation, i.e., the progenitors of the AGN in the local Universe.

Finally, I discuss the implications of these findings in the larger astronomical context, and suggest future prospects of expanding the studies to gain an even more detailed understanding of galaxy evolution.

# Resumé

Nye resultater fra *JWST* og Atacama Large Millimeter-submillimeter Array (ALMA) har vist, at de første galakser i Universet begyndte at dannes inden for 500 Myr efter Big Bang. Det betyder, at der er gået over 13 milliarder år, siden de første lysende objekter dukkede op. De sidste par årtier inden for astronomi har skitseret den generelle proces, hvorved nutidige galakser som vores Mælkevej udviklede sig fra oprindelige strukturer — mørkt stof samlede sig i haloer, hvor almindeligt stof dannede stjerner og galakser, som derefter smeltede sammen for at skabe tungere strukturer. Endnu er mange detaljer dog uhåndgribelige — hvorfor, hvordan og hvornår forvandlede de oprindelige galakser deres moderne modstykker? Hvordan var forholdene i og udenfor disse galakser, der fik dem til at udvikle sig på denne specifikke måde? Hvilke af de objekter, vi observerer i det fjerne Univers, dvs. i vores fjerne fortid, var forfædre til moderne objekter, herunder spiralgalakser som vores Mælkevej, dværggalakser, kuglehobe, ikke-stjernedannende og elliptiske galakser og de supertunge sorte huller i centrum af galakser? Hvilke af dem spillede den største rolle i de store begivenheder i vores Univers' historie, som f.eks. reionisering? Er der objekter, som vi endnu ikke har opdaget, som fuldstændigt kan ændre vores forståelse af, hvordan galakser udviklede sig?

Formålet med denne afhandling er at forsøge at besvare disse spørgsmål. Jeg begynder med et overblik over vores nuværende forståelse af galakseudviklingens tidslinje og fysik sammen med relevante observationsteknikker og deres begrænsninger.

Jeg præsenterer derefter vores undersøgelse af fysikken i en tidlig galakse ved $z \sim 7.13$ ($\sim$ 800 millioner år efter Big Bang). Ved at bruge emission fra den metalberigede gas i det fjern-infrarøde, specifikt fra [C II] 158μm, [N II] 122μm, [O III] 52 and 88μm linjer, sammen med den underliggende kontinuums-emission fra støvet, estimerer jeg metalliciteten, ioniseringsstyrken og gasdensiteten i det interstellare medium (ISM) i denne galakse. Denne analyse, den første af sin slags ved $z > 7$, giver et sjældent indblik i ISM'et i en tidlig galakse og sætter grænser for, hvornår den kan være dannet. I forlængelse heraf giver dette en tidslinje for dannelsen af de første galakser i Universet og deres støv- og gasegenskaber.

Dernæst analyserer jeg den indre struktur af $\sim$ 50 stjernedannende galakser mellem "kosmisk middag" og reionisering ($z \sim$ 4–6). Jeg bruger

igen [C II] 158μm linjen og emission fra støvkontinuet, sammen med emissionen i ultraviolet (UV) og optisk. Jeg estimerer centroiderne for disse fire emissioner og deres Doppler-forskydninger i forhold til hinanden og finder, at omkring $\sim 25\%$ af galakserne i undersøgelsen viser betydelige forskydninger. Da [C II]-emissionen kommer fra gassen i galaksen, kontinuet fra støvet og UV og optisk emission direkte fra stjerner, indebærer en forskydning af emissionen en forskydning mellem gassen, støvet og stjernerne i galakserne, hvilket afslører forholdene inden for ISM'et, såsom styrken af feedback fra stjernestråling, fordelingen af støv på tværs af galakserne og også den generelle morfologiske struktur af galakser i denne epoke.

Senere undersøger jeg et gådefuldt objekt ved $z \sim 4.53$. Spektret omfatter træk fra en stjernedannende galakse og også fra et supertungt sort hul, dvs. en aktiv galaksekerne (AGN). Dette objekt ser ud til at være ét blandt en voksende liste af en ny klasse af objekter kaldet "små røde prikker", som var ukendte før *JWST*. Selvom en galakse med en AGN ikke er noget nyt, plejede præ-*JWST*-observationer at vise enten en stjernedannelsesdomineret eller en AGN-domineret galakse. Disse objekter ser dog ud til at være fanget nøjagtigt mellem disse to faser, hvilket betyder, at vi kan være vidne til de tidligste stadier af supertunge sorte hullers dannelse, dvs. forfædre til AGN i det lokale Univers.

Til sidst diskuterer jeg implikationerne af disse fund i den større astronomiske kontekst og foreslår fremtidige udsigter til at udvide undersøgelserne for at få en endnu mere detaljeret forståelse af galakseudviklingen.

# Contents

# List of Figures

# List of Tables

# Part I

# Introduction

# Chapter 1

# Galaxy Evolution

The search for galaxies outside our own began with the discovery of "island universes" by Immanuel Kant in the mid 1700s, followed by Lord Rosse's spiral nebulae in the mid 1800s. Then came the Shapley-Curtis debate of 1920 and the confirmation of the extra-galactic nature of these objects by Edwin Hubble (Hubble & P., 1925). Today there are billions of known galaxies, and their numbers are ever increasing with the advent of *JWST*. To date, the most distant galaxy with spectroscopic confirmation is JADES-GS+53.14988-27.77650 at a redshift ($z$) of $13.20^{+0.04}_{-0.07}$ (Curtis-Lake et al. 2023; although there are candidates with photometric redshift as high as 16 from Donnan et al. 2022). This corresponds to a mere $\sim 300$ Myrs after the Big Bang (Aghanim et al., 2020), which leaves over 13 Gyrs of galaxy evolution to produce the modern (cosmic noon and thereafter; see Sec. 1.1) galaxies we see in the local Universe.

With each new redshift record (e.g. Hu et al., 2002; Oesch et al., 2016) came the realisation that galaxies in the Universe at high-$z$ were increasingly different than those at $z \sim 0$, including morphology (Conselice, 2014), ionisation state (Katz et al., 2023; Tang et al., 2023), and chemical composition (Maiolino & Mannucci, 2019). Yet, these objects are the progenitors of the Milky Way (e.g. Salvadori et al., 2010; Graziani et al., 2017; Papovich et al., 2016) and other modern objects in the local Universe (e.g. Yajima et al., 2012; Morishita et al., 2015; Hygate et al., 2023). Thus, they must have transformed over billions of years due to mergers (Romano et al., 2021), gas accretion and quenching (Noguchi, 2023; Sherman et al., 2020), cooling of the cosmic microwave background (CMB; Steinhardt et al. 2022), and dust and metal enrichment (Ramburuth-Hurt et al., 2023; Donevski et al., 2020). The exact timeline, processes, and reasons for this transformation are still not very well understood (e.g. Kewley et al., 2019; Förster Schreiber & Wuyts, 2020; Saintonge & Catinella, 2022; Robertson, 2022; Crain & Voort, 2023). For this reason, the study of the evolution of galaxies from the Big Bang to the present day has been a central theme of observational astronomy over the last century. In this section, I will provide an overview of the state-of-the-art of the study of

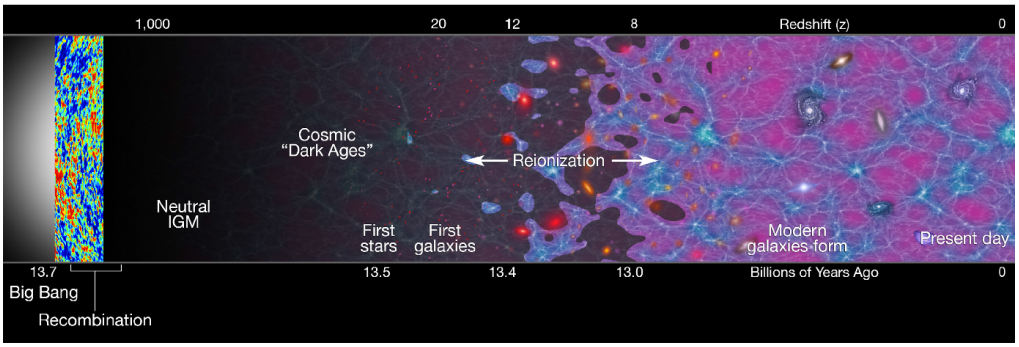


**Figure 1.1:** Timeline of evolution of the Universe from the Big Bang on the far left to the present day on the far right. The epoch of reionisation ($z \sim 6$–$20$) is indicated, along with the era of the first galaxies ($z > 10$) and the peak of modern galaxy formation, i.e., cosmic noon at ($z \sim 2$). Image taken from Gnedin et al. (2022).

galaxy evolution.

## 1.1 Timeline

The history of the Universe can be broadly divided into epochs or eras as shown in Fig. 1.1. After the Big Bang and recombination, the CMB was released at $z \sim 1090$ (Aghanim et al., 2020). Then followed the "Dark Ages" after which the the first so-called Population III (Pop III) stars (Bromm et al., 2002; Yoshida et al., 2008; Latif et al., 2022) began forming at $z > 20$, 200 Myrs after the Big Bang (Gnedin et al., 2022; Jeon et al., 2015). Stars, according to the ΛCDM model, then hierarchically assembled bottom-up into galaxies (Barkana & Loeb, 2001) at $z \gtrsim 15$ (Whitler et al., 2022). All these luminous objects produced ionising radiation, which ionised bubbles of gas around them (Furlanetto et al., 2004; Datta et al., 2007; Witstok et al., 2023b). Eventually, the bubbles coalesced until all the intergalactic medium was reionised. We do not know what the major contributor to reionisation was - galaxies or active galactic nuclei (AGN), although observations and models currently favour the former (e.g. Alvarez et al., 2012; Robertson et al., 2015; Kashino et al., 2023). The exact redshifts for the beginning and end of the formation/assembly of the first galaxies are still being researched, but this is believed to have occurred between $z \sim 12$–$6$ (e.g. Fan et al., 2006; McGreer et al., 2015; Chornock et al., 2014; Lu et al., 2022). The next major era in the history of the Universe is the Cosmic Noon at $z \sim 2$, where the bulk of the present Universe's stellar mass was assembled (Madau & Dickinson, 2014). For the purpose of this thesis, I will assign the name "Cosmic Morning" to the period between the end of reionisation and the beginning of cosmic noon, i.e., $z \sim 4$–$6$, where the processes driving modern galaxies were established.

### 1.1.1 Dust and metal enrichment

As the first stars and galaxies in the Universe formed out of pristine gas from the Big Bang with mostly H and He (Bromm & Loeb, 2003a; De Rossi & Bromm, 2017), the metallicity and dust content were near zero (Fumagalli et al., 2011). Stars then processed the gas through nuclear fusion, supernova explosions, and asymptotic giant branch (AGB) evolution, producing heavier elements that enriched the Universe with metals and dust (Pallottini et al., 2014; Corazza et al., 2022; Curti et al., 2022; Furlanetto & Loeb, 2003; Schneider et al., 2006; Cherchneff & Dwek, 2010; Marassi et al., 2015). The overall metallicity and dust content of galaxies thus steadily increases with decreasing redshift (Nakajima et al., 2023; Zavala et al., 2021). Although we do not yet know how early in the history of the Universe this enrichment occurs, FIR observations within the last decade have shown that there is already significant dust and metal enrichment by $z \sim 7$–8 (e.g. Watson et al., 2015; Venemans et al., 2017; Schouws et al., 2022b).

## 1.2 Baryon Cycle and Fundamental Physics

Let us now zoom in to focus on the physics of a single galaxy and the processes that occur within its interstellar medium (ISM). A galaxy interacts with its environment through the baryon cycle, as shown in the top panel of Fig. 1.2, accreting gas from the cosmic web and injecting processed, dust and metal-rich gas back into the circumgalactic and intergalactic media (CGM and IGM) through stellar feedback and outflows (Davé et al., 2019; Lilly et al., 2013; Ginolfi et al., 2020a). According to the "bathtub" model, the galaxy is in a quasi-steady state equilibrium, forming stars in proportion to its gas reservoir, which can be exhausted by outflows, and replenished by pristine gas accretion from the cosmic web (e.g. Bouché et al., 2010; Davé et al., 2011, 2012; Lilly et al., 2013; Dekel & Mandelker, 2014; Somerville & Davé, 2015; Dessauges-Zavadsky et al., 2020). Stellar/AGN feedback affect the rate at which gas flows in and out of the galaxy (Fluetsch et al. 2019; Veilleux et al. 2020; Zhu et al. 2023; see also Dekel et al. 2023). Availability of cold, molecular gas in turn affects how many stars can be formed, as also evidenced by the increasing star-formation rate (SFR) with increasing molecular gas content at high-$z$ (e.g. Scoville et al., 2016; Decarli et al., 2019b; Tacconi et al., 2020).

Within the ISM, there exist distinct regions: hot, ionised H II regions are in the immediate surroundings of stars, while cool, molecular $H_2$ gas lies around and outside the ionised pockets. In between these two regions lies the photo-dissociation region (PDR), with an onion structure of various species of metal ions and atoms, proceeding in the order of decreasing ionisation potential with increasing distance from the ionising source (Carilli

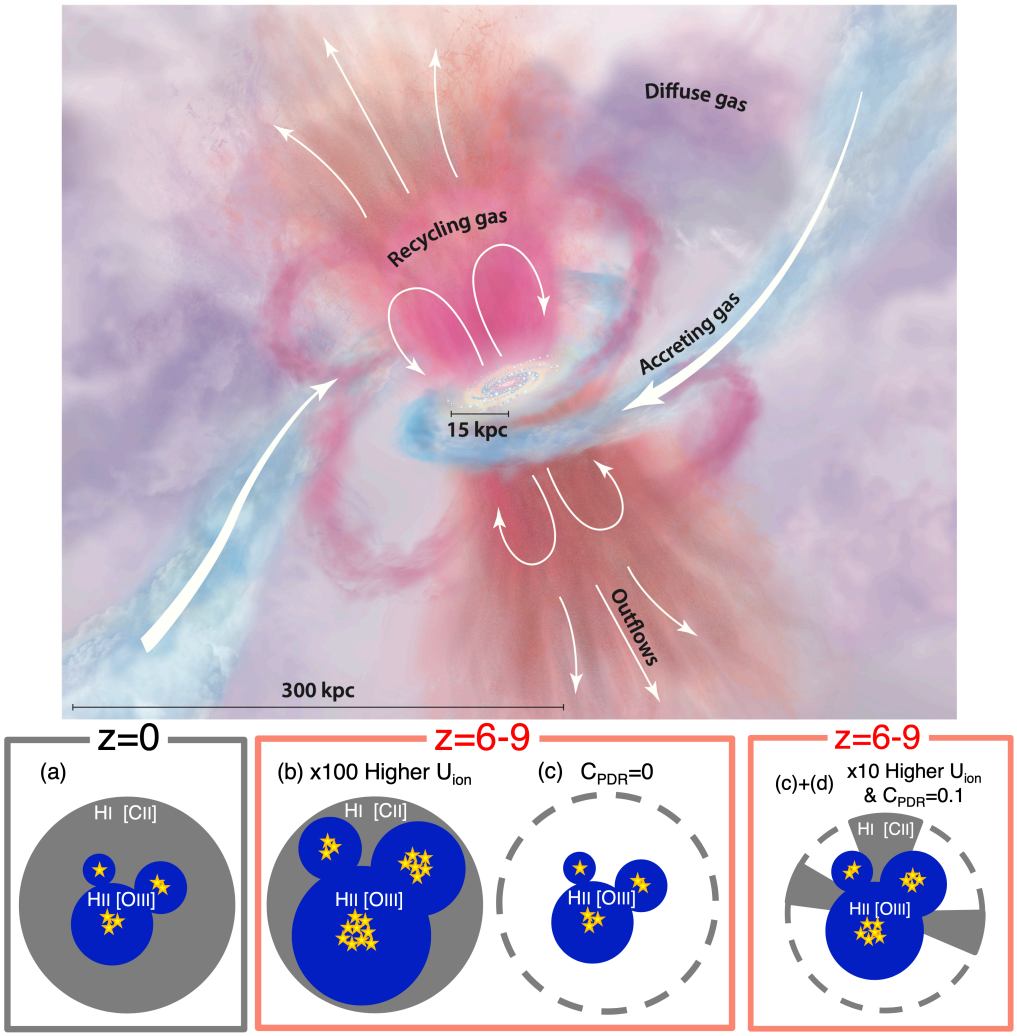


**Figure 1.2:** *Top:* A representation of the baryon cycle showing the interaction between a galaxy and its environment via gas accretion (blue), outflows (orange), and recycling (pink). The outer diffuse halo gas (purple) is mixed over time by a combination of these processes. Image taken from Tumlinson et al. (2017). *Bottom:* Ionisation in the ISM of a galaxy showing the PDR region and location where [C II] and [O III] are emitted. The ionised H II regions emitting [O III] (and [N II]) are shown in blue, the PDRs emitting [C II] are shown in grey, and ionising sources are shown as yellow stars. The leftmost panel (a) shows the ionisation structure in typical $z \sim 0$ galaxies. Panel (b) shows the case of very high ionisation observed in $z \sim 6$–9 galaxies, caused either by a young stellar population or a compact size. Panel (c) shows the hypothetical case of a PDR covering fraction, $C_{PDR} = 0$. The rightmost panel shows an intermediate scenario between (b) and (c) with a low, non-zero $C_{PDR}$ and moderately high ionisation. Image from Harikane et al. (2020).

& Walter, 2013; Kewley et al., 2019; Cormier et al., 2019). Fig. 1.2 shows a representation of PDR regions around ionising stellar sources. The far-infrared (FIR) line [O III] arises from ionised regions, whereas [C II], with a lower ionisation potential, arises from the cooler PDR region (see Sec. 2.1). The sizes of the ionised and PDR regions depend on the strength of the radiation field (described by the ionisation parameter $U$ or $U_{\rm ion}$). High-$z$ galaxies have been observed to have harder radiation fields, and their PDR covering fraction ($C_{\rm PDR}$) is correspondingly expected to be more sparse than at $z \sim 0$. If an AGN is present, the inner ionised regions also include extremely high ionised species such as N V and C IV (Furtak et al., 2023b; Kumar et al., 2023).

Metals in the galaxy are produced in stars, supernova explosions (SNe), and AGB nucleosynthesis. Of note, O is produced in SNe following the death of massive stars, and C is produced both in SNe and low-mass AGB stars (Kobayashi et al., 2020; Jones et al., 2023). Initially in the history of a galaxy, both O and N are produced at the same rate and co-evolve linearly. However, once intermediate-mass stars enter their AGB phase, they produce excess N (called secondary nitrogen production; Vincenzo et al. 2016; Johnson et al. 2022), changing the ratio of N to O in the ISM. Beyond this point, N is produced mainly by intermediate-mass AGB stars (Kobayashi et al., 2020). All these elements are then distributed throughout the galaxy via galactic winds and SNe-driven outflows (Curti et al., 2020; Kolborg et al., 2022; Sharda et al., 2023). The metal content can vary through the lifetime of a galaxy, however, depending on the level of stellar activity, the availability and inflow of pristine gas from the IGM, and the strength of the stellar/AGN feedback and outflow that can remove metals from the galaxy (Kirby et al., 2011; Li et al., 2022).

The origin and distribution of dust is more complex. Dust may originate in SNe (Hoyle et al., 1970; Dunne et al., 2009; Gall et al., 2011; Hirashita et al., 2014; Matsuura et al., 2019) and AGB stars (Ferrarotti et al., 2006; Schneider et al., 2014), in Wolf-Rayet stars or protostars (Matsuura et al., 2009; Forgan et al., 2017; Ginolfi et al., 2018; Witstok et al., 2023a), or grow via accretion in the ISM (Draine, 2009; Asano et al., 2013; Burgarella et al., 2020) Further, depending on the size of the dust grains and the strength of the radiation field, dust can be destroyed in AGN and SNe (Slavin et al., 2015; Tazaki & Ichikawa, 2020; Priestley et al., 2022), making the prediction of dust geometry complicated. Observations and simulations of galaxies at $z > 4$ seem to show a patchy rather than uniform dust distribution (Ma et al., 2019; Inami et al., 2022; Hygate et al., 2023; Birkin et al., 2023).

## 1.3 Role of AGN

Ever since the discovery of AGN (Schmidt & M., 1963; Hoyle et al., 1963; Salpeter et al., 1964), evidence has piled up that most galaxies may have a supermassive black hole (SMBH) at the center (Lynden-Bell, 1969; Kormendy & Ho, 2013), which, whether *currently* dormant or active, plays a crucial role in the formation and evolution of its host galaxy (Sijacki et al., 2015; Adler, 2021).

Supermassive black hole seeds are thought to have formed either as the remnants of Pop III stars or through direct collapse (Bromm & Loeb, 2003b; Wise et al., 2019; Haemmerlé et al., 2020; Sassano et al., 2021; Chantavat et al., 2023). The former produce seeds with masses of $10^2$–$10^4\,M_\odot$, whereas the latter can have seed masses of up to $10^6\,M_\odot$. These seeds then grow via accretion and mergers (Zhang et al., 2021; Lin et al., 2023) to create the SMBH we see today.

Given the tight correlations observed between SMBH and host galaxy properties (Magorrian et al., 1998; Silk et al., 1998; Ferrarese & Merritt, 2000; Gebhardt et al., 2000; Marconi & Hunt, 2003; Kormendy & Ho, 2013; López et al., 2023), some studies suggest that galaxies may form around primordial black hole seeds (Kim et al., 2019; Adler, 2021; Liu & Bromm, 2022), which then co-evolve with the host galaxy (Hopkins et al., 2008; Mullaney et al., 2012; Kormendy & Ho, 2013; Carraro et al., 2020).

AGN arise when the central SMBH begins accreting mass from its surroundings into an accretion disk (e.g.: Akiyama et al. 2019, although alternate theories have been suggested; see Antonucci et al. 2012). Matter falling onto the SMBH acquires kinetic energy through gravitational infall, and heats up further due to friction in the disk (Shakura et al., 1973). Consequently, SMBHs produce radiation across the electromagnetic spectrum from UV to IR, with many emitting in X-ray (Li et al., 2021), and in some cases also gamma-ray and radio emission if there is a jet present (Liu et al., 2005; Chen et al., 2023). This feedback, along with AGN-driven wind, regulates gas-temperature and thereby star-formation in the host galaxy (Fabian, 2012; Lemaux et al., 2014; Fiore et al., 2017; Sánchez et al., 2018).

As galaxies evolve in this way, they undergo changes in stellar and ISM structure and composition that produce measurable variation in the galaxy spectrum (e.g.: the 4000 Å Balmer break that reveals the age of the stellar population; Poggianti et al. 1997; Kriek et al. 2011) and morphology (e.g.: the transition across the Hubble tuning fork; Hubble et al. 1926; Treu et al. 2023). The history of a galaxy and the evolution that it has undergone is thus encoded in observable properties such as spatial extent and structure, and strength of emission from various species in its spectrum. Hence, studying these properties can provide insight into the evolution of galaxies. But how much of this information do we correctly extract from observations

that are limited by the capabilities, signal-to-noise ratio (SNR), and spatial and spectral resolution of the instrument used? For instance, some ultra-high redshift measurements based on photometry (Zavala et al., 2023), and even spectroscopy (Kaasinen et al., 2023), may simply be a product of the ambiguity in low SNR data.

Moreover, observation in each wavelength regime has its own unique advantages and challenges, as different wavelengths of light trace different components of a galaxy and phases of the ISM. UV continuum emission traces young stars (Cullen et al., 2023), FIR continuum traces dust (Hygate et al., 2023; Fujimoto et al., 2023b), emission from high ionisation species such as C IV and [Ne IV] (and broad line emission) traces AGN (Maiolino et al., 2023b), Ly$\alpha$, H$\alpha$, and other H recombination lines trace the ionised gas around young stars and AGN (Bunker et al., 2023a; Larson et al., 2023), [C II], [O III], [N II], and other FIR emission lines trace diffuse, metal-enriched gas close to star-forming regions (Fujimoto et al., 2022a; Vaidya et al., 2023), while CO (Lu et al., 2018), neutral [C I] (Valentino et al., 2020; Rizzo et al., 2023), and neutral [O I] (Lee et al., 2021) trace cooler gas away from star-forming regions. Understanding galaxy evolution requires that we observe and interpret each of these components correctly - how they form and transform, how they interact with and influence each other, and how the situation changes with redshift, galaxy mass, type, age, and environment.

In the next few chapters, I will discuss some relevant observational methods I used in my work to study high-$z$ galaxies, the limitations of the same, and recent developments in the field.

# Chapter 2

# ISM of the First Galaxies

Understanding galaxy evolution begins with analysing the earliest galaxies in the Universe. What were the conditions within their ISMs, and how and how quickly was the gas enriched with dust and metals? Studying interstellar gas, dust, and metals requires FIR observations, for which Atacama Large Millimeter/Sub-millimeter Array (ALMA) has become the ideal instrument, thanks to its excellent sensitivity and spatial resolution. It enabled several key discoveries in the last two decades, such as the first detection of dust in the early Universe (Watson et al., 2015), detection of FIR metal lines (Nagao et al., 2012; Hashimoto et al., 2018), including spatially resolved maps (De Breuck et al., 2014; Decarli et al., 2019a; Wong et al., 2022), and several spectroscopic confirmations of high-$z$ candidates from UV studies (Schouws et al., 2022a; Bouwens et al., 2022). In this chapter, I will provide an overview of the study of the ISM of the earliest galaxies in the Universe using ALMA.

| Line | Wavelength (μm) | Frequency (GHz) | Ionisation energy (eV) | Critical density ($cm^{-3}$) |
|---|---|---|---|---|
| [C II] | 157.68 | 1900.5 | 11.26 | 2800 |
| [O III] | 88.36 | 3393.0 | 35.12 | 510 |
| [O III] | 51.81 | 5785.9 | 35.12 | 3600 |
| [N II] | 121.80 | 2459.4 | 14.53 | 310 |
| [N II] | 205.30 | 1461.3 | 14.53 | 480 |

**Table 2.1:** Properties of FIR cooling lines commonly observed with ALMA, including rest wavelength and frequency, ionisation energy, and critical density. Values from (Padilla et al., 2022).

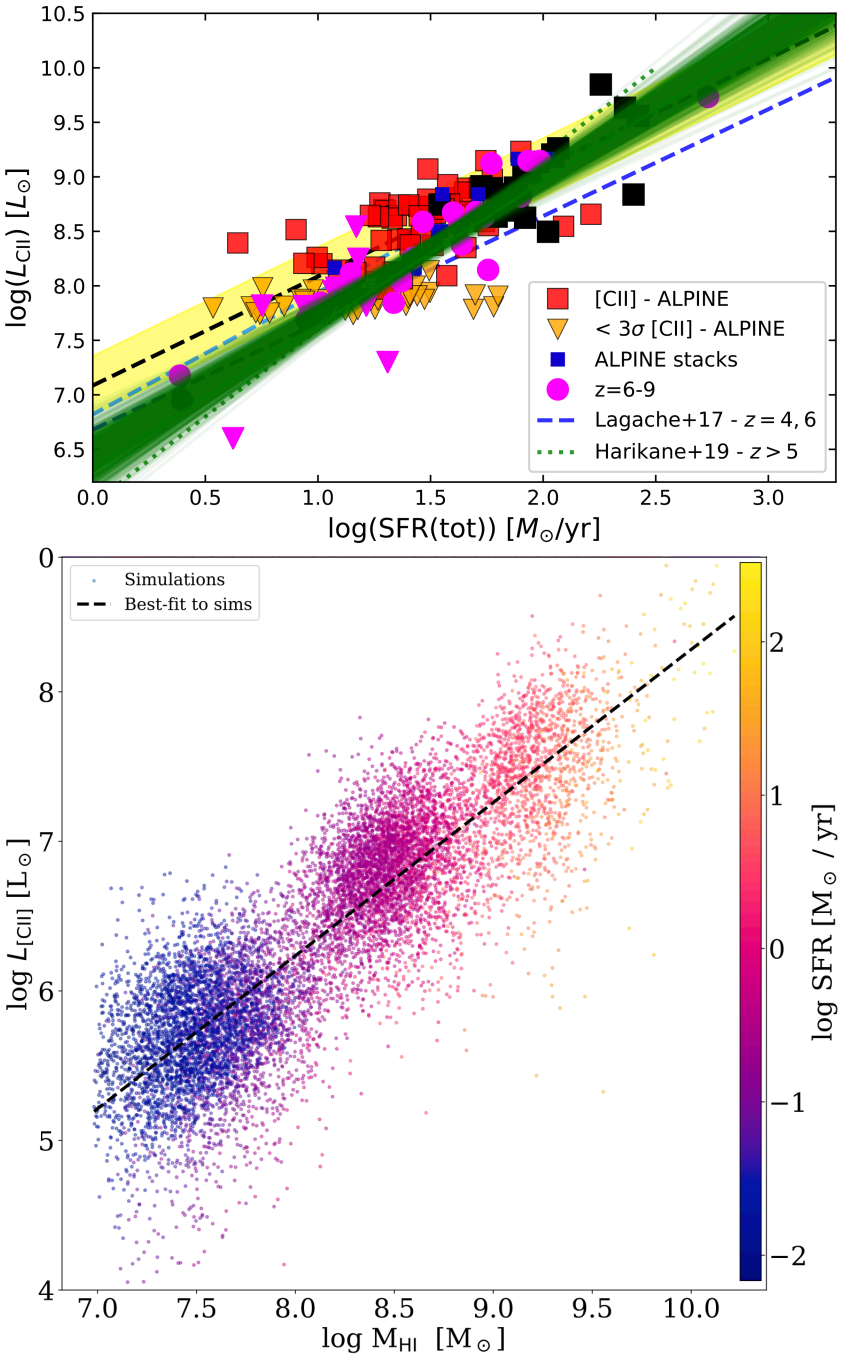


**Figure 2.1:** *Top:* Relationship between $L_{[CII]}$ and SFR from observations and simulations. Squares and circles represent [C II] detections, while triangles show upper limits. Black, red, and blue points are for $z \sim 4$–6 galaxies, and pink is for $z \sim 6$–9 galaxies. Blue dashed lines show $L_{[CII]}$-SFR relation from models. Linear fit to local galaxies is shown by the yellow band and black dashed line, fit to $z \sim 5$–9 observations is shown by the green dotted line, and fit to all $z > 4$ measurements, including upper limits, is shown by the green band. The slope of the relation is $1.28 \pm 0.10$. Image from Schaerer et al. (2020). *Bottom:* [C II]-H I relation. Relationship between $L_{[CII]}$ and H I gas mass from simulations at $z \sim 6$, colour-coded by SFR. The plot follows a linear relation with $\log(L_{[CII]}) = 1.02 \log(M_{HI}) - 1.95$. Image taken from Vizgan et al. (2022).

## 2.1 FIR cooling lines

Commonly observed lines in the FIR come from fine-structure transitions of singly ionised C ([C II]), doubly ionised O ([O III]), and singly ionised N ([N II]). The properties of these lines are summarised in Table 2.1.

[C II] 158μm is of utmost interest because it is the strongest cooling line in the FIR (Tielens et al., 1985; Wolfire et al., 1995), and hence easily visible from Earth (Stacey et al., 1991; Malhotra et al., 1997; Brauher et al., 2008). Since its ionisation energy (11.2 eV) is lower than that of H, [C II] can coexist both with ionised H II and atomic H I, and also to some extent with molecular $H_2$. It can thus be used to trace the ionised, neutral, and molecular gas in a galaxy (Zanella et al., 2018; Sutter et al., 2019; Cormier et al., 2019), which sometimes makes it difficult to interpret its origin. Nevertheless, it has been widely used in calibrations as an SFR tracer (Boselli et al., 2002; De Looze et al., 2014; Herrera-Camus et al., 2015) and also recently as a H I gas mass tracer (Heintz et al., 2021; Vizgan et al., 2022), as shown in Fig. 2.1. Both plots follow a tight linear relation across a range of redshifts and SFRs.

Although several non-detections were reported initially (e.g. Ouchi et al., 2013; Ota et al., 2014; Schaerer et al., 2015), [C II] has now been observed with ALMA up to $z \sim 8.5$ (Le Fèvre et al., 2020; Willott et al., 2015; Hygate et al., 2023; Heintz et al., 2023b), including extremely detailed resolved maps (Spilker et al., 2022; Posses et al., 2023), rotating disks (Carniani et al., 2013; De Breuck et al., 2014; Jones et al., 2021), and extended halos (Fujimoto et al., 2020).

The [O III] lines at 88μm and 52μm are also bright (potentially brighter than [C II]; Inoue et al. 2014), but [O III] 88 μm is favoured over [O III] 52 μm as it is more accessible with ALMA from the ground for high-$z$ observations (owing to atmospheric absorption in short-wavelength ALMA bands). With an ionisation potential of 35.1 eV, [O III] is a forbidden line that arises from hot, ionised gas surrounding stars. It has therefore been used as an SFR and ionised gas tracer (De Looze et al., 2014; Padilla et al., 2022), and has been detected up to $z \sim 7$ (Sugahara et al., 2021; Witstok et al., 2022), including resolved maps (Wong et al., 2022; Ren et al., 2023).

[N II], with an ionisation potential of 14.5 eV, is relatively more delicate than [O III], and can be found in the ionised gas surrounding stars, but at larger radii than [O III]. [N II] is also a doublet with emission at 122μm and 205μm. The latter has been detected with ALMA up to $z \sim 7$ (Béthermin et al., 2016; Pavesi et al., 2016; Vaidya et al., 2023), and my own work (Killi et al., 2023) presented in Part II reports the first detection of the former beyond $z \sim 7$.

ALMA can simultaneously measure the underlying continuum along with each line. FIR dust continuum measurements have been used to infer properties such as dust temperature (Sugahara et al., 2021; Bakx et al.,

2021; Akins et al., 2022; Sommovigo et al., 2022a; Tripodi et al., 2023; Fudamoto et al., 2023), dust-to-gas and dust-to-metal ratios (see Sec. 2.2.3), and dust mass budget Pozzi et al. (2021) and dust-obscured star formation (Zavala et al., 2021; Bowler et al., 2022; Inami et al., 2022) in the Universe.

In the next section, I will discuss *how* we infer ISM properties using all the above FIR observations.

## 2.2 Studying the ISM in the FIR

The ISM of a galaxy is described by several fundamental parameters: metallicity, hydrogen density $n_H$ (assumed to be the same as the electron density $n_e$), ionisation parameter, and gas temperature. These parameters are co-dependent, and set by stars, AGN, gas, and dust (Harikane et al., 2020). For collisionally excited, optically thin gas, they can be traced by FIR cooling lines, specifically, the relative ratios of these lines. Since energy differences between FIR electron states are much smaller compared to the typical gas temperature in the ionising regions of a galaxy, gas temperature does not have a significant effect on FIR lines (Yang et al., 2021). I will hence only focus on the other three parameters here.

### 2.2.1 Ionisation parameter

The ionisation parameter ($U$) is a measure of the strength and hardness of the ambient radiation in the ISM, and can reveal the extent and age of the starburst, and the level of activity of the AGN, if present. In my work I use the formulation by Harikane et al. (2020), where $U$ is defined as a function of the $n_H$, Strömgren radius, case B recombination rate, volume filling factor, and the speed of light. Typical values of $\log(U)$ for galaxies at $z > 6$ are found to be much higher ($\sim -1$ to -2; Harikane et al. 2020; Witstok et al. 2022; Fujimoto et al. 2022a) than the typical Milky Way value (-2.5 to -3.5; Kewley & Dopita 2002), suggesting the presence of harder ionisation fields at high-$z$ (as represented in the bottom panels of Fig. 1.2).

### 2.2.2 Density

The ratio of the [O III] 88 µm ($^3P_1$–$^3P_0$) line to the [O III] 52 µm ($^3P_2$–$^3P_1$) line is mostly independent of $U$ and $Z$ since both lines originate from the same ion, and can therefore be used to determine $n_H$ as described below.

Assuming a three level ion with no photo-dissociation, ions can be collisionally excited or de-excited, and can radiatively de-excite. Since the timescales involved in the atomic transitions here are short compared to those related to star-formation and galaxy evolution, a steady-state solu-

tion applies (Yang & Lidz, 2020). Thus, the number of ions entering a state exactly balances the number of ions leaving the state.

For state 2,

$$N_0 C_{02} + N_1 C_{12} = N_2(A_{21} + C_{21} + A_{20} + C_{20}), \tag{2.1}$$

where $N_i$ are the number of ions in the $i$th state, $A_{ij}$ is the Einstein A coefficient for the transition from state $i$ to state $j$.

$C_{ij}$ is the collisional term given by

$$C_{ij} = n_e q_{ij} = n_e \frac{\beta \gamma_{ij}}{g_i \sqrt{T}} \tag{2.2}$$

where $n_e$ is the electron density per cm$^3$, $g_i$ is the statistical weight of the $i$th state given by $2i + 1$, $\gamma_{ij}$ is the Maxwellian-averaged, i.e., *effective* collision strength for the $i$ to $j$ transition, and

$$\beta = \left(\frac{2\pi h^4}{km^3}\right)^{1/2} = 8.6 \times 10^{-6} \tag{2.3}$$

in CGS units.

Note that,

$$\gamma_{ij} = \gamma_{ji} \tag{2.4}$$

due to symmetry of collision strengths in thermodynamic equilibrium.

Similarly, for state 1,

$$N_0 C_{01} + N_2(A_{21} + C_{21}) = N_1(A_{10} + C_{10} + C_{12}) \tag{2.5}$$

Solving the equations 2.1 and 2.5, we have,

$$\frac{N_2}{N_1} = \frac{C_{02}(A_{10} + C_{10} + C_{12}) + C_{01}C_{12}}{C_{01}(A_{20} + C_{20} + A_{21} + C_{21}) + C_{02}(A_{21} + C_{21})} \tag{2.6}$$

Using Eq. 2.2,

$$\frac{N_2}{N_1} = \frac{q_{02}(\frac{A_{10}}{n_e} + q_{10} + q_{12}) + q_{01}q_{12}}{q_{01}(\frac{A_{20}}{n_e} + q_{20} + \frac{A_{21}}{n_e} + q_{21}) + q_{02}(\frac{A_{21}}{n_e} + q_{21})} \tag{2.7}$$

Now, in the specific case of the [O III] ion, $^3\mathrm{P}_0$ is state 0, $^3\mathrm{P}_1$ is state 1, and $^3\mathrm{P}_2$ is state 2. Therefore, luminosity ratio of [O III] 52 µm ($^3\mathrm{P}_2 - ^3\mathrm{P}_1$) to [O III] 88 µm ($^3\mathrm{P}_1 - ^3\mathrm{P}_0$) transitions can be written (ignoring the volume filling factor which is assumed to be the same for both [O III] lines; see Yang & Lidz 2020) as

$$\frac{L_{21}}{L_{10}} = \frac{E_{12}N_2A_{21}}{E_{01}N_1A_{10}} \tag{2.8}$$

where $E_{ij}$ is the energy difference between state i and state j. This energy is given by $h\nu$, where $\nu$ is the frequency of the photon emitted during

transition between state $i$ and $j$. Substituting this and the expression for $\frac{N_2}{N_1}$ from Eq. 2.7 into Eq. 2.8, we have

$$\frac{L_{21}}{L_{10}} = \frac{\nu_{12}A_{21}}{\nu_{01}A_{10}} \times \frac{q_{02}(\frac{A_{10}}{n_e} + q_{10} + q_{12}) + q_{01}q_{12}}{q_{01}(\frac{A_{20}}{n_e} + q_{20} + \frac{A_{21}}{n_e} + q_{21}) + q_{02}(\frac{A_{21}}{n_e} + q_{21})} \tag{2.9}$$

Thus the density can be determined using the observed $\frac{L_{21}}{L_{10}}$, i.e., [O III] 52/88μm luminosity ratio (see Fig. 9.3). Typical densities at high-$z$ are found to be of the order of a few hundred $\mathrm{cm}^{-3}$ in the ionised ISM, as seen from ALMA and UV measurements (e.g. Sugahara et al., 2021; Reddy et al., 2023; Fujimoto et al., 2022a).

### 2.2.3 Metallicity

The metallicity ($Z$; usually expressed as oxygen abundance $12 + \log(\mathrm{O/H})$) reveals the extent of processing of ISM by stars (Sec. 1.1.1), and can be measured either using UV auroral (e.g. Sanders et al., 2023) or FIR cooling lines (e.g. Heintz et al., 2023b). Whereas the UV/optical metallicity measurement only traces the unobscured regions of the galaxy, FIR metallicity also includes the dust-obscured regions (Nagao et al., 2011), hence providing a more comprehensive estimate. (Chartab et al., 2022) find that the difference is expected to be of the order of 0.3 dex despite excluding extremely dusty galaxies and AGN.

#### MZR and FMR

The correlation between galaxy mass (or luminosity in early studies) and metallicity has been observed for several decades (Larson et al., 1974; Garnett, 2002; Tremonti et al., 2004; Cowie & Barger, 2008; Wu et al., 2016), and it has been shown that this mass-metallicity relation (MZR) evolves with redshift (Savaglio et al., 2005; Maier et al., 2005; Ly et al., 2017; Sanders et al., 2021; Langeroodi et al., 2022). Sanders et al. (2021) parametrize the MZR as

$$\log(SFR) = a \log\left(\frac{M_*}{10^{10} M_\odot}\right) + b, \tag{2.10}$$

where $a$ and $b$ are fit empirically to galaxies at $z \sim 0$, 2.3, and 3.3. This relationship is shown in the top panel of Fig. 2.2.

Some studies have proposed that the observed mass–metallicity relation (MZR) is a consequence of a more general relation between mass, metallicity, and SFR - the fundamental metallicity relation (FMR; Mannucci et al. 2010; Lara-López et al. 2010; Henry et al. 2013; Curti et al. 2020). The FMR corrects for the observed evolution of the MZR with $z$, establishing a universal plane of M⋆-SFR-$Z$ on which all galaxies lie.

Curti et al. (2020) parametrise the FMR as

$$Z(M, SFR) = Z_0 - \frac{\gamma}{\beta} \log \left( 1 + \left( \frac{M}{M_0(SFR)} \right)^{-\beta} \right), \tag{2.11}$$

where $\log(M_0(SFR)) = m_0 + m_1 \log(SFR)$, and $Z_0$, $m_0$, $m_1$, $\gamma$, $\beta$ are fit parameters obtained by empirically fitting the observed data. This relationship is shown in the bottom panel of Fig. 2.2.

Other physical quantities have also been included into the FMR such as the stellar age (Puertas et al., 2022), gas mass (Lilly et al., 2013; Ma et al., 2016), and the ionisation parameter (Nakajima & Ouchi, 2014) to generate even more general relations.

That such relationships exist has become abundantly clear, but why they exist is still open to question. These deceptively simple relations require that we understand the complex interplay between various processes of the baryon cycle (Sec. 1.2). The addition of metals into the ISM happens via stellar winds, SNe, and AGB (e.g. Dwek, 1998; Maiolino & Mannucci, 2019); removal of metals occurs due to galactic wind- and feedback-induced outflow of metal-enriched gas (Garnett, 2002; Tremonti et al., 2004; Spitoni et al., 2010; Lin & Zu, 2023), and inflow of metal-poor gas from the IGM (Dekel et al., 2009; Mannucci et al., 2009; Kacprzak et al., 2016). To estimate the metal input requires that we know how many massive and low mass stars there have been in the history of the galaxy, i.e., the initial mass function (IMF). This in turn necessitates a correct estimate of the current stellar mass from the observed luminosity, which may be dust-obscured, and the star-formation history (SFH), which may be bursty. To measure the metal removal, we need to accurately measure the gas mass in the ISM, the strength of stellar/AGN feedback and whether it is enough to fully escape the gravitational potential, and the metallicity of inflowing and outflowing gas. Depending on redshift, galaxy mass, whether it is the central or satellite galaxy, and whether it has undergone a merger, the relative importance of these processes seems to vary (Dayal et al., 2013; Calabrò et al., 2022; Yao et al., 2022; Omori & Takeuchi, 2022; Wang et al., 2023). A comprehensive picture is yet to emerge on the origin and universal validity of the FMR.

### DTM and DTG

The dust-to-gas ratio (DTG) gives the ratio between the total interstellar dust mass and the total (including ionised, atomic, and molecular) gas mass in a galaxy. It is therefore a product both of the chemical maturity of the system, and its ability to retain the dust that it produces (by avoiding both dust grain destruction and dust loss via outflows). DTG is shown to evolve with metallicity (e.g. Wiseman et al., 2017; Kahre et al., 2018; Péroux & Howk, 2020; Lu et al., 2023) as shown in the top panel of Fig. 2.3,

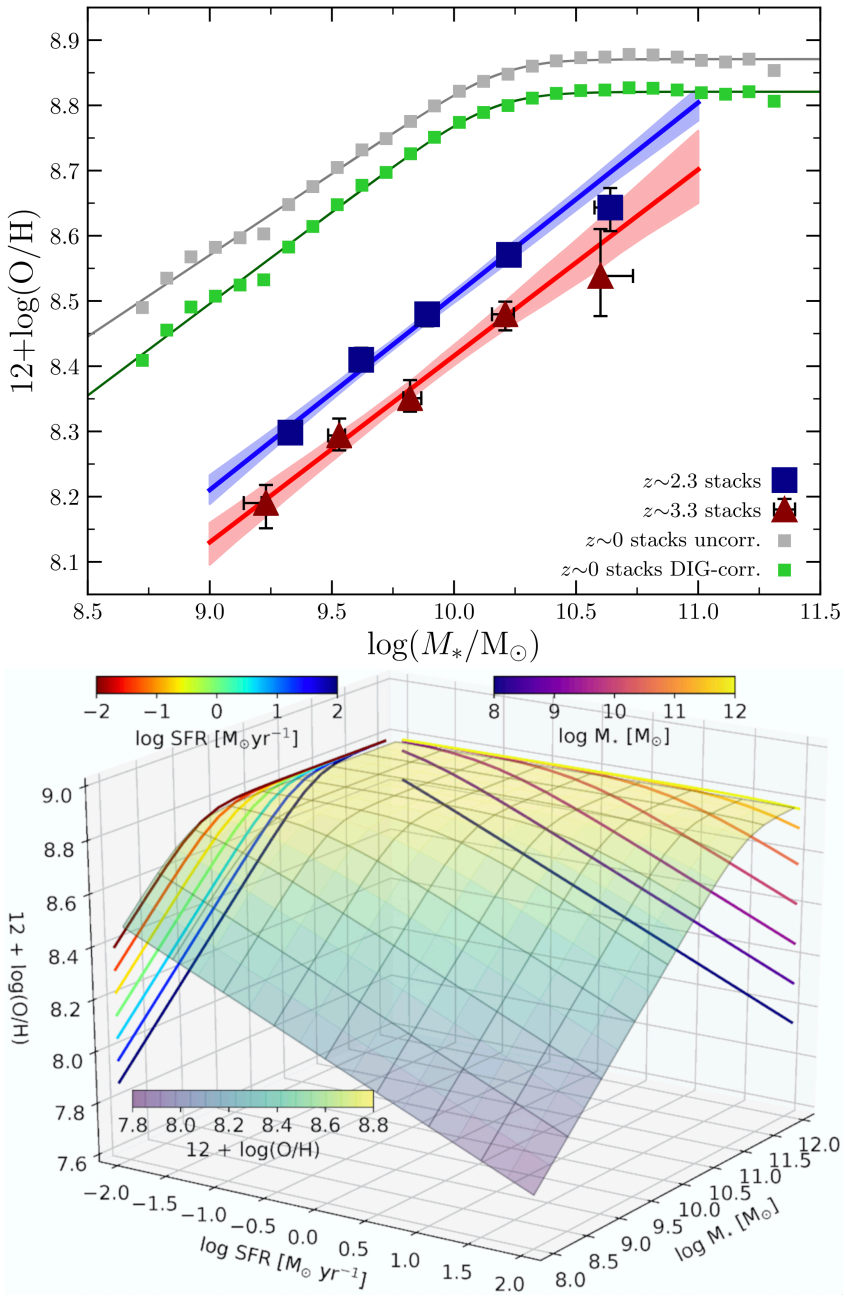


**Figure 2.2:** *Top:* MZR from stacked smaples of galaxies at $z \sim 0$ (grey and green), $z \sim 2.3$ (blue), and $z \sim 3.3$ (red), with solid lines showing the best-fit relations and shaded regions showing $1\sigma$ uncertainties on the fits. *Bottom:* A graphical representation of the FMR surface, colour-coded by its predicted metallicity values, along with contours of the projections of the FMR onto the M$_*$-$Z$ and SFR-$Z$ plane. Images taken from Sanders et al. (2021) and Curti et al. (2020).

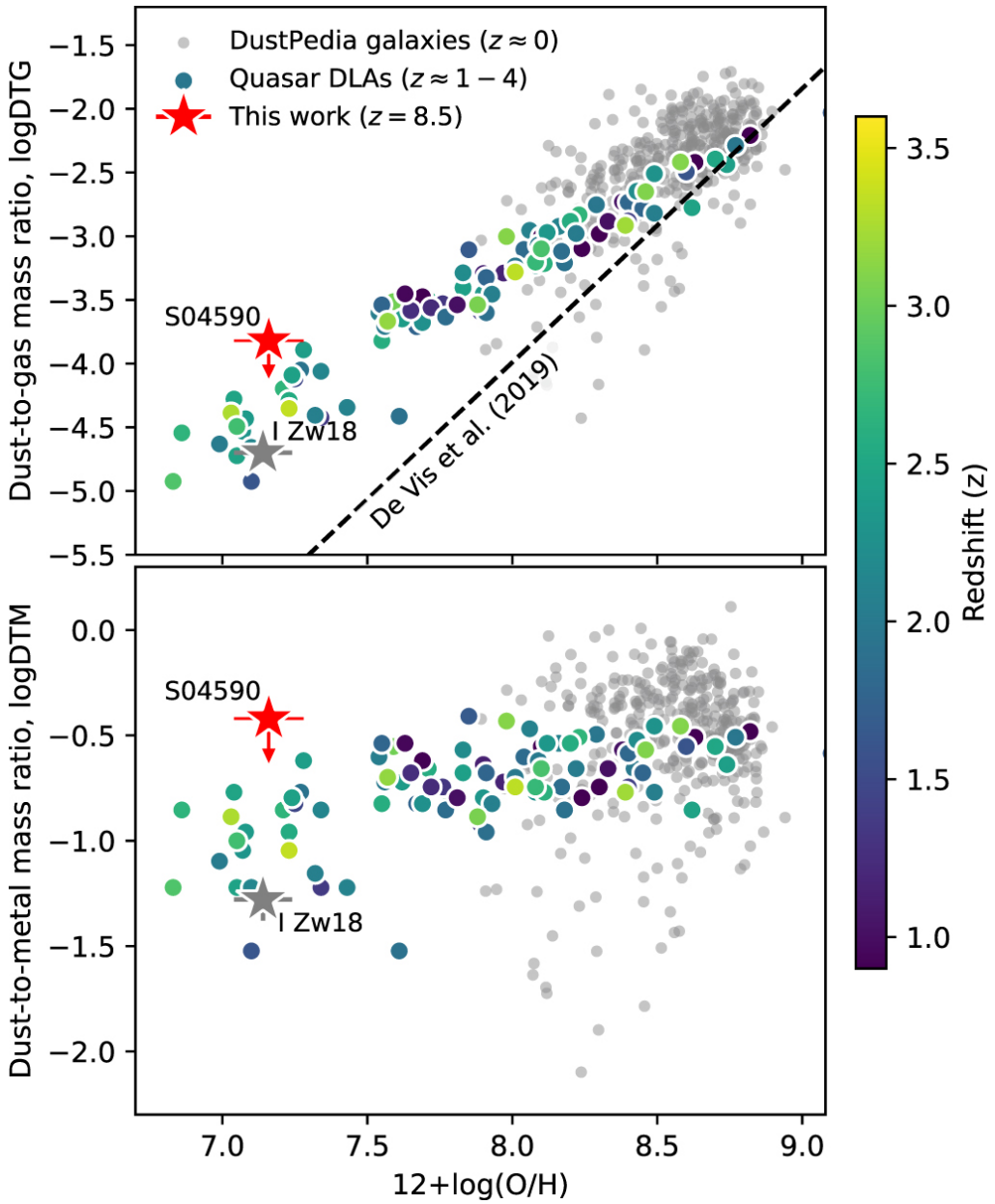


**Figure 2.3:** The DTG (top) and DTM (bottom) ratios plotted against gas-phase metallicity. Grey dots show galaxies at $z \sim 0$ along with their best-fit line, circles show quasar damped Ly$\alpha$ (DLA) systems, with colour representing redshift. The red and grey stars show metal-poor $z \sim 8.5$ and $z \sim 0$ galaxies respectively. Image taken from Heintz et al. (2023b).

with higher metallicity corresponding to a higher DTG, although this trend seems to break down at low metallicities (Galliano et al., 2005; Galametz et al., 2011; Rémy-Ruyer et al., 2014; De Vis et al., 2019).

The ratio between the dust and the metal content (DTM) is another important quantity that gives the amount of elements heavier than He that are present in solid form in dust grains vs in gaseous form in the ISM. This can tell us about the history of dust formation and destruction, and whether the conditions within the ISM (such as the strength of the radiation field) are favourable for the production and growth of solid dust grains, i.e., the dust formation efficiency of the galaxy. The dependence of the DTM on other physical properties such as metallicity, stellar mass, and SFR is somewhat unclear, with some claiming correlations, and others not (e.g. Zafar & Watson, 2013; Wiseman et al., 2017; De Vis et al., 2019; Li et al., 2019; Lu et al., 2023).

Estimating the DTM and DTG relies on accurate measurement of gas mass, which is difficult to determine because of the multi-phase nature of the ISM. Heintz et al. (2021) and Heintz et al. (2023b) present two different ways of estimating the gas mass, one directly using an empirical [C II] to H I gas mass conversion, and one via a parametrisation of dynamical mass from which stellar mass is subtracted to obtain gas mass. Once this quantity has been measured, DTG can be estimated by inferring dust mass from the ALMA dust continuum, and DTM can be obtained by inferring metal mass from the metallicity. Conversely, the metallicity and dust content have been used to estimate the gas mass fraction (e.g. Suzuki et al., 2021).

Studies have found a mild evolution of DTM and DTG with $z$ (Li et al., 2019; Péroux & Howk, 2020). Milky Way DTG is 0.006 and DTM is 0.45, but the values obtained at $z > 6$ by simulations (Behrens et al., 2018), and the few available observations (Heintz et al. 2023b and my own work presented in Part II), seem to be lower. This may be due redshift evolution of gas fraction (Tacconi et al., 2013; Scoville et al., 2017), metal content and composition (Yabe et al., 2015; Dors et al., 2018; Péroux & Howk, 2020; Isobe et al., 2023), or dust production mechanisms (Vijayan et al., 2019; Triani et al., 2020).

# Chapter 3

# Cosmic Morning Galaxies

While studying an individual galaxy can tell us about the specific conditions during its formation and evolution, understanding how galaxies as a whole evolved over the lifetime of the Universe requires statistical studies of large samples of galaxies. Can we find general trends at small- and large-scales in galaxy morphology and ISM as they transformed from primordial to modern? In the last decade there have been a few successful large surveys with ALMA that attempt to answer this question (e.g. González-López et al., 2017; Urquhart et al., 2022; Ferrara et al., 2022; Barrufet et al., 2023). Of note is the ALMA Large Programme to INvestigate $C^+$ at Early times (ALPINE) survey (Le Fèvre et al., 2020; Béthermin et al., 2020; Faisst et al., 2020) with over 20 publications, which reveals the conditions and properties of star-forming galaxies during Cosmic Morning.

## 3.1 The ALPINE survey

### 3.1.1 Star-formation

ALPINE galaxies all lie on the star-forming main-sequence (Noeske et al., 2007; Steinhardt et al., 2014; Speagle et al., 2014; Popesso et al., 2022) as shown in Fig. 3.1, and therefore represent the majority of galaxies in the Cosmic Morning (Rodighiero et al., 2011, 2015). They are selected to have UV magnitudes $M_{1500A} < -20.2$, and span a fairly wide range of stellar masses ($10^7$–$10^{11}\,M_\odot$) and SFRs ($10^{-2}$–$10^{3.5}\,M_\odot yr^{-1}$). Khusanova et al. (2021) parametrized the main-sequence for ALPINE galaxies, finding that the slope varies between the population at $z \sim 4.5$ and that at $z \sim 5.5$. However, they do not observe an evolution (in the normalisation) of the main-sequence from $z \sim 4.5$ to $z \sim 5.5$, as seen in UV studies at similar redshifts (e.g. Speagle et al., 2014; Popesso et al., 2022).

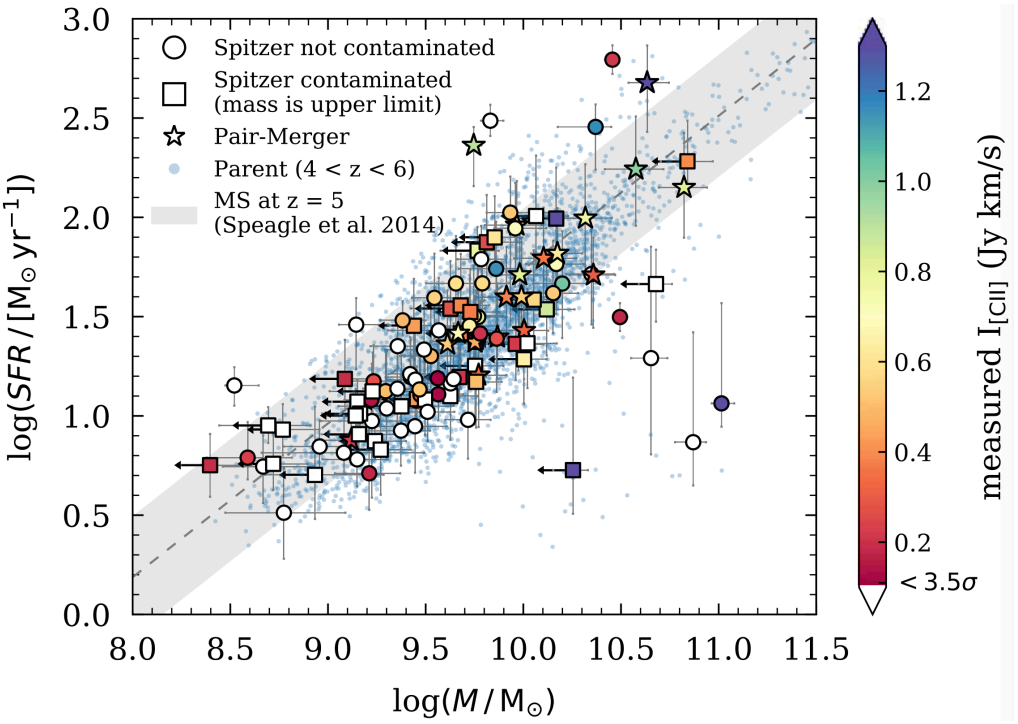


**Figure 3.1:** The main-sequence relation between stellar mass and SFR of ALPINE galaxies classified as Spitzer-contaminated (with only upper limit on stellar mass; squares), not contaminated (circles), and mergers (stars). Non-ALPINE galaxies at $4 < z < 6$ are shown as light blue points, and the Speagle et al. (2014) main-sequence at $z = 5$ is shown as a grey band. Points are coloured by [C II] flux, with non-detections shown in white. Image taken from Faisst et al. (2020).

### 3.1.2 Morphology and kinematics

A fraction of the ALPINE galaxies have complex morphology including merging and multi-component systems either in the [C II] or FIR continuum. Romano et al. (2021) estimate a merger fraction of 0.44 at $z \sim 4.5$ and 0.34 at $z \sim 5.5$, and rapid increase from the local Universe to higher redshifts, suggesting that major mergers play an important role in galaxy mass build up at early times. The detailed view of a galaxy at $z \sim 4.5$ presented by Jones et al. (2020a) provides a complementary picture, revealing an ongoing major merger and an upcoming minor merger that will likely appear as a single massive galaxy by $z \sim 2.5$. Further, the galaxies in the ALPINE sample with sufficient SNR have been classified into rotating, dispersion-dominated, and merging systems by Jones et al. (2021), who find that the fraction of simple rotating disks is lower than observed at low $z$, and suggest filamentary accretion may also help in mass assembly.

### 3.1.3 Feedback and outflows

ALPINE galaxies were selected to have low AGN activity, except for two sources that show some signatures of AGN (Barchiesi et al., 2023). Indeed Shen et al. (2022) study a stacked subset of the ALPINE galaxies from X-ray to radio and find no evidence of AGN activity. Nevertheless, these galaxies seem to have very strong feedback from stellar activity. Fujimoto et al. (2020) find extended [C II] halos around a third of isolated ALPINE galaxies, with 2–4 times the UV radii, implying that metal-enriched outflows were common at these redshifts. Pizzati et al. (2023) use semi-analytical modelling to confirm that [C II] halos are caused by starburst-driven cooling outflows, and suggest that such momentum-driven outflows are a common occurrence in the Cosmic Morning. (Cassata et al., 2020) observe velocity offsets between the ALPINE [C II] measurements and Ly$\alpha$ emission, finding further evidence for outflows. Ginolfi et al. (2020a) use a stacking analysis to estimate that these outflows have velocities of $\sim 500\,\mathrm{km\,s^{-1}}$, and are consistent with being driven by star-formation. Ginolfi et al. (2020b) focus on a single merging system at $z \sim 4.57$, and also find evidence for extended [C II] emission. In both cases, the spatial extent of the outflows is up to $\sim 30\,\mathrm{kpc}$, suggesting that they connect to the CGM, meaning the baryon cycle is already in place and playing a very important role in the Cosmic Morning.

### 3.1.4 Dust evolution

The evolution of the fraction of dust-obscured star-formation with redshift tells us how early the Universe was enriched with dust. As the dust content in the Universe increases, we expect that a greater fraction of star-formation will be obscured. But how quickly does this enrichment

occur and at what redshift does the obscured fraction overcome the unobscured fraction? Khusanova et al. (2021) find that the dust obscured star-formation is $\sim$ 68% at $z \sim 4$, and falls to $\sim$ 61% by $z \sim 5$. In Fig. 3.2, I show their estimate of the cosmic star-formation rate density (SFRD) as a function of redshift. While at $z \gtrsim 5$, UV-derived SFRD estimates are consistent with IR-derived values, there is a divergence below $z \sim 5$, with UV falling significantly short of the IR. This is confirmed by Fudamoto et al. (2020), who analyse the IRX-$\beta$ relation at $z \sim 5$, and find an obscured fraction of $\sim$ 45%, consistent with the Khusanova et al. (2021) estimate within the uncertainties. Although Boquien et al. (2022) argue that ALPINE galaxies fit with a diverse range of attenuation curves, from steeper than the extinction of the Small Magellanic Cloud (SMC), to shallower than that of a starburst, they also reassert the conclusions of Fudamoto et al. (2020). Several serendipitously discovered FIR galaxies in the ALPINE observations, a substantial number of which do not have UV counterparts (Gruppioni et al. 2020; Romano et al. 2020; see also Pozzi et al. 2021), reinforce the idea that a large percentage of star-formation in the Cosmic Morning is obscured. This means that the Universe has already been enriched with significant amounts of dust by this time as shown in Fig. 3.2.

### 3.1.5 Gas processing

The $L_{[CII]}$-SFR relation and the $L_{[CII]}/L_{IR}$ ratio of ALPINE galaxies agrees well with that at $z \sim 0$ (after correcting for dust-obscuration) (Schaerer et al., 2020). Even including the [C II]-undetected (either due to low metallicity or low [C II] luminosity) ALPINE galaxies does not alter the $L_{[CII]}$-SFR relation significantly (Romano et al. 2022; see Fig. 2.1). This shows that the mechanism that produces these relations does not evolve over this time period, although the [C II] luminosity function does seem to evolve between $z \sim 0$ and $z \sim 5$ (Loiacono et al., 2021). Yan et al. (2020) produce a [C II] line luminosity function in the Cosmic Morning, and estimate the number of [C II]-emitting galaxies there are in this epoch. Since ALPINE galaxies are UV-selected, they derive lower limits on this population, but estimate via indirect measures that the true numbers are 20–50 times higher than in the local Universe. The reason may be higher star formation, or higher gas fractions towards high-$z$.

Indeed Vanderhoof et al. (2022) find, for a sub-sample of ALPINE galaxies, an ionisation parameter consistent with galaxies at $z \sim 2$–3, but lower than that at $z \sim 6$ (e.g. Hutchison et al., 2019; Harikane et al., 2020), suggesting rapid evolution in the ISM radiation field within few 100 Myrs. Dessauges-Zavadsky et al. (2020) also lend support to this idea. By studying the evolution of the molecular gas in ALPINE galaxies (and those from literature at lower redshifts) find that the molecular gas fraction remains

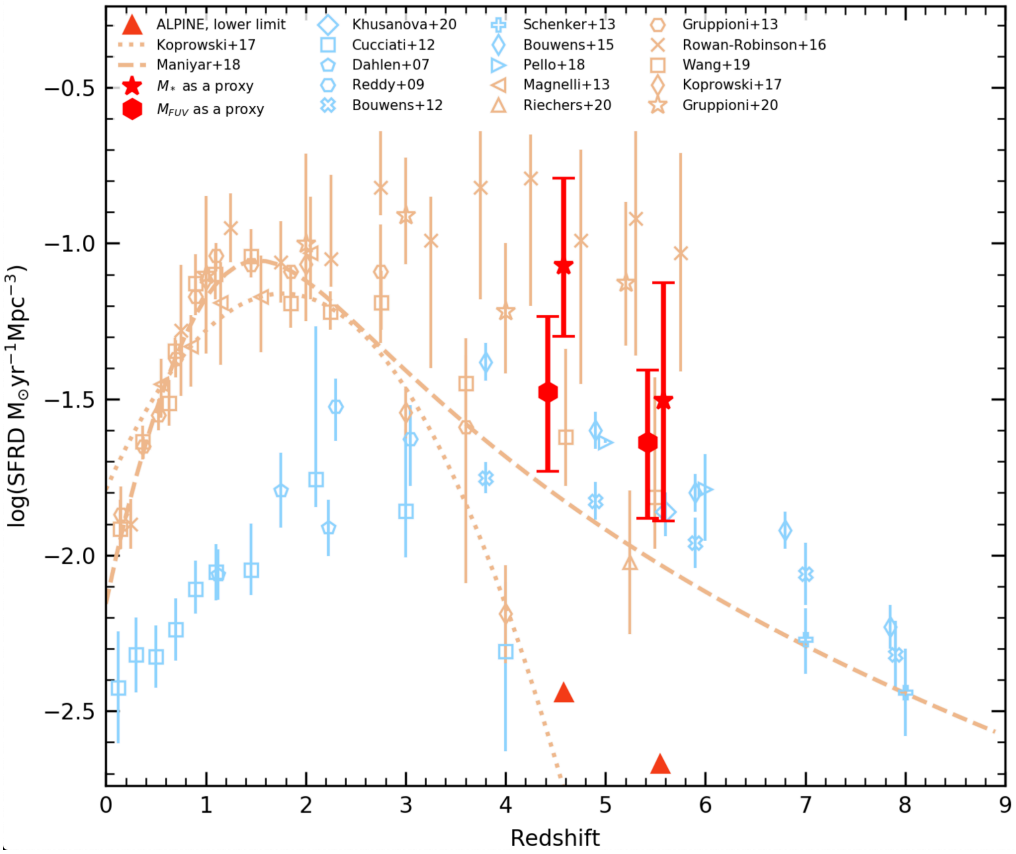


**Figure 3.2:** Redshift evolution of the star-formation rate density (SFRD) in the IR and UV. The measurements (stars and hexagons with errorbars) and lower limits (triangles) from Khusanova et al. (2021) are shown in red. The blue symbols represent UV SFRD measurements not corrected for dust obscuration. Brown symbols show IR derived SFRD values, along with fits to the IR SFRD evolution shown by brown lines. Image taken from Khusanova et al. (2021).

relatively flat during the Cosmic Morning, but drops rapidly to $z \sim 0$. This may reflect the high star-formation rate during cosmic noon that exhausts molecular gas reservoirs in galaxies. Dessauges-Zavadsky et al. (2020) also find that the ALPINE sample can be divided into low- and high-mass bins, which evolve differently; the low-mass galaxies consume gas gradually, and becoming Milky Way-like ($M_* \sim 10^{10.8}$–$10^{11.2} M_\odot$) by $z \sim 0$, whereas the high-mass ones consume little gas until $z \sim 2$, and then very quickly exhaust gas and transform into the high mass ($M_* \sim 10^{11.4}$–$10^{11.7} M_\odot$) galaxies we see at $z \sim 0$. Pozzi et al. (2021) suggest instead that ALPINE galaxies will likely evolve into the bulges of local spiral or elliptical galaxies, rather than disk galaxies such as the Milky Way.

Taken together, all these pieces of evidence show that the Cosmic Morning was a period of turbulence and rapid transformation where gas-rich galaxies formed about half of their stars in dust-obscured regions, underwent rapid stellar mass build-up via star-formation and mergers, and interacted heavily with the CGM and IGM via accretion and outflows. Thus, the ALPINE sample has revealed the conditions of main-sequence galaxies during Cosmic Morning. In Part III, I add to this knowledge with my recently submitted paper on the spatial offsets between stars and ISM in ALPINE galaxies.

## 3.2 Spatial offsets at high-$z$

Over the past decade, several observational works have highlighted the existence of stellar-ISM spatial offsets in galaxies at $z \sim 4$–$8.5$, as shown in Fig. 3.3. Some find the [C II] line emission offset from the UV (referring to emission in the restframe; similarly with "optical" and "NIR" in the following text) by a few kpc in Cosmic Morning galaxies (Carniani et al., 2018), and also at higher redshift (Maiolino et al., 2015; Pentericci et al., 2016; Matthee et al., 2019). Hodge et al. (2012) find that the CO(2-1) emission is offset from UV at $z \sim 4$, and Pentericci et al. (2016) find [C II] emission offset from NIR at $z \sim 6.6$. There have been reports of the dust continuum being offset from the UV by Bowler et al. (2022) and Schouws et al. (2022b) at $z \sim 7$. In some cases, the [O III] and optical emission coincide, but are together offset from the [C II] emission, as for the $z \sim 8.5$ galaxy from Fujimoto et al. (2022a). Sometimes, the [O III] and dust continuum are coincident, but the UV is offset from both as for the $z \sim 8.4$ galaxy studied by Laporte et al. (2017). Willott et al. (2015) present coincident [C II] and dust continuum, both offset from NIR emission at $z \sim 6$. Carniani et al. (2017) find a galaxy where [C II], [O III], UV are all offset, similar to Fujimoto et al. (2022a) who find [C II], dust continuum, and UV all offset from each other. Simulations also produce offsets between UV and dust emission (Arata et al., 2018; Sommovigo et al., 2020; Pallottini

et al., 2022), and [C II], [O III], and UV emission (Katz et al., 2017, 2019; Pallottini et al., 2019). Clearly, these offsets are not rare, and yet do not always occur between the same galaxy components. This suggests that there may be multiple mechanisms that produce offsets, and that these mechanisms must be common in high-$z$ galaxies.

Explanations that have been put forth include differential dust obscuration (Arata et al., 2018; Pallottini et al., 2022; Bowler et al., 2022), differential metal enrichment (Carniani et al., 2017), gas accretion and ionisation (Pentericci et al., 2016; Carniani et al., 2018), in-situ star-formation in the gas (Carniani et al., 2017), and feedback that disperses dust and gas (Sommovigo et al., 2020). Katz et al. (2017) predict that the young stars form in clumps of pristine gas fed by the IGM, which are offset from the location of dust and metal-enriched gas from which UV emission cannot escape, but [C II] and [O III] does. Further, they also predict that [O III] may be offset from [C II] as they arise from gas with different ionisation and temperature. This scenario is shown in Fig. 3.4. Katz et al. (2017) find also that the young stellar population is coincident with the $H_2$ location, but both are in turn offset from the old stellar population, which they argue is the configuration we would expect if the $H_2$ birth clouds are being destroyed by feedback from SNe from the young stars.

If this is indeed true, then why do we only observe certain kinds of offsets in a select few galaxies? As outflows, dust obscuration, and and gas accretion are common phenomena, offsets should be far more ubiquitous. Katz et al. (2019) offer a possible solution. They propose that spatial offsets can only be produced under specific conditions: a clumpy morphology and feedback that is just strong enough to destroy the neutral but not the ionised gas.

Even if these conditions are met, however, the *observation* of spatial offsets further depends on the viewing angle and the point in time at which we observe the galaxy, as offsets are a transient phenomenon. The simulations by Pallottini et al. (2019) and observations by Carniani et al. (2017); Matthee et al. (2019); Bowler et al. (2022); Schouws et al. (2022b) support the idea that a clumpy morphology can produce offsets. Pallottini et al. (2019) also show that if the relative luminosity between two emission lines is different in different parts of a galaxy, a non-detection in one part of the galaxy can move the centroid of emission towards the more dominant part, which would then produce an offset between the two line emissions. Kohandel et al. (2019) also show that the detection (or non-detection) of [C II] emission depends on viewing angle.

While such complex explanations mean that it will be difficult to explain when and why a *given* galaxy may display an offset, studying the number and sizes of offsets in a *large sample* of galaxies at a particular redshift epoch can tell us the physical conditions of the sample and time period as a whole. In this context, the ALPINE data can provide a more comprehensive

understanding of the number, nature, and physical origin of offsets, given the wealth of information we already possess about these galaxies (see Sec. 3.1.

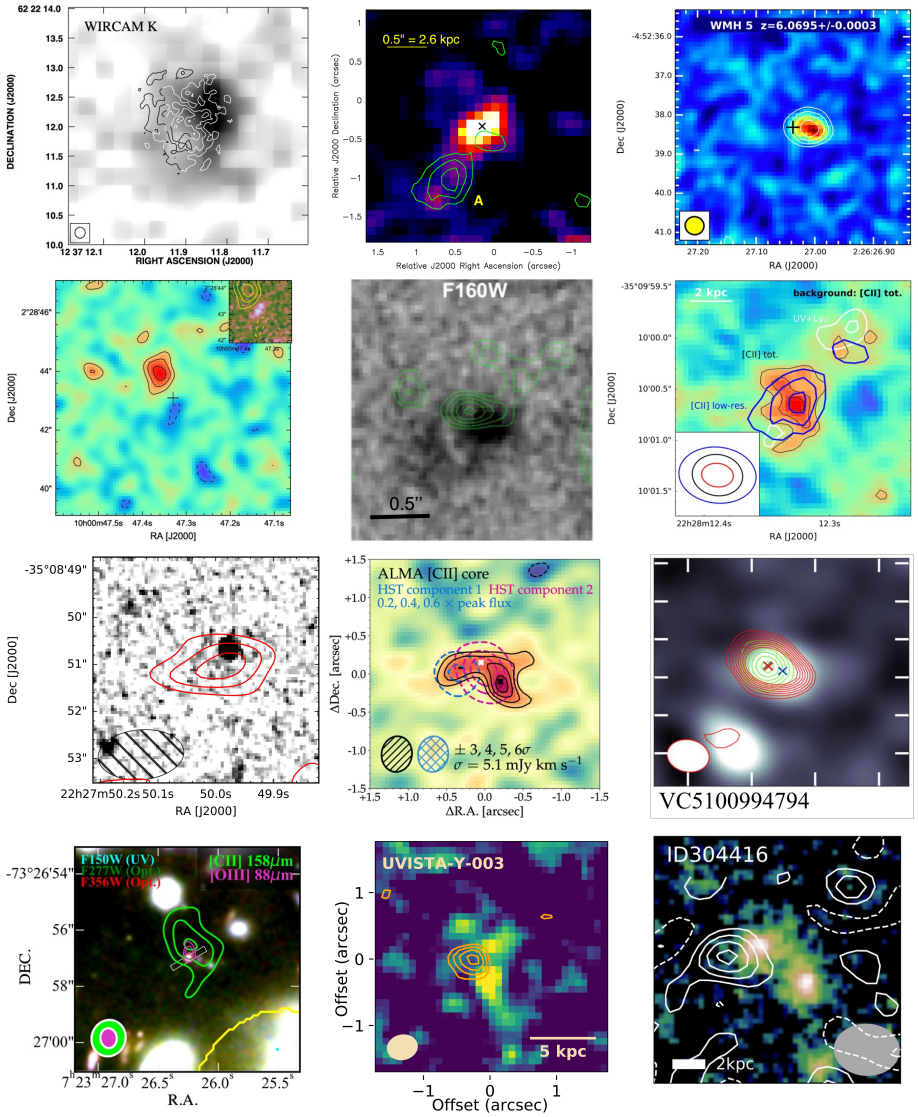


**Figure 3.3:** The images show (in order from left to right) offsets of the order of a few kpc between: *Row 1:* K-band optical (greyscale) and CO(2–1) (overlay) emission at $z \sim 4$ from Hodge et al. (2012), [C II] (green contours) and Y-band UV continuum (background) emission at $z \sim 7$ from Maiolino et al. (2015), [C II] (background) and 1.2 mm dust continuum (white contours) at $z \sim 6$ from Willott et al. (2015), *Row 2:* [C II] (black contours in the main image, yellow contours in the inset) and NIR (black crossbar in the main image, background image in the inset) at $z \sim 6$ from Pentericci et al. (2016), *HST* UV continuum (background) and ALMA dust continuum (green contours) at $z \sim 8$ from Laporte et al. (2017), [C II] (black, red, and purple contours) and Y-band UV continuum (white contours) at $z \sim 7$ from Carniani et al. (2017), *Row 3:* [C II] (red contours) and NIR continuum (background) at $z \sim 6$ from Carniani et al. (2018), [C II] (black contours) and *HST* UV continuum (blue and red contours) at $z \sim 6$ from Matthee et al. (2019), *HST* UV continuum (background image and blue cross) [C II] and ALMA dust continuum (red and green contours and crosses) at $z \sim 5$ from Fujimoto et al. (2020), *Row 4:* [C II] and [O III] (green and magenta contours) and *JWST* optical (background) emission at $z \sim 8$ from Fujimoto et al. (2022a), *HST* UV continuum (background) and dust continuum (orange contours) at $z \sim 8$ from Schouws et al. (2022b), *HST* UV continuum (background) and ALMA dust continuum (white contours) at $z \sim 7$ from Bowler et al. (2022).

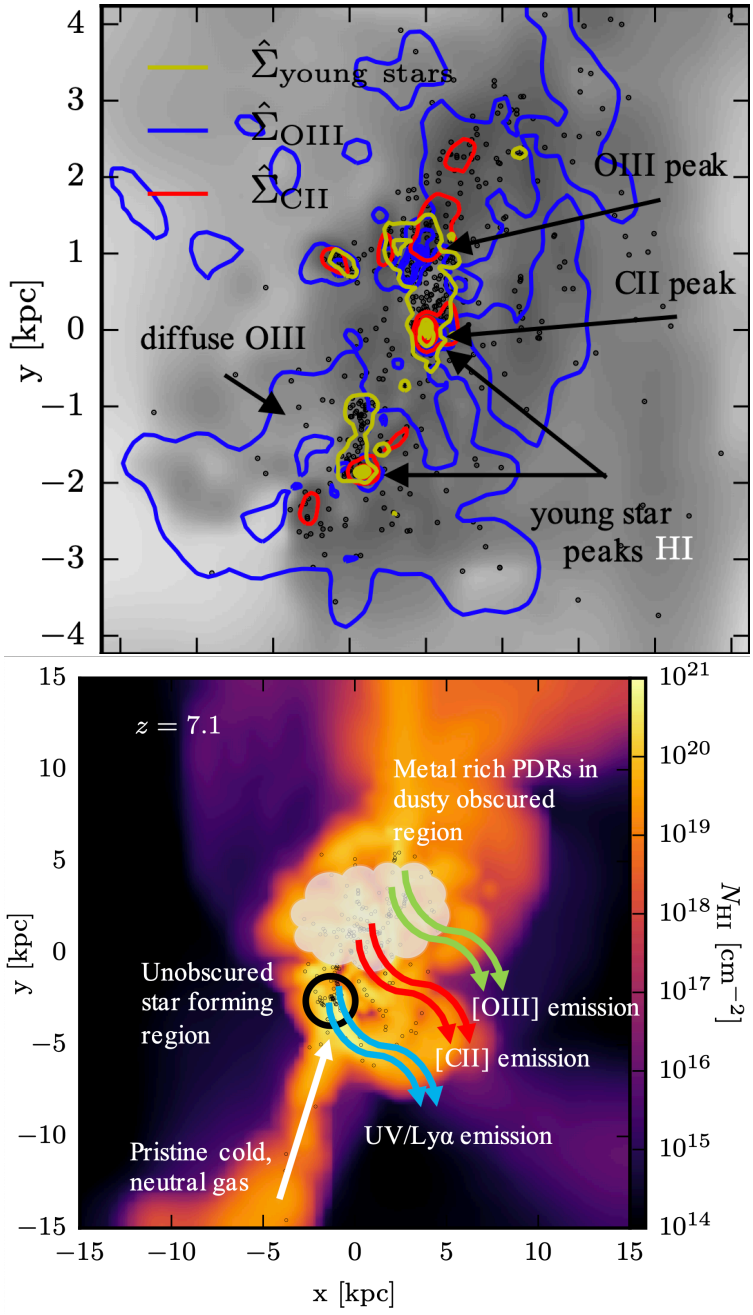


**Figure 3.4:** *Top:* Surface density plots of H I in the Katz et al. (2017) simulations at $z = 6$. The (normalised) column density contours of [O III], [C II], and young stars are shown in blue, red and yellow, respectively. The projected locations of young stars are shown as black points. The [O III] peak is spatially offset from the [C II] peak and young star peaks, while the [C II] peak is co-located with one of the young star peaks. *Bottom:* Surface density of neutral gas with [C II] (and [O III]) vs UV (and Ly$\alpha$) offset in the simulation at $z = 7.1$. Young stars are again shown as black points. Inflow of pristine cold, neutral, low-metallicity gas is shown with a white arrow. An unobscured star-forming region at the intersection of the inflowing filament and the galaxy is circled in black. A dust cloud is also depicted where UV emission is obscured, but the [C II] and [O III] emission can escape. The UV, [C II], and [O III] emission are shown with blue, red, and green arrows, respectively. Images from Katz et al. (2017).

# Chapter 4

# Cosmic Morning AGN and their hosts

While stars, dust, and gas form the bulk of a galaxy, the central black hole, although tiny in comparison by mass, plays a significant role in the life cycle of the galaxy (see Sec. 1.3). Study of galaxy evolution is therefore incomplete without an understanding of AGN evolution. But do our current models adequately explain the evolution of BH growth from Big Bang to the present day? AGN emission spans an even larger swathe of the electromagnetic spectrum than galaxy emission. Do observations and theories agree across this range? In this chapter, I will highlight our current understanding of the field, and new discoveries with *JWST* that are setting the stage for a paradigm shift.

## 4.1 AGN mass function

Many quasars at $z > 6$ have been identified with black hole masses of $M_{BH} \gtrsim 10^9\,M_\odot$ (e.g. Mortlock et al., 2011; Bañados et al., 2018; Wang et al., 2021; Farina et al., 2022). If all AGN at high-$z$ are indeed this massive, then it becomes necessary to invoke either direct collapse to form massive seeds of $\sim 10^5\,M_\odot$ or consistent and rapid super-Eddington accretion (Collin et al., 2002; Wang et al., 2014; Pezzulli et al., 2016) of Pop III seeds over the next billion years (see Sec. 1.3). However, given that AGN accretion is far from continuous and efficient over long timescales, except within the most massive DM halos (e.g. Neistein & Netzer, 2013; Storchi-Bergmann & Schnorr-Müller, 2019), and direct collapse BH are yet to be observationally confirmed, it may be that this mode of SMBH formation only occurs in the most extreme cases, while the majority of AGN at high-$z$ are less massive than those that have been observed so far (Inayoshi et al., 2020). Indeed, simulations predict an increase in the number of low mass black holes towards higher redshifts as shown by the evolution of the AGN mass function in Fig. 4.1. At $z \sim 0$, we see a flatter distribution with a sig-

nificant number of SMBH weighing billion solar masses or higher. But this function becomes steeper towards higher $z$. Even at $z \sim 5$, the simulations by Volonteri et al. (2016) predict almost no BH at billion solar masses, so it is difficult to explain a large number of $M_{BH} \gtrsim 10^9\,M_\odot$ SMBH at $z > 6$. With *JWST*, we are for the first time, able to bridge the divide between simulations and observations by identifying low–moderate mass ($\sim 10^5$–$8\,M_\odot$) AGN at $z > 4$ (e.g. Larson et al., 2023; Harikane et al., 2023; Maiolino et al., 2023a). Current estimates place the number of low mass AGN at 10–100× the number counts from UV luminosity functions (e.g. Barro et al., 2023; Furtak et al., 2023a). This may suggest that the very high-mass SMBH discovered previously were the exception, rather than the norm, and may therefore still be consistent with our current AGN models. On the other hand, these newly discovered AGN are too massive and numerous for their redshift range, and may hence still pose a challenge for BH growth models (Greene et al., 2023).

## 4.2 Contribution to reionisation

The discovery of the numerous low mass AGN may also change our view on the contribution of AGN to the reionisation of Universe (Madau & Haardt, 2015; Giallongo et al., 2015; Jeon et al., 2022). The current consensus is that galaxies took on the majority of this task, and AGN contribution was minimal at $z \gtrsim 6$. In Fig. 4.2 from Trebitsch et al. (2021) for the OBELISK simulation, star-formation is by far the major contributor to reionisation at high-$z$. AGN only start to become relevant below $z \sim 4$, well past the end of reionisation at $z \sim 6$. A substantial increase in the AGN number counts may increase estimates of their contribution. One caveat is that many of these low-mass AGN appear to be dust-obscured, which may limit the number of reionising photons that escape the system. Nonetheless, Maiolino et al. (2023a) estimated that the AGN and their host galaxies may together contribute >10% to reionisation.

## 4.3 Studying AGN and their hosts

If early *JWST* results are to be believed, it is essential that we update the techniques we employ to classify objects as AGN, to keep up with this new generation of powerful space- and ground-based telescopes. I detail below some common identification methods, their pitfalls, and revised methods based on *JWST* data.

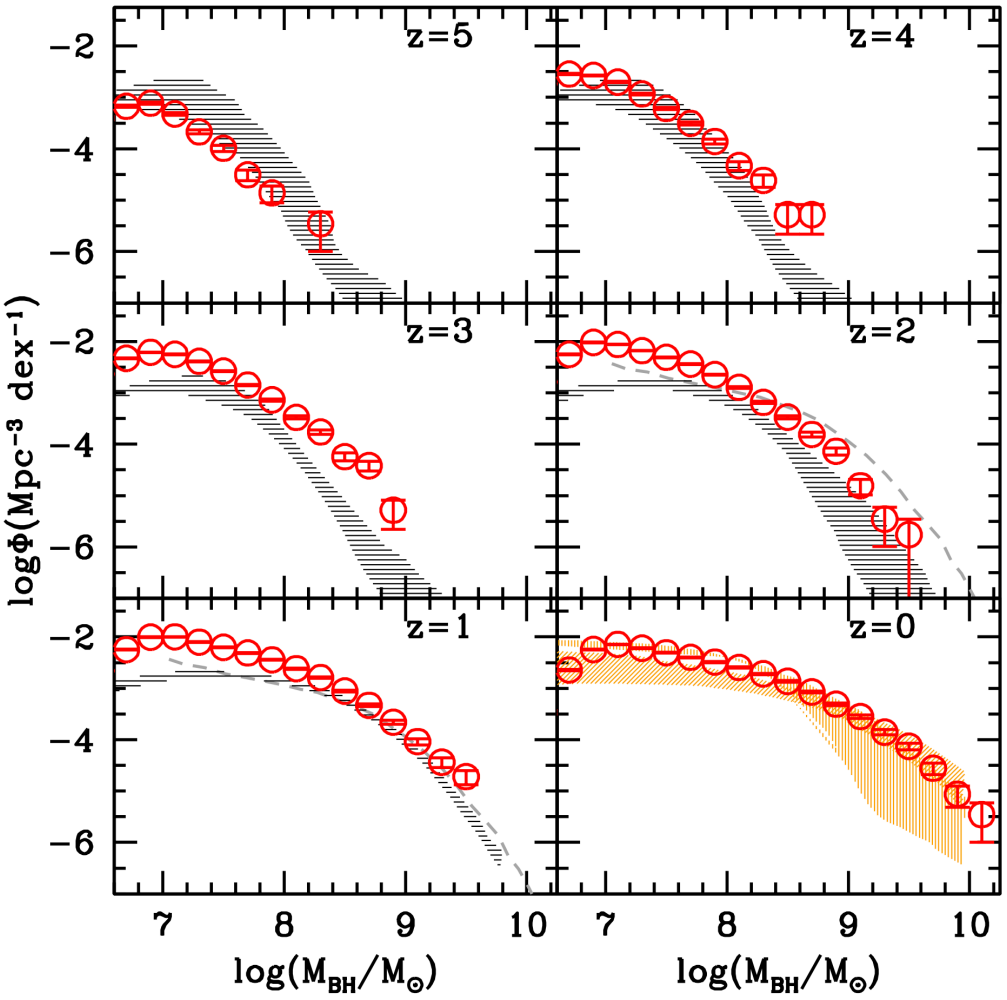


**Figure 4.1:** Observations (orange hatched regions and grey dashed curves) and simulations (black hatched regions and red circles) showing the evolution of the AGN BH mass function between $z$=0–5. We expect fewer black holes with $\log(M_{BH}) \gtrsim 8$ towards high-$z$. Image taken from Volonteri et al. (2016).

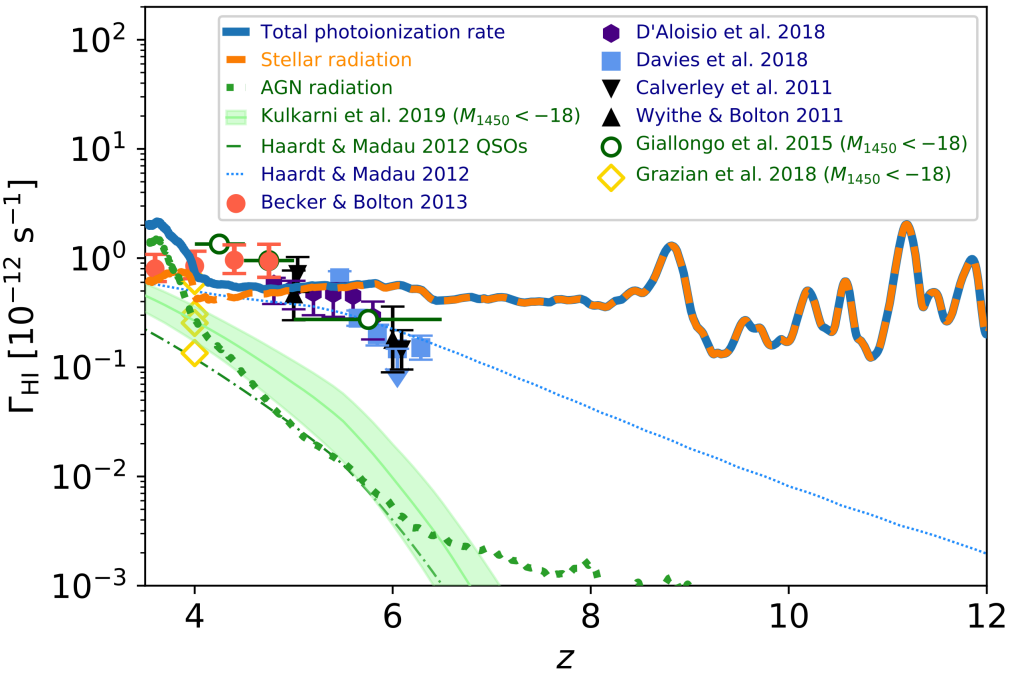


**Figure 4.2:** The contribution of stellar radiation from galaxies (orange) and AGN (green) to the total H I photoionization rate in ionized gas (blue). The simulations and observations from literature are shown in the respective colours as data points with errorbars. AGN contribution appears to be negligible during the reionisation era, and even up to $z \sim 4$. Image taken from Trebitsch et al. (2021).

### 4.3.1 Identifying AGN

Conventionally used methods to identify AGN via photometry include detecting the source in X-rays, and plotting the location of the source on ionisation diagrams such as the BPT diagram. Both methods have their limitations. X-ray studies of obscured AGN, which are possibly quite numerous, especially at high-$z$ (Vignali et al., 2014; Hatcher et al., 2021) requires very deep observations. Diagnostic diagrams, on the other hand, rely on observed local relationships between the abundance and ionisation of various species, which may be different at high-$z$. For instance, it is well-known that AGN with low-metallicity, a common occurrence at high-$z$, occupy the same region as local star-forming galaxies (e.g. Stasińska et al., 2006; Feltre et al., 2016; Polimera et al., 2022; Kocevski et al., 2023; Maiolino et al., 2023a). These diagrams also require the detection of four or more emission lines (although alternatives exist with less stringent requirements; e.g.: Cid Fernandes et al. 2010), which is challenging for low-luminosity obscured AGN. They also rely on the accurate modelling of observed flux to determine what fraction arises from the AGN and from star-formation in the host galaxy. Additionally, the standard assumption has been that AGN have a compact morphology (or at least a strong point-source component), but recent studies with *JWST* have shown that this is only true in case of AGN-dominated systems, and may well overlook moderate or low mass AGN where the host galaxy dominates the observed morphology (e.g. Harikane et al., 2023).

How do we identify an AGN that does not dominate the morphology, does not emit strongly in the X ray or radio part of the spectrum, and may occupy unusual regions of ionisation diagrams? Spectroscopy seems to be the only decisive method to pick out these obscured and low-to-moderate mass AGN that are overshadowed by their hosts.

### 4.3.2 UV/Optical spectra

The most prominent emission lines in the UV/optical part of the spectrum are the H recombination lines from the Lyman and Balmer series. Although Ly$\alpha$ emission (1215 Å) is strong, it undergoes resonant scattering, meaning that it can be absorbed and re-emitted (scattered out of the line of sight) several times on its way out of a galaxy (Neufeld et al., 1991; Kunth et al., 1998; Hayes et al., 2010). It can also be absorbed by the IGM especially at high-$z$ (Rauch et al., 1998; Bosman et al., 2018). The next most prominent recombination line is H$\alpha$ (6565 Å), which does not undergo resonant scattering, and can be used to trace the hot, ionised gas around young, massive stars. Whereas with the Hubble Space Telescope (*HST*), we were limited to observing Ly$\alpha$ beyond $z \sim 3$, *JWST* has already produced H$\alpha$ measurements up to $z \sim 7$ (Sun et al., 2023; Bosman et al., 2023).

The forbidden [O III] lines, including the doublet at 4959 and 5007 Å, and the [O III] 4363 Å line can be used to estimate gas temperature, and together with other lines such as [N II] and [O II], can also yield the metallicity, ionisation parameter, and density, although the results vary depending on the method used (McGaugh et al., 1991; Zaritsky et al., 1994; Kobulnicky et al., 1999; Pérez-Montero & Contini, 2009). *JWST* has allowed large surveys of metallicity measurements at high-$z$ (Curti et al., 2022; Sanders et al., 2023). Recently, Birkin et al. (2023) have even constructed resolved metallicity maps using [N II] and Hα at $z \sim 4$.

The FWHMs of emission lines broadened by galactic activity tend to be of the order of a few hundred $\mathrm{km\,s^{-1}}$, whereas line broadening in the narrow and broad line regions (NLR and BLR) around an SMBH results in much higher velocity widths, up to several thousands of $\mathrm{km\,s^{-1}}$. The division is not sharply defined, and some transient stellar processes can produce very high velocity winds e.g.:Baldassare et al. 2016, but FWHM$\gtrsim 500\,\mathrm{km\,s^{-1}}$ is generally accepted to be caused by the latter (Fabian, 2012). In addition, AGN BLR contributes to broadening of permitted lines (e.g.: Balmer), but not forbidden lines (e.g.: [O III] 5007 and [O III] 4959 Å) because the latter become weaker in high-density regions due to collisional de-excitation.

### 4.3.3 Dust

One major consideration for UV/optical studies is interstellar dust, as a large fraction of the emitted flux is lost to dust attenuation (or extinction in case of a point-source such as AGN). Attenuation can be estimated using Balmer decrement - by comparing the observed ratios between Balmer lines Hα, Hβ, Hγ, Hδ to the theoretical ratios from Case B recombination, we can estimate how much dust there is in the ISM (Momcheva et al., 2013). The Balmer decrement from the ratio of narrow lines gives the nebular attenuation, whereas that from broad lines gives the attenuation of the AGN emission due to dust around the BLR. Attenuation of the continuum emission, on the other hand, can be estimated by fitting attenuation curves (Calzetti et al., 2000), the choice of which can be challenging due to degeneracy between the effects of dust-reddening, the slope of the attenuation curve, and the intrinsic shape of the continuum itself. (Mao et al., 2014; Buat et al., 2019; Qin et al., 2022; Schulz et al., 2020; Hsu et al., 2023)

There may also be dust emission from hot dust grains in the AGN torus, which emits as a blackbody, following the Planck function, written in terms of wavelength $\lambda$ as:

$$B_\lambda \propto \frac{\frac{2hc^2}{\lambda^5}}{e^{\frac{hc}{\lambda k_\mathrm{B} T_\mathrm{B}}} - 1}, \tag{4.1}$$

where $h$ is the Planck constant, $c$ the speed of light, $k_\mathrm{B}$ the Boltzmann constant, and $T_\mathrm{B}$ the dust grain temperature. Typical dust temperatures

in the hottest regions of the torus tend to be $\sim$ 1000–1500 K (Rodríguez-Ardila & Mazzalay, 2006; Kim et al., 2015; Bosman et al., 2023), which can vary depending on the composition and size of the grains, but never exceed dust sublimation temperatures of $\sim$ 2200 K (Guhathakurta & Draine, 1989).

### 4.3.4 Unification models

Once an object has been identified as an AGN, it can then also be categorised under the wide array of sub-classifications, including Seyfert galaxies, quasars, radio galaxies, and blazars. Several models exist to explain this variety in AGN types.

The Unified AGN Model proposes that the cause is simply the viewing angle (Antonucci et al., 1993; Urry & Padovani, 1995; Netzer, 2015; den Brok et al., 2020). The top panel of Fig. 4.3 shows a representation of the model. Depending on which elements of the AGN - torus, BLR, NLR, jet if present - are visible to the observer, the spectrum may be dominated by X ray, UV, FIR, or radio emission, and may contain broad, narrow, or even no emission lines.

While convenient, this theory is not without its detractors (e.g. Villarroel et al., 2012; Ramos Padilla et al., 2022). Trump et al. (2011) propose that it is the accretion rate rather than the viewing angle that governs the observed spectrum.

Some works such as Narayanan et al. (2010), and more recently, Matthee et al. (2023) have suggested that depending on the age and the level of activity of the AGN at the present time, there may be an evolutionary sequence of highly host-dominated to highly AGN-dominated systems, i.e., from obscured AGN to luminous quasars. In this interpretation, the observed variation in the spectrum (the fraction of broad to total H$\alpha$ emission in case of Matthee et al. 2023) is attributed to differing stages in the evolution as shown in the bottom panels of Fig. 4.3. As the AGN evolves, it blows away obscuring material to reveal the luminous core within. Fujimoto et al. (2022b) recently found evidence for an AGN in such a transition phase at $z \sim 7.2$.

### 4.3.5 AGN properties

The mass of the central SMBH ($M_{BH}$) is the most defining property of an AGN, and sets limits on the bolometric luminosity ($L_{bol}$; Merloni et al. 2003; Shen et al. 2019; Liu et al. 2019) and in turn, the radius of the BLR ($R_{BLR}$).

As direct observation of the central AGN is limited by spatial resolution, we can instead indirectly estimate $M_{BH}$ by studying emission from the

[1] https://fermi.gsfc.nasa.gov/science/eteu/agn/

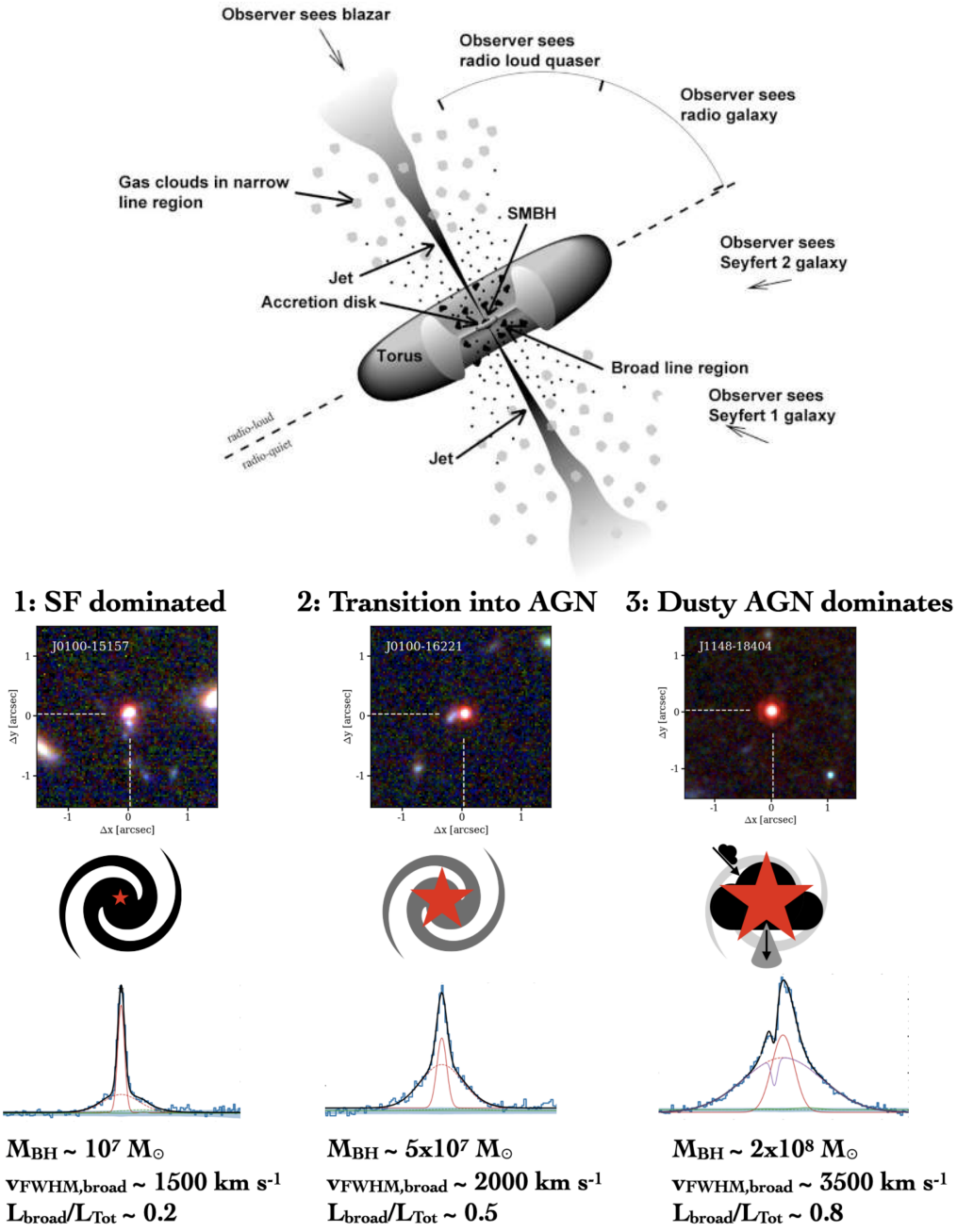


**Figure 4.3:** *Top:* A unified AGN model that proposes that the difference in AGN types seen by an observer is due to the viewing angle from Earth. A view where the BLR is obscured by the dust torus produces a Seyfert 2 galaxy with no broad lines, one where BLR is visible produces a Seyfert 1 galaxy with broad lines, a view directly through the jet (if present) produces no emission lines at all, and so on. Image credit: The Fermi Gamma-ray Telescope team[1]. *Bottom:* An evolutionary sequence of *JWST* AGN that shows how the observed spectrum can vary depending on the stage of the AGN-host evolution. A young AGN dominated by star-formation (SF) from its host produces a faint broad feature in Hα emission. As the AGN evolves, this feature becomes stronger and broader until it dominates the emission. Image taken from Matthee et al. (2023).

BLR. Reverberation mapping (Blandford et al., 1982; Peterson et al., 1993; Cackett et al., 2021) is a technique that utilises the time delay between flux variations in the light from the central source, and those in the re-radiated light from the BLR, to estimate AGN physical properties. This technique was used to establish an empirical correlation between $R_{BLR}$ and $L_{1500}$ continuum luminosity, which can be used to calculate $M_{BH}$ (Kaspi et al., 2000; Watson et al., 2011). Other studies have exploited the observed correlation between the radius of the Hβ emitting gas in the BLR and AGN luminosity (e.g. Marziani & Sulentic, 2012; Bentz et al., 2013). However, Hβ is intrinsically weaker than Hα, and more affected by dust due to its shorter rest wavelength, making it difficult to accurately determine the height of the broad emission component. $M_{BH}$ may then be overestimated due to contamination from the host galaxy flux. Hence, several recent works (e.g. Übler et al., 2023; Larson et al., 2023; Kocevski et al., 2023) have used the luminosity and FWHM of the broad component of Hα line, following Greene & Ho (2005), as this is guaranteed to be from the AGN, and bright enough to get a high SNR measurement even for host-dominated systems at high-$z$.

$M_{BH}$ can also trace some properties of the host galaxy, such as the stellar mass. In fact, it correlates linearly with stellar mass of the host galaxy (Reines & Volonteri, 2015; Bentz & Manne-Nicholas, 2018). While some studies find no evolution of this relationship with redshift (Sun et al., 2015; Suh et al., 2020), others find that it does evolve (Merloni et al., 2009; Ding et al., 2020). Recent *JWST* results support the latter viewpoint, especially at $z \sim 4$ (Pacucci et al., 2023). This indicates that BH growth occurs rapidly in the early Universe up to Cosmic Morning, at which point, galaxy growth picks up, overtaking BH growth, and reaching its peak by cosmic noon.

# Chapter 5

# Thesis Outline

The main objective of this thesis is to understand the process and timeline of evolution of the Universe by studying the ISM of high-z galaxies and AGN. In the previous chapters, the relevant theory and state-of-the art were presented. The remainder of the thesis will describe my work and future perspectives, including articles that have, or are set to, appear in peer-reviewed journals.

In Part II, I estimate the metallicity of a galaxy at $z \sim 7.1$, from which I derive the stage of evolution of the system, and in turn, the timeline of the formation of the very first galaxies in the Universe.

In Part III, I characterise the spatial distribution of stars and ISM of galaxies at $z \sim 4$–$6$, from which I deduce the conditions of the ISM and the internal processes occurring within star-forming galaxies at these redshifts.

In Part IV, I study the spectrum of one compact *JWST* source at $z \sim 4.5$, from which I infer its contents, and identify the nature of the object (whether it is a normal galaxy, an AGN, a starburst, or something else).

Finally, in Part 25, I provide perspectives on future research within these topics.

# Part II

# A1689-zD1

This part of the thesis contains the following article:

## "A solar metallicity galaxy at $z > 7$? Possible detection of the [N II] 122 μm and [O III] 52 μm lines"

Published in the Monthly Notices of the Royal Astronomical Society (MNRAS): Volume 521, Issue 2, pp.2526-2534, 2023.

Authors: Meghana Killi, Darach Watson, Seiji Fujimoto, Hollis Akins, Kirsten Knudsen, Johan Richard, Yuichi Harikane, Dimitra Rigopoulou, Francesca Rizzo, Michele Ginolfi, Gergö Popping, and Vasily Kokorev.

# Chapter 6

# Abstract

We present the first detection of the [N II] 122 µm and [O III] 52 µm lines for a reionisation-epoch galaxy. Based on these lines and previous [C II] 158 µm and [O III] 88 µm measurements, using two different radiative transfer models of the interstellar medium, we estimate an upper limit on electron density of $\lesssim 500\,\mathrm{cm}^{-3}$ and an approximate gas-phase metallicity of $Z/Z_\odot \sim 1.1 \pm 0.2$ for A1689-zD1, a gravitationally-lensed, dusty galaxy at $z = 7.133$. Other measurements or indicators of metallicity so far in galaxy interstellar media at $z \gtrsim 6$ are typically an order of magnitude lower than this. The unusually high metallicity makes A1689-zD1 inconsistent with the fundamental metallicity relation, although there is likely significant dust obscuration of the stellar mass, which may partly resolve the inconsistency. Given a solar metallicity, the dust-to-metals ratio is a factor of several lower than expected, hinting that galaxies beyond $z \sim 7$ may have lower dust formation efficiency. Finally, the inferred nitrogen enrichment compared to oxygen, on which the metallicity measurement depends, indicates that star-formation in the system is older than about 250 Myr, pushing the beginnings of this galaxy to $z > 10$.

# Chapter 7

# Introduction

The frontier of the study of galaxy evolution has now moved to the epoch of reionisation, $z \gtrsim 7$, where the physical conditions of the interstellar medium (ISM) are beginning to be investigated (e.g. Novak et al., 2019; Bouwens et al., 2022). Measuring these conditions is critical to our understanding of the evolution of galaxies and the growth of structure. The metal enrichment of the gas in galaxies, in particular, can tell us about the extent of processing of the ISM through stars, and therefore, the stage of evolution of the galaxy. However this fundamental ISM property is difficult to determine at high-$z$.

While at low redshifts, ISM properties are often determined using optical and ultraviolet (UV) emission lines (e.g. Kewley et al., 2019; Maiolino & Mannucci, 2019), at $z > 7$ those lines shift into the infrared (IR), where *JWST* is just beginning to produce the first results (e.g. Schaerer et al., 2022; Curti et al., 2022). However, heavily dust-obscured galaxies (e.g. Marrone et al., 2018; Fudamoto et al., 2021) cannot be studied with *JWST* because UV-optical observations cannot probe dust-obscured gas (Chartab et al., 2022). Hence, at high redshift, we require detections of bright far infrared (FIR) cooling lines and dust emission to estimate ISM properties (e.g. Nagao et al., 2011; Novak et al., 2019).

So far, FIR lines such as [C II] 158 µm and [O III] 88 µm (hereafter [C II] and [O88] respectively) have been detected in only a handful of $z > 7$ galaxies (e.g. Maiolino et al., 2015; Pentericci et al., 2016; Carniani et al., 2017; Hashimoto et al., 2019; Carniani et al., 2020; Sommovigo et al., 2021; Schouws et al., 2022a). Very few galaxies have been detected in both [O88] and [C II] at $z > 6$ (Carniani et al., 2017; Hashimoto et al., 2019; Tamura et al., 2019; Bakx et al., 2020; Harikane et al., 2020; Witstok et al., 2022), and only four of those are at $z > 7$.

Furthermore, while observations of the [O88] and [C II] lines and continuum emission allow the star-formation rate, dust mass and, to some extent, the temperature to be assessed with some reliability, determining the basic ISM parameters, i.e. the gas-phase metallicity, density, and ionisation parameter, requires other FIR lines. For instance, Pereira-Santaella et al.

(2017) and Harikane et al. (2020) describe models that use lines such as [O III] 52 µm and [N II] 122 µm (hereafter [O52] and [N II] respectively) in addition to [O88] and [C II].

However, this poses an observational challenge because while [O88] and [C II] are bright, [N II] is relatively faint and difficult to detect at $z > 6$. There have been [N II] detections in quasar host galaxies at $z = 6.003$ (Li et al., 2020), and $z = 7.54$ (Novak et al., 2019), but non-detections for all other systems attempted at $z \sim 6$–7 (Harikane et al., 2020; Sugahara et al., 2021). Although the [O52] line can be bright, it is also difficult to detect at this redshift as it lies in a wavelength region with low atmospheric transmission. Thus far, there have been no detections reported of [O52] at $z > 6$.

In this work, we report on the first measurement of the [O52] and [N II] lines for a non-quasar galaxy at $z > 6$. Together with previous [O88] and [C II] measurements (Akins et al. 2022; Wong et al. 2022; Knudsen et al. (in prep.)), we now have four FIR line detections for the gravitationally-lensed reionisation-epoch, dusty, normal galaxy A1689-zD1 at $z = 7.133$, making it the ideal candidate to study ISM conditions in re-ionisation era galaxies.

A1689-zD1 is lensed by the galaxy cluster Abell 1689 with a magnification factor of 9.3 (Watson et al., 2015). It was first discovered as a photometric candidate $z > 7$ galaxy (Bradley et al., 2008). The Ly$\alpha$ break was spectroscopically confirmed with deep VLT/X-shooter data, and it was shown to be a dusty galaxy with ALMA detections in bands 6 and 7 (Watson et al., 2015; Knudsen et al., 2017). This was the first detection of dust at $z > 7$, though more distant dust emitters have since been identified (e.g. Fudamoto et al., 2021; Ferrara et al., 2022; Schouws et al., 2022b; Laporte et al., 2017). A1689-zD1 has now been detected in strong [C II] and [O88] emission (Wong et al., 2022), the detailed 2D and 3D structure of which is studied in Akins et al. (2022) and Knudsen et al. (in prep.). The galaxy has also been detected in four continuum bands allowing an accurate measurement of its dust temperature and mass (Bakx et al., 2021). The rich multi-wavelength data set makes it one of the best-studied reionisation-epoch galaxies.

In this paper, we report the measured line fluxes, and calculate ratios among the four lines and their underlying continua to characterise the ISM of A1689-zD1. We deal here mainly with the galaxy-integrated properties. A resolved study of A1689-zD1 is presented in Knudsen et al. (in prep.).

We adopt a Flat ΛCDM cosmology with $H_0 = 67.74\,\mathrm{km\,s^{-1}\,Mpc^{-1}}$, $_M = 0.3075$, and $= 0.6925$ (Planck Collaboration et al., 2016).

# Chapter 8

# Observations and Methods

For the analysis presented in this work, we use the following the values for the stellar mass ($M_*$), dust mass ($M_\mathrm{d}$), and star-formation rate (SFR) for the galaxy: $M_* = 1.7^{+0.7}_{-0.5} \times 10^9 \mathrm{M}_\odot$ (Watson et al., 2015); total SFR $= 37 \pm 1\,\mathrm{M}_\odot\,\mathrm{yr}^{-1}$ (Akins et al., 2022); $M_\mathrm{d} = 1.7^{+1.3}_{-0.7} \times 10^7 \mathrm{M}_\odot$ (Bakx et al., 2021).

## 8.1 [N II] and [O52] observations

Observations were carried out at the Atacama Large Millimeter/submillimeter Array (ALMA) in Chile from November to December 2019 in cycle 7 (# 2019.1.01778.S, PI: D. Watson) under a precipitable water vapour (PWV) of 0.3–0.8 mm, using 42–45 antennae with projected baselines of 15–313 m. Based on a source redshift of $z = 7.1332 \pm 0.0005$, securely determined with [C II] and [O88] (Wong et al. 2022, Knudsen et al. (in prep.)), the available 7.5 GHz bandwidth with four spectral windows was centred at observed frequencies of 296.9 GHz (Band 7) and 703.8 GHz (Band 9) so that the [N II] and [O52] lines fall in one or two spectral windows. J1229+0203 and J1337−1257 were observed as the flux and bandpass calibrators. Phase calibration was performed by using observations of J1256−0547. The total on-source times were 200 minutes and 95 minutes for the [O52] and [N II] observations respectively.

We reduced the ALMA data with the Common Astronomy Software Applications package (CASA; McMullin et al. 2007) in the standard manner with the scripts provided by the ALMA observatory. We produced the continuum images and line cubes by running the CLEAN algorithm with the TCLEAN task. For continuum, we flagged the calibrated visibility in the expected frequency ranges of the lines. We executed the TCLEAN routines down to the $1\sigma$ level with a maximum iteration number of 10 000 in the automask mode with the sub-parameters determined by the recommendations of the ALMA automasking guide[1]. For cubes, we applied continuum subtraction to the calibrated visibility with the UVCONTSUB

[1] https://casaguides.nrao.edu/index.php/Automasking_Guide

**Table 8.1:** Data properties for the four lines and two continuum images used in this work. The [O52] and [N II] data were produced by natural weighting, while the [O88] and [C II] data use Briggs weighting as described in Knudsen et al. (in prep.). Beam size corresponds to the full width at half maximum (FWHM). The $1\sigma$ sensitivity is evaluated from the standard deviation of the pixel values.

| ALMA Band | Target line/continuum | Beam-size | Sensitivity |
|---|---|---|---|
| | | [″×″] | [mJy beam$^{-1}$] |
| 6 | [C II] | $0.24 \times 0.22$ | 0.02 |
| 7 | [N II] | $1.19 \times 0.98$ | 0.02 |
| 8 | [O88] | $0.33 \times 0.28$ | 0.12 |
| 9 | [O52] | $0.51 \times 0.42$ | 0.42 |
| 7 | continuum | $1.18 \times 0.97$ | 0.06 |
| 8 | continuum | $0.46 \times 0.40$ | 0.05 |

task by using the line-free frequency. We fit the continuum along channels at least ±500 km/s away from the expected line centre. We tried the subtraction with fitorders 0, 1, and 2. For [O52], the automasking and cleaning worked best for fitorder 0, and for [N II] the results were similar for all fitorders. We therefore chose to use fitorder of 0 for both [O52] and [N II] continuum subtraction. We adopted a spectral channel width of 20 km s$^{-1}$ and performed the CLEAN algorithm in each channel in the same manner as the continuum map. In both cases, we used natural weighting to maximise the sensitivity and applied the multi-scale deconvolver with scales of 0 (i.e. point source), 1, and 3 times the beam size. We list the synthesised beam size and the standard deviation of the pixel values in the final natural-weighted maps and cubes in Table 8.1.

# Chapter 9

# Results

## 9.1 Detection

In Figure 9.1, we show the velocity-integrated moment 0 maps[1] and spectra for the [N II] and [O52] lines (along with the [C II] and [O88] detections from previous studies). The [N II] and [O52] lines show significance levels of $5.0\sigma$ and $3.7\sigma$ at the peak pixel, respectively. The respective significance is $3.4\sigma$ and $3.8\sigma$ in the aperture optimised to each line (Fig. 9.1), and $3\sigma$ and $1.4\sigma$ in the common aperture (see Sec. 9.2). The morphology of the [O52] line is spatially extended (well beyond the beamsize), consistent with the spatial position and rough extent of the rest-frame UV continuum observed with the *Hubble Space Telescope* (*HST*) (Watson et al., 2015). Given the consistency with *HST*, we conclude that we achieve the first detection of the faint FIR lines of [O52] as well as [N II] at $z > 7$.

[1] produced using the SPECTRAL-CUBE package in PYTHON (Ginsburg et al., 2019)

**Table 9.1:** Galaxy-integrated line and continuum measurements for A1689-zD1 using an aperture as described in Sec. 9.2. The luminosity has been corrected for lensing, but the flux is uncorrected.

| Line | $\lambda_{\rm rest}$ | Flux | Luminosity ($L_\odot$) |
|---|---|---|---|
| [O III] | 52 µm | $2.3 \pm 1.6$ (Jy km s$^{-1}$) | $9.6 \pm 6.7 \times 10^8$ |
| [O III] | 88 µm | $5.75 \pm 0.38$ (Jy km s$^{-1}$) | $1.40 \pm 0.09 \times 10^9$ |
| [N II] | 122 µm | $0.09 \pm 0.03$ (Jy km s$^{-1}$) | $1.65 \pm 0.51 \times 10^7$ |
| [C II] | 158 µm | $3.56 \pm 0.07$ (Jy km s$^{-1}$) | $4.84 \pm 0.10 \times 10^8$ |
| continuum | 88 µm | $1.72 \pm 0.13$ (mJy) | |
| continuum | 122 µm | $0.82 \pm 0.03$ (mJy) | |

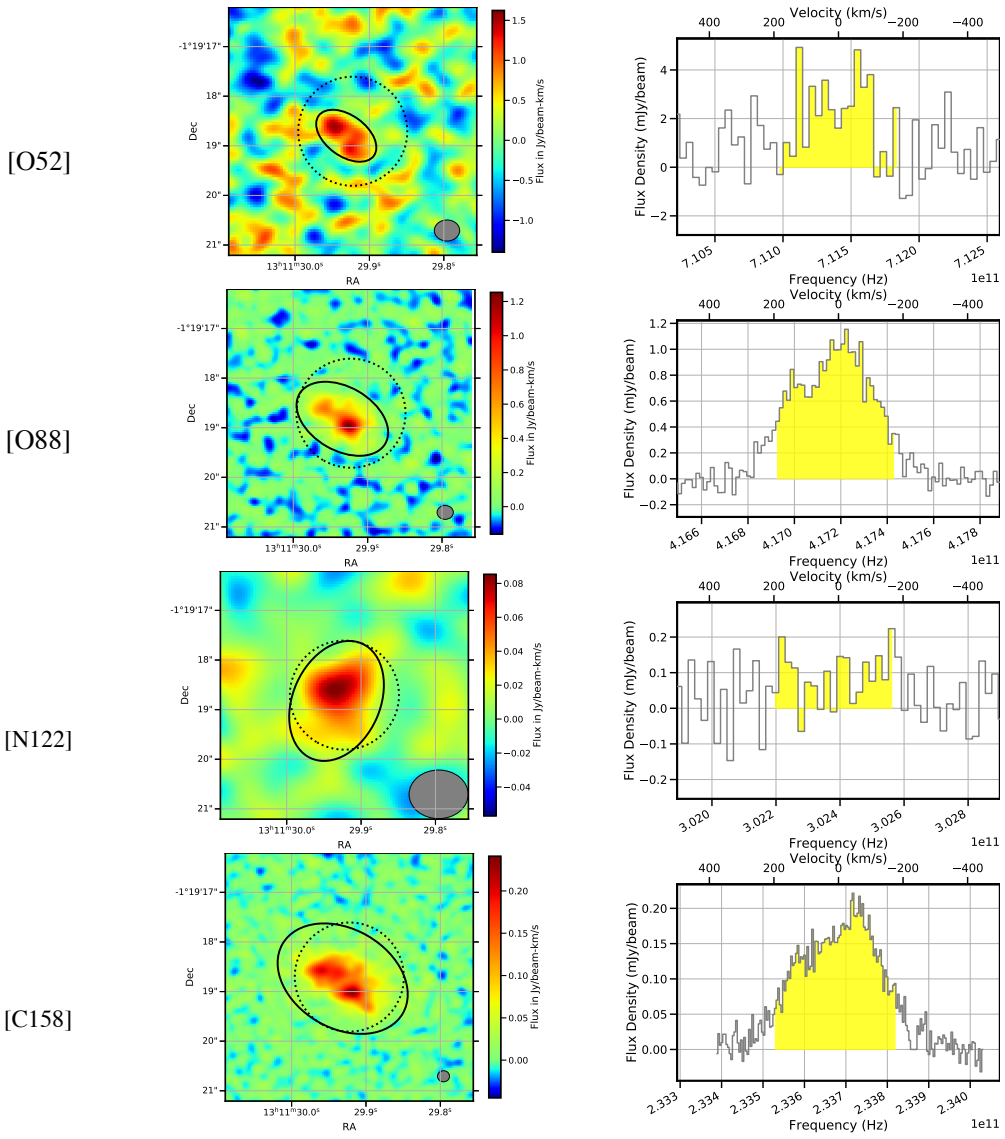


**Figure 9.1:** Velocity-integrated moment-0 map (left) and spectrum (right) for all four lines. We show two apertures for each line: the aperture used to extract the spectrum shown as an empty black ellipse, and the aperture used to extract the flux shown as an empty dotted ellipse. The former is customised to each line to extract the best possible spectrum. The latter, common aperture (see Sec. 9.2), has the same size and location for all lines to ensure that we use the same physical region to calculate line ratios and estimate metallicity. The beam size is shown by a filled grey ellipse. The highlighted spectral line bins are based on the [C II] line width of -180 to +200 km s$^{-1}$. No smoothing is applied.

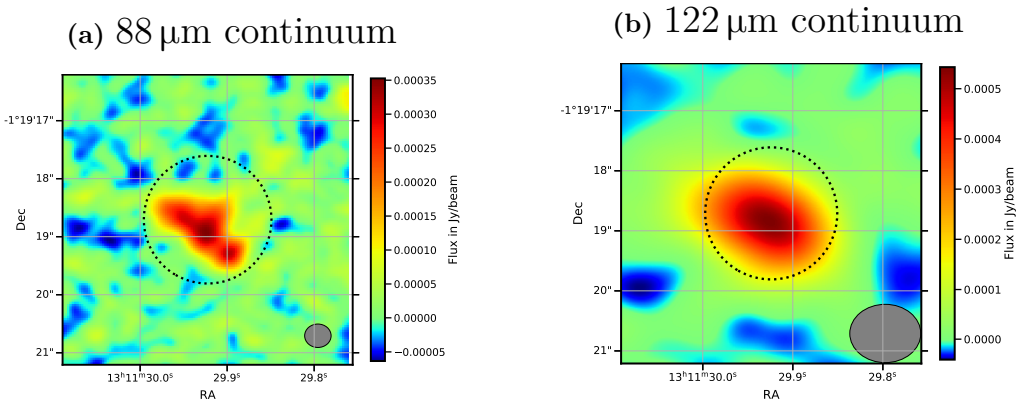


**Figure 9.2:** Continuum maps at 88 and 122 µm. As in Fig. 9.1, the empty dotted ellipse and the filled grey ellipse show the common aperture used to extract the flux and the beam size respectively.

## 9.2 Flux measurement

To perform a fair photometric comparison by analysing the same regions of the galaxy, we use a common aperture to extract the enclosed flux for the four lines and the underlying continua for [N II] and [O88]. The common aperture was selected to get the best estimate of the weakest lines, [O52] and [N II]. We use this common aperture for all our calculations. To find the best common aperture, we plotted the signal-to-noise ratio (SNR) as a function of increasing aperture radius for both [O52] and [N II]. For [O52], the highest SNR was at 0.″5 radius beyond which noise began to dominate. For [N II], the optimal aperture radius was around 1.″0. As the beamsize of the [N II] line was 1.″19 × 0.″98, we chose not to use the optimal [O52] aperture to avoid flux loss in an aperture with diameter smaller than the largest beamsize. Hence, we used a circular aperture with 1.″1 radius to include most of the [N II] and [O52] flux. We also adopt a common velocity integration range of $[-180 : +200]$ km s$^{-1}$ to estimate the line flux. This range is based on the $\sim 2\sigma$ velocity width for the [C II] line as can be seen from the last panel of Fig. 9.1.

We use a circular aperture of 1.″1 radius, centred at RA = 13:11:29.924 and Dec. = −01:19:18.710 (J2000). The aperture was chosen to include both the [O52] and [N II] lines, which is slightly larger than the detectable [O52] emission region (see Figs. 9.1 and 9.2). This aperture also encompasses the central [C II] and [O88] emission regions. We ensured that the aperture size is not smaller than the beam-size of our worst resolution image ([N II]). The fluxes and corresponding luminosities are shown in Table 9.1.

To test whether the difference in resolution affects our flux measurement, we tapered the higher resolution [O88] map to match the lower resolution [O52] and [N II] maps. The fluxes measured were consistent to the values reported in Table 9.1 within $\sim 1\sigma$ uncertainty. Additionally, we tested several elliptical and circular apertures that also encompassed all

four line emissions, and the results were consistent.

The detection significance of the [O52] and [N II] lines is $\sim 3.5\sigma$. To test the significance of the line detection further, we employed a moving spectral window and produced several moment-0 maps with midpoints across the velocity axis. Then we performed a systematic search for off-centre sources in each moment-0 map using a 1.″1 circular aperture. While for [N II], we found no other sources with $\geq 3.5\sigma$ significance, we did find a few of them for [O52]. However, these did not have extended spatial morphologies like the central source. Moreover, [O52] was only used to derive an upper limit (see Sec. 9.3.1), so if the detection significance is lower, our upper limit still holds.

## 9.3 Metallicity Constraint

In this section, we obtain a constraint for the metallicity, $Z$, of A1689-zD1 in a series of steps. We first derive the electron density, $n_e$, using the [O III] line ratio. We then combine this with the 88 to 122 µm dust continuum ratio to derive the ionisation parameter, $U$. Finally, using $U$ and the [O88] to [N II] line luminosity ratio, we constrain $Z$.

The flux ratios could in principle be affected by differential magnification, which in turn depends on the lensing model assumed. However, in this case, since we are calculating integrated galaxy properties in a common aperture and all the lines and continuua are mostly co-spatial, differential magnification is likely to be small, only of the order of a few per cent.

### 9.3.1 [O III] ratio

The ratio of the [O52] to [O88] luminosity is independent of both $Z$ and $U$ as both lines originate from the same ion, and of the temperature, because the energy difference between these two states is small compared to the typical gas temperature in the ionising regions of the galaxy. It is therefore a robust probe of $n_e$, up to $10^4$ or even $10^5\,\mathrm{cm}^{-3}$ (Palay et al., 2012; Pereira-Santaella et al., 2017; Zhang et al., 2018; Yang & Lidz, 2020).

Fig. 9.3 shows the theoretical relationship between the [O III] line ratio and $n_e$. The [O52] to [O88] ratio for A1689-zD1 in the common aperture is plotted as a horizontal purple line with $1\sigma$ uncertainty plotted as the corresponding shaded purple region. We derive a nominal value of $n_e \sim 55\,\mathrm{cm}^{-3}$ for the electron density. Including the $1\sigma$ uncertainty on the ratio, we obtain 1 and $2\sigma$ upper limit of $n_e \lesssim 260$ and $485\,\mathrm{cm}^{-3}$.

Our density derivation assumes that the gas is optically thin and in thermodynamic equilibrium at a temperature of 10 000 K. The upper limit is less than $10^3\,\mathrm{cm}^{-3}$ for any temperature between 5 000 and 20 000K. In the following analysis, we adopt the $1\sigma$ bound of $n_e \sim 260\,\mathrm{cm}^{-3}$ to propagate into our uncertainty calculation.

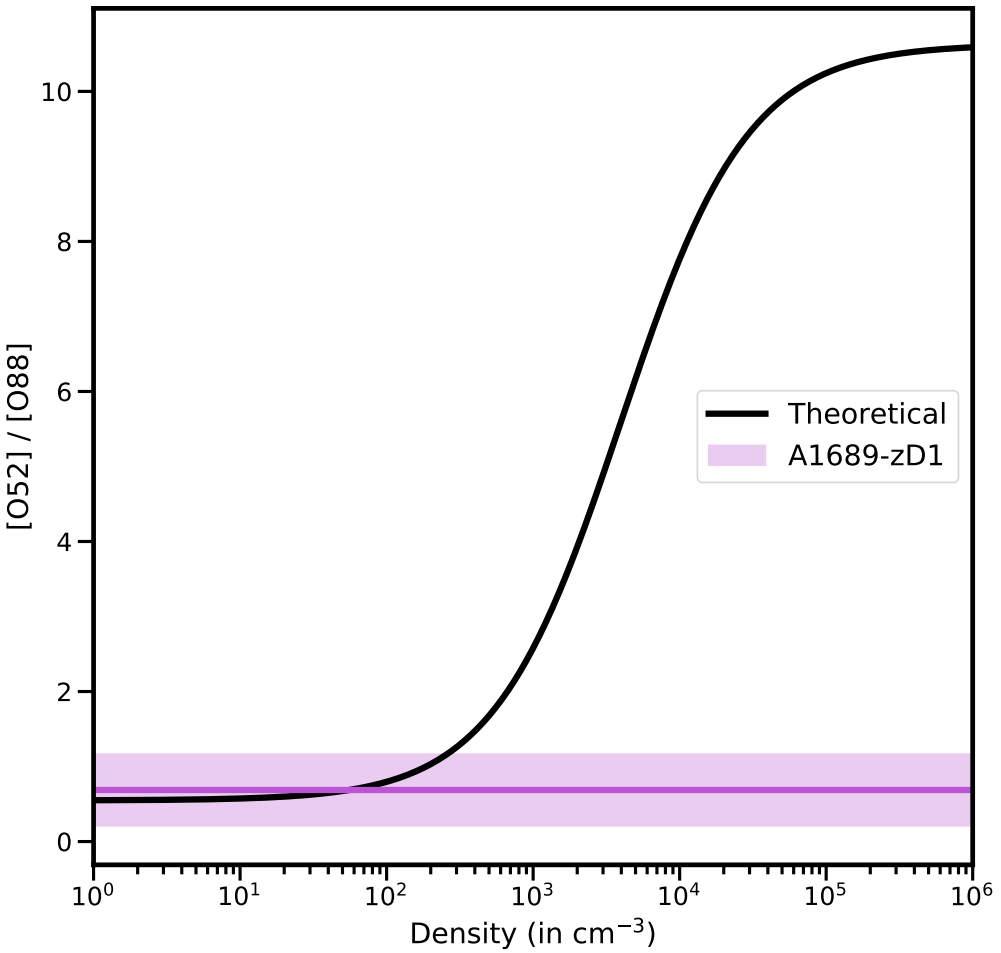


**Figure 9.3:** Theoretical relationship between [O52]/[O88] ratio and density shown as a black curve with the ratio for A1689-zD1 along with $1\sigma$ uncertainty shown in purple. The intersection of the horizontal purple line and black curve gives the nominal density measurement of $n_e \sim 55\,\mathrm{cm}^{-3}$, and the intersection of the extreme ends of the horizontal shaded purple region with the black curve gives the uncertainty range on the density. In case of A1689-zD1, we are only able to derive an upper limit of $n_e \sim 260\,\mathrm{cm}^{-3}$.

### 9.3.2 Dust continuum ratio and $U$

The ratio of the continuum at 88 µm and 122 µm can be used to constrain $U$, with some dependence on the density (Rigopoulou et al., 2018). We assume a $1\sigma$ density range with an upper bound of 260 $\mathrm{cm}^{-3}$ from the [O III] line ratio and a lower bound of about 10 $\mathrm{cm}^{-3}$ (corresponding approximately to a uniform distribution of $2 \times 10^{10}\, M_\odot$ in gas over the galaxy area). While this lower bound is somewhat arbitrary, it is the upper density bound that influences how low the metallicity can be. A lower density would result in higher metallicity and ionisation parameter. In Fig. 9.4, we plot the continuum ratio as a function of $\log U$ based on CLOUDY modelling over these density bounds from Pereira-Santaella et al. (2017). We show the ratio for A1689-zD1 with $1\sigma$ uncertainty regions. The extreme values of this uncertainty region are then propagated through the model at the extreme values of the density range derived in Sec. 9.3.3. From this, we infer a value of $-1.7 \lesssim \log U \lesssim -0.8$ within the $1\sigma$ uncertainty range.

### 9.3.3 [O88]/[N II] ratio and the metallicity

Since the [O88] and [N II] lines have similar critical densities, their ratio is nearly independent of the density. However, it does depend on $Z$ and $U$. Fig. 9.5 plots the ratio as a function of $Z$ for different model tracks of $\log U$, once again using the Pereira-Santaella et al. (2017) model. While the model does hold beyond $\log U > -2$, this parameter space was only explored in their work for galaxies with an active galactic nucleus (AGN). Non-AGN galaxies generally do not have $\log U > -2$, but A1689-zD1 appears to be an exception with a high $\log U$ despite not having any appreciable AGN activity. We therefore extrapolate the non-AGN Pereira-Santaella et al. (2017) model plot to higher values of $U$ to accommodate the measurements for A1689-zD1. Since these extrapolated model values are in agreement with the numbers in the Harikane et al. (2020) models presented below, which is also CLOUDY based, and does extend all the way up to $\log U = -0.5$, we are confident that the extrapolation is valid.

As before, the ratio for A1689-zD1 is indicated with the $1\sigma$ uncertainty regions. Once again, we derive the uncertainty range on metallicity by propagating the extreme values of the uncertainty region on the [O88]/[N II] ratio through the model curves at the extreme values of the $\log U$ measurements from Sec. 9.3.2. We thus find $0.9 \lesssim Z/Z_\odot \lesssim 1.3$. As mentioned in Sec 9.3.2, if we were to allow lower densities, $U$ and in turn, $Z$, would be higher.

For comparison, we use models from Harikane et al. (2020) with metallicity-dependent N/O and C/O ratios. These are plotted in Fig. 9.6. The model assumes that the nitrogen-to-oxygen abundance ratio depends on the metallicity due to secondary nucleosynthesis (see Sec. 10.2). This in turn uses the relation presented in Kewley et al. (2019) in the same

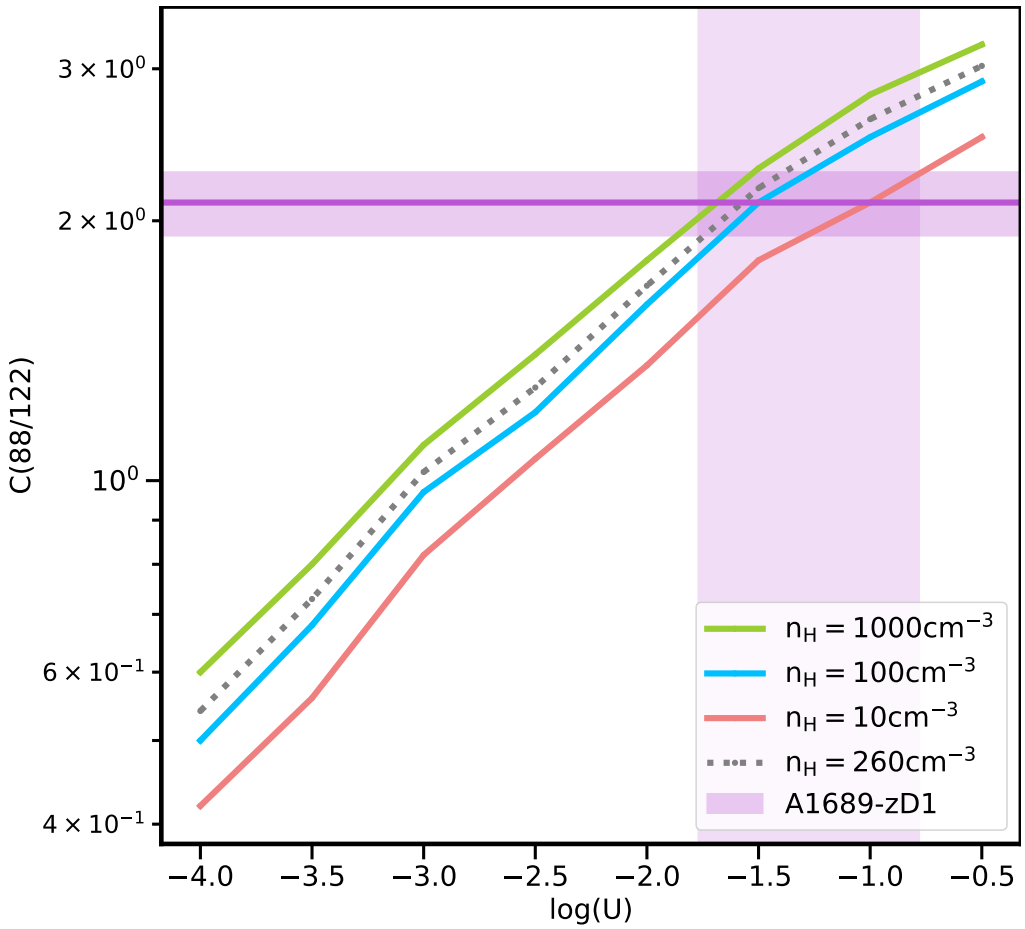


**Figure 9.4:** [O88] to [N II] continuum ratio as a function of $U$ and $n_H$. Figures from Rigopoulou et al. (2018) re-created with permission. Measurement for A1689-zD1 is shown as a purple line with the $1\sigma$ uncertainties depicted as a shaded purple region. As in Fig. 9.3, the uncertainty range on $\log U$ is given by the intersection of the extreme ends of the horizontal shaded purple region with the model curves corresponding to the extreme values (dotted grey curve for upper limit and red curve for lower limit) of our density estimate from Sec. 9.3.1.

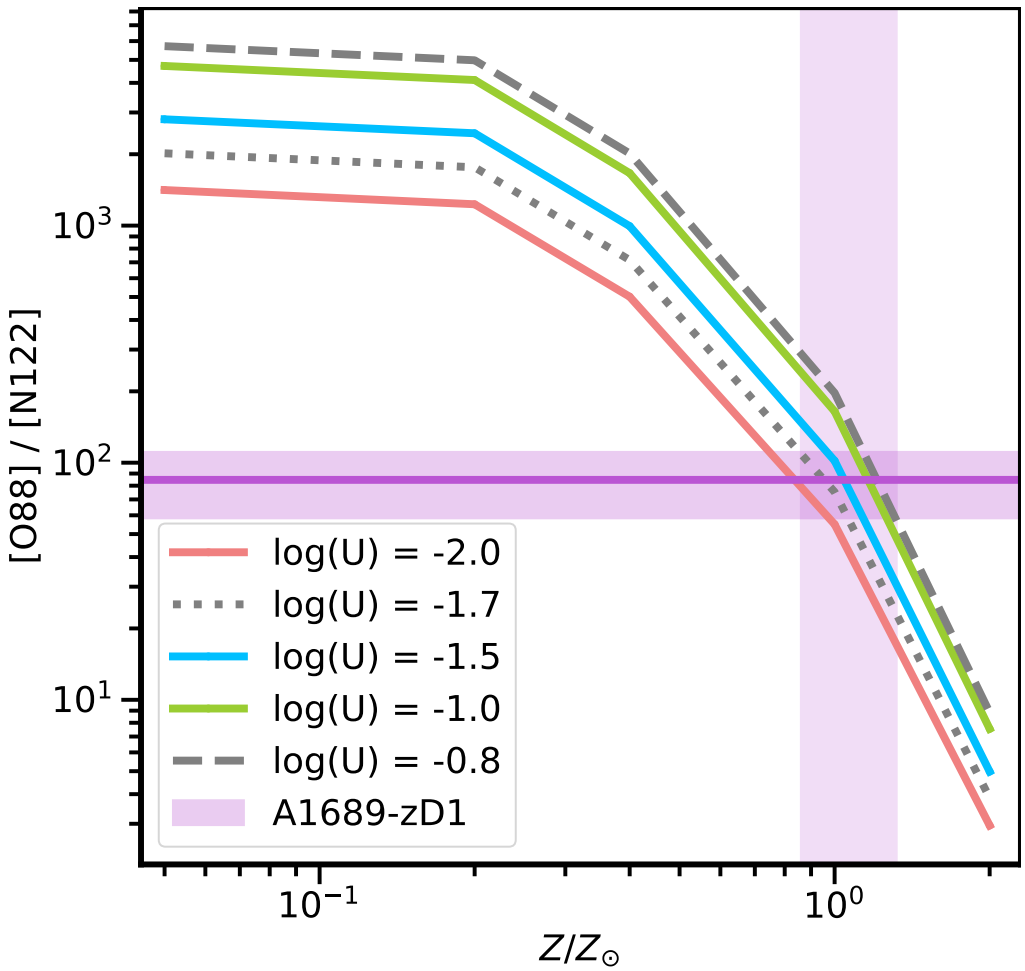


**Figure 9.5:** [O88] to [N II] line ratio as a function of $U$ and Z (Adapted from Rigopoulou et al. 2018 and extrapolated above -2.0). Measurements for A1689-zD1 are shown in purple, just as in Fig. 9.4. Also as in Fig. 9.4, the uncertainty range on $\log U$ is given by the intersection of the extreme ends of the horizontal shaded purple region with the model curves corresponding to the extreme values (dotted grey curve for lower limit and dashed grey curve for upper limit) of our $\log U$ estimate from Sec. 9.3.2.

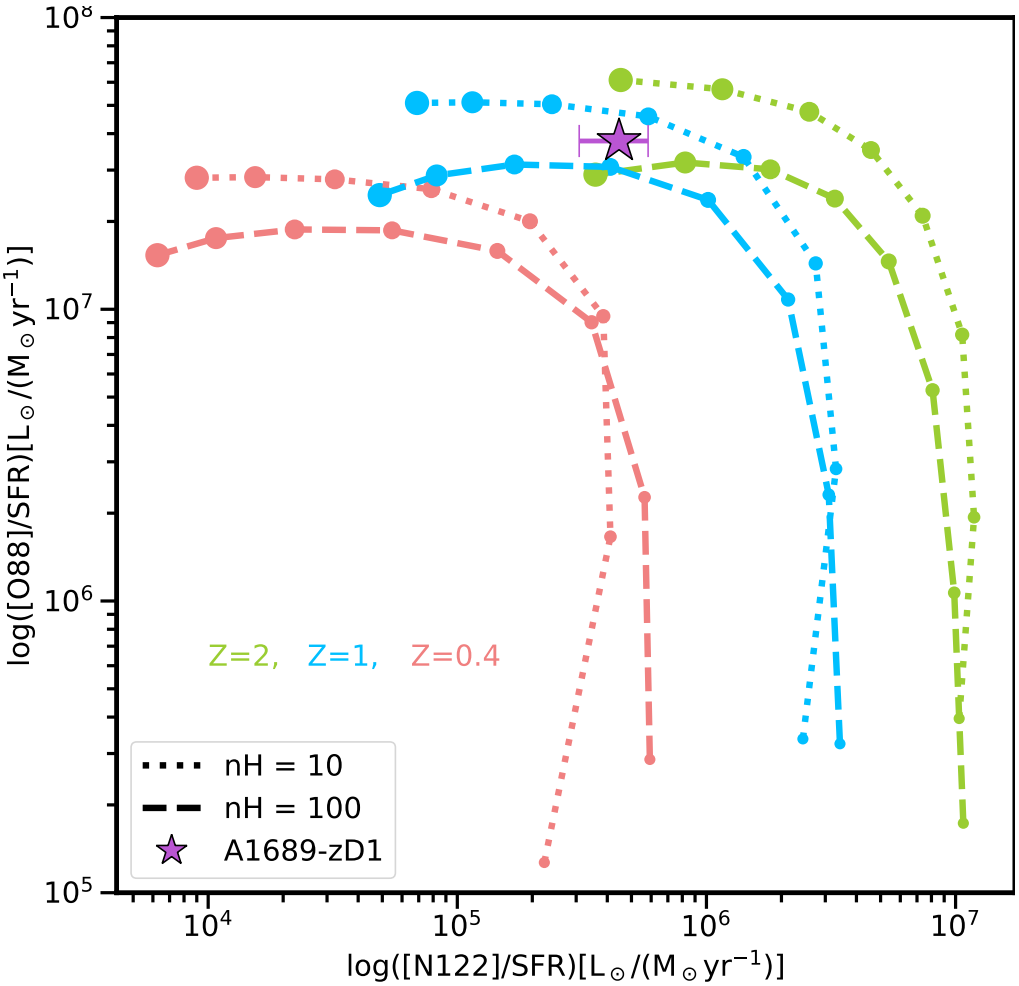


**Figure 9.6:** Model curves at various metallicities and densities for the [O88] luminosity/SFR ratio as a function of the [N II] luminosity/SFR ratio, based on Harikane et al. (2020). Increasing marker size represents an increase in $\log U$, within the range -4 to -0.5. The measurements for A1689-zD1 are shown as a purple star with uncertainties.

manner as Nagao et al. (2011). With this model, we find $Z/Z_{\odot} \sim 1$ to 2, and $\log U \sim -0.5$ to $-2$ (with $n_{\rm H} \sim 10$ to $100\,{\rm cm}^{-3}$) roughly consistent with the estimates based on Rigopoulou et al. (2018).

Despite both models being CLOUDY-based, the slight difference in metallicity estimate may arise from the different assumptions made in each one. For instance, Harikane et al. (2020) assumes a Chabrier initial mass function (IMF) and Pereira-Santaella et al. (2017) assumes a Kroupa IMF. In addition, we use a modified Harikane et al. (2020) model with metallicity-dependent nitrogen abundance, but a similar modification was not made for Rigopoulou et al. (2018) model. Regardless of these differences, metallicities significantly below the solar value do not reproduce our line ratios with either the Rigopoulou et al. (2018) or Harikane et al. (2020) model.

Nonetheless, there is some uncertainty associated with the model curves

presented here. Firstly, there is some scatter in the N/O abundance to metallicity conversion (e.g. Liang et al., 2006). Additionally, CLOUDY model curves have a model uncertainty of the order 10–20 per cent as discussed in Pereira-Santaella et al. (2017), comparable to metallicity models based on optical emission lines. Although, as discussed in e.g. Croxall et al. (2013), models relying on FIR lines remove the heavy dependence on temperature which plagues optical emission lines.

## 9.4 [O88]/[C II] ratio and the PDR covering fraction

The ionisation energies of [O III] (35.1 eV) and [N II] (14.5 eV) are higher than that of H (13.6 eV), whereas the ionisation energy of [C II] (11.2 eV) is lower than that of H. Hence, the [C II] emission comes from the cold atomic components, photo-dissociation regions (PDR), and H II regions, whereas the emission from the other three lines comes exclusively from the H II regions. Therefore, the ratio of [C II] to any of the other three lines can be used to estimate the PDR covering fraction, i.e. the extent of the ionised H gas compared to the neutral H gas (e.g. Cormier et al., 2019; Harikane et al., 2020).

In Fig. 9.7, we plot model curves for [C II] luminosity assuming PDR covering fractions of 0 and 1. The measurements for A1689-zD1 favour a model with PDR fraction close to 1, i.e. dominated by neutral atomic gas.

## 9.5 Dust-to-metals ratio

The total gas mass for A1689-zD1 is based on the sum of the atomic and molecular masses. We determine the atomic gas mass from the relation between the [C II] line luminosity, metallicity and the atomic gas mass from Heintz et al. (2021). We find $M_{H\,I} = 1.7^{+0.7}_{-0.5} \times 10^{10}\,M_\odot$. This includes the scatter in the relation and the statistical error added in quadrature.

Assuming most of the gas is in the atomic phase, the total gas mass is between 1.2 and $2.4 \times 10^{10}\,M_\odot$. Using a solar metal fraction of about 1/100 and a dust mass of $1.7^{+1.3}_{-0.7} \times 10^7\,M_\odot$ (Bakx et al., 2021), the corresponding dust-to-metals mass ratio (DTM) for A1689-zD1 is around 0.1. If there is significantly more gas in the system, say in the molecular phase, this will make the DTM even lower.

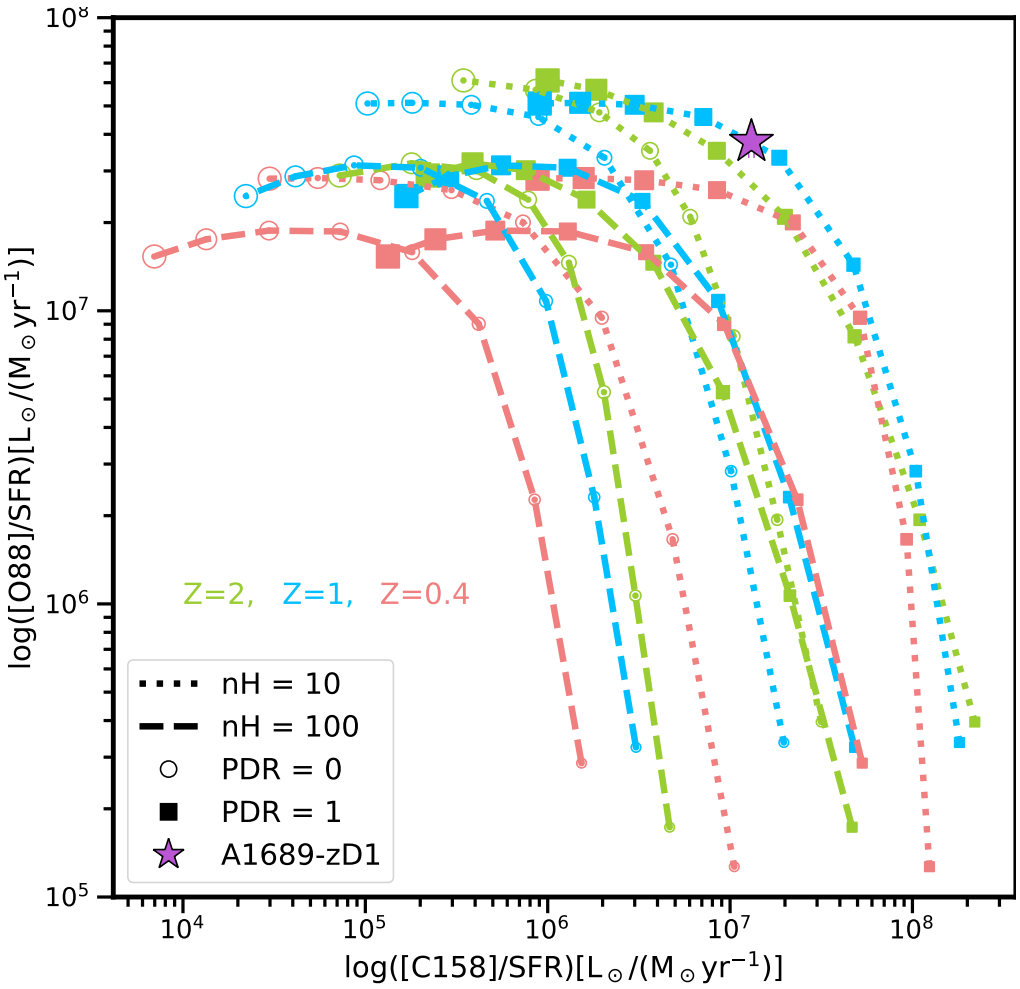


**Figure 9.7:** Model curves based on Harikane et al. (2020) for the [O88] luminosity/SFR ratio as a function of the [C II] luminosity/SFR ratio, assuming a PDR covering fraction of 0 (open circles), and 1 (filled squares). The $\log U$ range is the same as in Fig. 9.6, and measurements for A1689-zD1 are shown as a purple star just as in Fig. 9.6.

# Chapter 10

# Discussion

Several striking features are derived from the line ratios reported here. First, the metallicity is close to solar, which deviates strongly from the expected mass-metallicity evolution towards high-$z$.

Second, the nitrogen abundance is in excess of oxygen, indicating that the star-formation in the galaxy must be old enough to have produced secondary nitrogen through intermediate mass stellar envelopes, i.e. at least 250 Myr (Henry et al., 2000), pushing the formation age of the system back to $z > 10$.

Third, though this system is known as a prototypical dusty normal galaxy at this epoch, it seems to be deficient in dust compared to its total metal content.

## 10.1 Evolution of metal abundance

The most reliable metallicity estimates for star-forming galaxies come from back-lighting absorption studies, e.g. gamma-ray burst afterglows. All show metallicities substantially below 0.1 solar (Salvaterra, 2015) at $z \sim 6$. With some assumptions on density and temperature, Jones et al. (2020b) have estimated metallicities for a handful of $z > 7$ galaxies using the relative strength of the [O88] line to the total SFR and find metallicities ranging from 8–36 per cent of the solar value. Using a similar method to the one used here, but assuming $\log U$, Novak et al. (2019) find solar or possibly super-solar metallicity for the ISM of the host galaxy of the quasar J1342+0928 at $z = 7.54$, demonstrating that such a high metallicity is not unique at $z > 7$. Over the next 13 Gyr, if such a high metallicity galaxy is to increase its mass, it must do so mainly via dry mergers and not through a lot of star formation which would lead to supernova explosions that would substantially increase the metal content.

### 10.1.1 The fundamental metallicity relation

Galaxies up to $z \sim 2.5$ lie on a plane in 3D space spanning $M_*$, $Z$, and SFR. While there appears to be no evolution between local SDSS galaxies at $z \sim 0$ and those at $z \sim 2.5$, there is some evolution above $z \sim 2.5$ (Mannucci et al., 2010). We do not know how early these relationships are set up in galaxies, but galaxies at $z \sim 3$ appear to lie 0.6 dex below the metallicity prediction of the lower-$z$-calibrated FMR from Mannucci et al. (2010). Other studies have also found an evolution of the FMR relation with redshift (e.g. Stott et al., 2013; Torrey et al., 2018; Sanders et al., 2021).

Given the stellar mass and SFR for A1689-zD, its metallicity is substantially higher than the $z \sim 3$ FMR by $\sim 1.25$ dex, and even the $z \sim 0$ FMR by $\sim 0.6$ dex. Hence, the measured metallicity of A1689-zD1 is inconsistent with the trend suggested by Mannucci et al. (2010) by about an order of magnitude in metallicity. A revised $z \sim 0$ FMR parameterisation was presented by Curti et al. (2020), but A1689-zD1 deviates from this relation as well by about 1 dex.

The reason for the deviation may be an inaccurate estimate of the stellar mass. The current value of $2 \times 10^9\,\mathrm{M}_\odot$ is determined from rest-frame optical SED fitting, which could be heavily dust-obscured. The SFR of A1689-zD1 is more than 90 per cent obscured. While the obscuration of the stellar mass is unlikely to be as high as this, it could still be substantial. With a stellar mass of $10^{10}\,\mathrm{M}_\odot$, i.e. a factor of 80 per cent obscuration of the stellar mass, the deviation from the $z \sim 0$ FMR decreases to only 0.1 dex (although the deviation from the $z \sim 3$ FMR is still 0.7 dex). A stellar mass at least as large as the gas mass is required to produce all the metals in a solar metallicity system assuming a Chabrier or Kroupa IMF. Therefore such a high stellar mass is reasonable. However, it is hard to imagine dust obscuration much greater than this.

Another potential reason for the discrepancy might be the assumed N/O ratio in our models based on Rigopoulou et al. (2018) and Harikane et al. (2020). Both models assume the relation between the N/O ratio and metallicity calibrated in the local Universe. However, we do not know the N/O-metallicity relation at $z \sim 7$. Some studies (e.g. Queyrel et al., 2009; Yabe et al., 2015) report a possible increase of the N/O ratio at fixed metallicity at redshift $z \sim 1.5$, while others do not at $z \sim 2$ (Kojima et al., 2017). If the N/O ratio does evolve, the estimated metallicity would decrease, and become more consistent with the fundamental metallicity relation.

## 10.2 Nitrogen excess and the age of A1689-zD1

The metallicity estimate derived from the [O88]/[N II] ratio depends on the overabundance of N with respect to O (Rigopoulou et al., 2018; Pereira-Santaella et al., 2017), a consequence of secondary nitrogen production that only becomes dominant at $Z/Z_{\odot} \gtrsim 0.25$ (e.g. Vincenzo et al., 2016; Pilyugin et al., 2014).

Henry et al. (2000) argue that the secondary production of nitrogen principally occurs in the asymptotic giant branch (AGB) phase of intermediate mass stars (4–8 $M_{\odot}$), while O and C production continues to be dominated by high mass stars or type II supernovae. This leads to an increase in the N/O ratio with increasing abundance above $Z/Z_{\odot} \gtrsim 0.25$. However, it also introduces a delay of about 250 Myr, the main-sequence lifetime of these intermediate mass stars, before the N/O ratio increase can occur.

The fact that we observe a relatively low [O88]/[N II] ratio, and from it infer a metallicity significantly above 0.25 solar, suggests that the stellar age of this galaxy is at least several hundred million years. The galaxy must have therefore started forming stars at $z > 10$. This is somewhat at odds with the stellar age inferred from the SED analysis ($\sim 80$ Myr). However, as argued above, much of the stellar mass may be completely obscured.

The stellar mass inferred from the SED fitting is only detected as far as 4.6 $\mu$m, corresponding roughly to the $V$-band in the rest-frame. As indicated by the 80–90 per cent obscured SFR fraction, we can infer that the average extinction to most sightlines in the galaxy is high. As also indicated by the relatively modest extinction in the UV-bright parts of the galaxy, the dust distribution is likely very patchy, with some low obscuration regions, and most of the galaxy completely extinguished (for example, a dust mass of $2 \times 10^7$ $M_{\odot}$ spread over about 1 $kpc^2$ gives an $A_V \sim 200$ Watson 2011). This suggests that the stellar mass of $2 \times 10^9$ $M_{\odot}$ inferred from the SED is only a lower bound, and the real stellar mass could be up to an order of magnitude higher. A stellar mass of $10^{10}$ $M_{\odot}$ would lead to a characteristic age of about 300 Myr, consistent with the age required for the N/O overabundance.

We therefore suggest two things from these considerations: that A1689-zD1 may have a much higher stellar mass than previously inferred, and that its stellar age is $\gtrsim 300$ Myr. Hence, it must have started forming stars at a significant rate at $z > 10$. This is consistent with the claims for significant $z > 10$ star-formation inferred from candidate $z \sim 9$ galaxies (e.g. Laporte et al., 2021).

## 10.3 Low dust formation efficiency at z > 7

With a metallicity estimate in hand, we can address the question of the dust-formation efficiency of a galaxy at $z \gtrsim 7$ for the first time. We calculated in Sec. 9.5 a dust-to-metals mass ratio of about 0.1. This is significantly lower than the MW value. For a MW gas-to-dust ratio of 150 (Galliano et al., 2018), suitable for galaxies close to solar metallicity, the corresponding dust mass in A1689-zD1 for its inferred gas mass should be 1–2 $\times$ $10^8$ $M_\odot$, an order of magnitude higher than the measured value of $1.7^{+1.3}_{-0.7} \times 10^7$ $M_\odot$.

Although there have been suggestions that the formation of dust may be less efficient at low metallicity (De Cia et al., 2016; Galliano et al., 2018), at solar metallicity, dust-formation efficiency is observed to be high. In other words, the DTM is expected to be close to the MW value of 0.5 at metallicities at least down to about 0.3 dex below solar, as is observed in low redshift galaxies (De Vis et al., 2019). The small number of estimates from emission-line galaxies at $z \sim 2$ (Shapley et al., 2020) suggest that the DTM is constant at about 0.5 to that redshift at high metallicity too, with the caveat that for those galaxies the molecular mass was assumed to represent all the gas. Estimates of the DTM for systems detected in absorption indicate both a dependence on metallicity (De Cia et al., 2016) and no metallicity dependence (Zafar & Watson, 2013; Wiseman et al., 2017).

Regardless, A1689-zD1 is therefore a unique case, indicating a low dust formation efficiency in spite of the high metallicity. The low dust formation efficiency could point to a gas mass much lower than we have inferred, indicating a breakdown of the [C II]-HI relation of Heintz et al. (2021), or a dust formation timescale longer than the stellar mass build-up or nitrogen-enrichment timescale of $\sim$ 250 million years, or possibly a lack of high-emissivity dust originating in e.g. AGB stars. One caveat here is indeed the uncertainty in the emissivity of the dust. Local studies of the dust emissivity or dust mass absorption coefficient suggest lower emissivity by up to a factor of two in high density or higher temperature environments (Bianchi et al., 2022; Clark et al., 2019). This factor would alleviate some of the tension we observe here, though not eliminate it entirely.

Another way to resolve the tension would be to reduce the inferred metallicity. Reducing the metallicity by a factor of several, coupled with lowering the dust emissivity, could be enough to replicate the MW DTM. However, this would require either that the [N II] line luminosity is over an order of magnitude lower than our estimate or that the N/O line ratio-to-metallicity conversion (Rigopoulou et al., 2018; Harikane et al., 2020) is very different at this redshift (see Sec. 10.1.1)

## 10.4 [C II] deficit and the initial mass function

We find no [C II] deficit (e.g. Hodge & da Cunha, 2020) in A1689-zD1, similar to some other massive galaxies at $z \sim 7$ (e.g. Capak et al., 2015; Schaerer et al., 2020; Schouws et al., 2022a). Katz et al. (2021) claim that the deficit comes from low C/O abundance at high redshift, which in turn arises from enrichment by low metallicity core-collapse supernovae with a top-heavy IMF with no AGB stars to provide carbon. Since most AGB stars take $\gtrsim$ 1 billion years to contribute substantially to the ISM, the presence of [C II]-bright sources at $z \sim 7$ militates against the hypothesis of a top-heavy IMF with carbon-deficient supernovae.

## 10.5 Metallicity variation across the galaxy

As the SNR and spatial resolution of the [N II] data is much lower than that of the other lines, we could not create a resolved metallicity map. However, considering the fact that the [C II] and dust emission are stronger to the northwest side while the *HST* emission is stronger to the southeast (Knudsen et. al.(in prep.)), the metallicity may vary across the galaxy. A distinct difference in the metallicity between the major components measured with higher SNR measurements could indicate that the system was in the process of merging (Knudsen et al., 2017; Wong et al., 2022).

# Chapter 11

# Conclusions

We have measured [O52] and [N II] for the first time in a reionisation-epoch galaxy. These measurements, coupled with previous measurements of [O88] and [C II], and several dust continuum detections, have allowed us to determine the electron density and metallicity of the galaxy, subject to modelling uncertainties.

A1689-zD1 appears to have approximately solar gas-phase metallicity, remarkably high and unusual for a normal galaxy at this epoch. The excess of nitrogen to oxygen indicates that the star-formation in this galaxy started at least 250 Myr earlier, i.e. at $z > 10$. The galaxy also appears to be atomic gas dominated, and to have a low dust-to-gas ratio for its metallicity, possibly hinting at a low efficiency for dust production in galaxies at this epoch.

## Acknowledgements

We thank the anonymous referee for insightful comments, and Shengqi Yang and Luca Di Mascolo for helpful discussions.

This paper makes use of the following ALMA data:
ADS/JAO.ALMA#2013.1.01064.S
ADS/JAO.ALMA#2015.1.01406.S
ADS/JAO.ALMA#2016.1.00954.S
ADS/JAO.ALMA#2017.1.00775.S
ADS/JAO.ALMA#2019.1.01778.S
ALMA is a partnership of ESO (representing its member states), NSF (USA) and NINS (Japan), together with NRC (Canada), MOST and ASIAA (Taiwan), and KASI (Republic of Korea), in cooperation with the Republic of Chile. The Joint ALMA Observatory is operated by ESO, AUI/NRAO and NAOJ. The National Radio Astronomy Observatory is a facility of the National Science Foundation operated under cooperative agreement by Associated Universities, Inc.

DW and SF are supported in part by Independent Research Fund Denmark grant DFF-7014-00017. The Cosmic Dawn Center is funded by the

Danish National Research Foundation under grant number 140. KK acknowledges support from the Knut and Alice Wallenberg Foundation. FR acknowledges support from the European Union's Horizon 2020 research and innovation program under the Marie Sklodowska-Curie grant agreement No. 847523 'INTERACTIONS'

## Data Availability

The data used in the paper are available in the ALMA archive at https://almascience.nrao.edu. The derived data and models generated in this research will be shared on reasonable request to the corresponding author.

# Part III

# ALPINE

This part of the thesis contains the following article:

## "The ALPINE-ALMA [C II] survey: Characterisation of Spatial Offsets in Main-Sequence Galaxies at $z \sim 4$–6"

Submitted to the Monthly Notices of the Royal Astronomical Society (MNRAS) in June, 2023, and undergoing moderate revisions prior to acceptance.

Authors: Meghana Killi, Michele Ginolfi, Gergö Popping, Darach Watson, Giovanni Zamorani, Brian Lemaux, Seiji Fujimoto, Andreas Faisst, Matthieu Bethermin, Michael Romano, Yoshinobu Fudamoto, Sandro Bardelli, Médéric Boquien, Stefano Carniani, Carlotta Gruppioni, Nimish Hathi, Eduardo Ibar, Gareth C. Jones, Anton Koekmoer, Ivanna Langan, Hugo Méndez-Hernández, Yuma Sugahara, Livia Vallini, and Daniela Vergani

# Chapter 12

# Abstract

The morphology of galaxies is shaped by stellar activity, feedback, gas and dust properties, and interactions with surroundings, and can therefore provide insight into these internal processes. In this paper, we study the spatial offsets between stellar and interstellar medium emission in a sample of 54 main-sequence star-forming galaxies at $z \sim 4$–6 observed with the Atacama Large Millimeter/submillimeter Array (ALMA) and drawn from the ALMA Large Program to INvestigate $C^+$ at Early times (ALPINE). We find no significant spatial offset for the majority ($\sim$ 75 percent) of galaxies in the sample among any combination of [C II], far-infrared continuum, optical, and ultraviolet emission. However, a fraction of the sample ($\sim$ 25 percent) shows offsets larger than the median by more than $3\sigma$ significance (compared to the uncertainty on the offsets), especially between [C II]-ultraviolet and ultraviolet-optical emission. We find that these significant offsets are of the order of $\sim$0.3–0.7 arcsec, corresponding to $\sim$1–6 kiloparsecs. These offsets could be the result of complex dust geometry, strong feedback from stars and active galactic nuclei, large-scale gas inflow and outflow, or a combination of these phenomena. However, our current analysis does not definitively constrain the origin. Future, higher resolution ALMA and *JWST* observations may help resolve the ambiguity. Regardless, since there exist at least some galaxies that display such large offsets, galaxy models and spectral energy distribution (SED) fitting codes cannot assume co-spatial emission in all main-sequence galaxies, and must take into account that the observed emission across wavelengths may be spatially segregated.

# Chapter 13

# Introduction

The redshift 6 to 4 era corresponds to the period between the end of reionisation of the Universe where the earliest galaxies lived (e.g. Fan et al., 2006; Dayal et al., 2018; Robertson, 2022), and the beginning of cosmic noon where the bulk of the Universe's stellar mass was created (e.g. Förster Schreiber & Wuyts, 2020). Somewhere between redshift 6 and 4, i.e., around the 1 Gyr mark, primordial galaxies transformed into modern galaxies, rapidly assembling their masses and reaching chemical maturity. This transition period is therefore of utmost interest to trace the evolution of galaxies from first light to the present day.

The most representative galaxies at $z \sim 4$–6 are those that populate the star-forming main sequence relation (between stellar mass, $M_\star$, and star-formation rate, SFR) at these redshifts (e.g. Noeske et al., 2007; Speagle et al., 2014; Popesso et al., 2022), and should hence be ideal to study the physics that led to the eventual creation of modern galaxies. Since observations based only on ultraviolet (UV) emission are limited by dust attenuation (Fudamoto et al., 2020, 2021), comprehensive studies of main-sequence galaxies and their dust properties require far-infrared (FIR) continuum observations with e.g. the Atacama Large Millimeter/sub-millimeter Array (ALMA). ALMA also allows the study of the cold gas component through observations of bright rest-frame FIR emission lines such as [C II] 158μm, a major coolant of the interstellar medium (ISM; Hollenbach et al., 1999; Wolfire et al., 2022), generally emitted from multiple gas phases (ionised, neutral, and molecular gas; Carilli & Walter, 2013; Vallini et al., 2013, 2017; Lagache et al., 2017; Zanella et al., 2018).

Understanding the physics occurring within galaxies requires the study of both stellar and ISM phases at high-resolution, but it is observationally expensive to conduct high-resolution studies at these redshifts. An alternative is to study the spatial offset between centroids of emission at different wavelengths, which can be done even with low-resolution observations. The presence or absence of spatial offset in a given galaxy can reveal how the stellar and ISM phases evolve and interact. Characterising offsets in a statistical sample of main-sequence galaxies can tell us what is normal

among high-$z$ galaxies, and separate the exceptional from the ordinary. We may then study the physics that produces these exceptions, and trace its influence on galaxy evolution.

A few recent studies (e.g. Hodge et al., 2012; Maiolino et al., 2015; Willott et al., 2015; Pentericci et al., 2016; Carniani et al., 2017; Laporte et al., 2017; Bowler et al., 2018; Carniani et al., 2018; Matthee et al., 2019; Fujimoto et al., 2020, 2022a; Schouws et al., 2022b; Bowler et al., 2022) have found spatial offsets of the order of a few kiloparsecs (kpc) between stellar emission (from H II regions/ionized diffuse gas traced by rest-frame UV continuum and [O III]) and ISM emission (from neutral/molecular gas traced by [C II]) in galaxies at $z \sim 4$–7. Several state-of-art zoom-in cosmological simulations have also consistently found spatial displacement of a similar scale between [C II]/IR bright regions and [O III]/UV bright regions in the ISM of z∼5–6 galaxies (e.g. Arata et al., 2018; Katz et al., 2017; Behrens et al., 2018; Katz et al., 2019; Pallottini et al., 2019; Sommovigo et al., 2020; Pallottini et al., 2022). While some predict that offsets should be commonplace, others do not.

In this context, a statistical observational study to identify what fraction of high-$z$, main-sequence galaxies display stellar-ISM spatial offsets is yet to be conducted. This knowledge is important because spectral energy distribution (SED) fitting models often assume an energy balance between emission in the UV and FIR (or at least that the emission in UV/optical is coupled to that in FIR) to derive galaxy properties such as stellar mass, star formation rate, and dust content (e.g. Da Cunha et al., 2008; Boquien et al., 2019). This assumption may not hold when there is a spatial offset causing a segregation of UV and FIR emission.

In order to conduct a systematic study of spatial offsets, we use the ALPINE-ALMA [C II] survey (ALMA Large Programme to INvestigate $C^+$ at Early times; Béthermin et al., 2020; Le Fèvre et al., 2020; Faisst et al., 2020), which is a statistically significant (see Sec. 14.1) sample of main-sequence galaxies at $z \sim 4$–6. In addition to the FIR properties from ALMA, ALPINE is also covered by a wealth of ancillary data from rest-frame UV to mid-IR, making it an ideal sample to perform this analysis.

The [C II] and FIR continuum emission from ALPINE trace the metal-enriched cold gas and the dust respectively (e.g. Gruppioni et al., 2020; Ginolfi et al., 2020a; Pozzi et al., 2021). We use the rest-frame UV emission in the F814W filter of the Advanced Camera for Surveys (ACS) observed with the Hubble Space Telescope (*HST*) over several surveys (see Sec. 14.1) as a tracer for the young, massive stellar population. We also include the emission in the K-band from the UltraVISTA survey (McCracken et al., 2012) which traces a slightly older stellar population (compared to that seen with *HST*/F814W). The K-band ($\sim 2.2\,\mu$m) emission may come from either the rest-frame optical or the near-UV part of a galaxy's spectrum, depending upon its redshift (between 330 nm and 400 nm for ALPINE),

but we refer to it as the "optical" emission throughout this paper.

We calculate spatial offsets between pairs of emissions, and provide a statistical characterisation of the number, significance, and size of the offsets. We then identify galaxies with significant spatial offsets between stellar and ISM emission, and investigate any potential correlations between offsets and galaxy physical properties, e.g. stellar mass, star-formation rate (SFR), or dust attenuation.

We adopt a Flat ΛCDM cosmology with $H_0 = 70\,\mathrm{km\,s^{-1}\,Mpc^{-1}}$, $_M$ = 0.3, and = 0.7. For this cosmology, 1" = 6.27 kpc at $z = 5$, i.e., the mean redshift of our study.

# Chapter 14

# Sample and Data Reduction

## 14.1 Basic properties of the full ALPINE sample

The full ALPINE (Project ID: 2017.1.00428.L; PI: O. Le Fèvre) sample consists of 118 main-sequence star-forming galaxies at $4.4 < z < 5.9$, excluding the low-transmission (for [C II]) atmospheric window between $4.6 < z < 5.1$. The targets were selected using spectroscopic redshifts based on Lyman-$\alpha$ and UV ISM lines (Faisst et al., 2020), and were drawn from the Cosmic Evolution Survey (COSMOS; Scoville et al., 2006a,b), the Extended Chandra Deep Field South (ECDFS; Cardamone et al., 2010), and the Great Observatories Origins Deep Survey (GOODS; Giavalisco & Team, 2003) fields. The galaxies span a range of stellar masses ($\log(M_\star/M_\odot) \sim 9$–$11$) and SFRs ($\log(SFR/M_\odot yr^{-1}) \sim 1$–$3$) as determined through spectral energy distribution (SED) fitting (Faisst et al., 2020).

The [C II] and FIR continuum data consist of ∼70 hours of ALMA Band 7 observations conducted in cycles 5 and 6. The ALMA data-cubes were reduced and calibrated using the standard Common Astronomy Software Applications (CASA; McMullin et al., 2007) pipeline. Each cube was continuum-subtracted in the *uv*-plane, and a line search algorithm was then applied to detect the [C II] line with SNR > 3.5. For further details on the data reduction, see Béthermin et al. (2020).

The ALMA data products (moment maps and continuum images) are publicly available through the ALPINE Data Release 1 repository[1]. ALPINE cubes and images have a pixel scale of 0.15 arcsec pixel$^{-1}$ and a $1\sigma$ sensitivity on the integrated [C II] luminosity $L_{[CII]}$ of $0.4 \times 10^8 L_\odot$ assuming a line width of 235 km s$^{-1}$. The smallest circularised beams of galaxies in the dataset are of the order of 0.8 arcsec, while the largest are of the order of 1.5 arcsec.

In addition to [C II] and FIR continuum images from ALMA, we use rest-frame UV images from *HST* taken with the Advanced Camera for

[1] https://cesam.lam.fr/a2c2s/data_release.php

| Tracer | Number | Fields |
|---|---|---|
| UV | 54 | COSMOS, GOODS-S, ECDFS |
| Optical | 45 | COSMOS |
| [C II] | 52 | COSMOS, GOODS-S, ECDFS |
| FIR continuum | 16 | COSMOS, GOODS-S, ECDFS |

**Table 14.1:** Number of galaxies in our sample with each tracer observation, and the fields in which the galaxies are located

Surveys (ACS) F814W filter (Scoville et al., 2006a; Koekemoer et al., 2007, 2011). These observations have a $3\sigma$ depth of $\sim$29 mag [AB], with a pixel scale of 0.06 arcsec pixel$^{-1}$, and all *HST* images are registered to Gaia DR2 (Faisst et al., 2020).

We also use optical images from the UltraVISTA survey (McCracken et al., 2012) Data Release 4 (Moneti et al., 2023). The spatial resolution is in the range 0.74–0.78 arcsec, with a seeing of $\sim$ 0.64 arcsec, and a limiting magnitude of 24.9 [AB] (computed as the $5\sigma$ limit in a 2.0 arcsec aperture, Moneti et al., 2019). These images have a pixel scale of 0.15 arcsec pixel$^{-1}$ (McCracken et al., 2012), the same as the ALPINE [C II] and FIR continuum images.

For further information on the reduction and properties of ALPINE ancillary data, see Faisst et al. (2020).

## 14.2 Our sample

Of the 118 ALPINE galaxies, 75 were detected in [C II] emission, and 23 in FIR continuum (21 galaxies have both [C II] and FIR continuum detection). Romano et al. (2021) performed a morpho-kinematic classification based on the [C II] emission to identify mergers and multi-component systems and found 23 such merging sources. In this work, we exclude these mergers as we cannot define a single centroid (see Sec. 15.2) to perform our offset calculation. While the analysis in Romano et al. (2021) identifies major mergers that can be discerned at our current resolution, there may still be minor or close mergers, satellites, accretion, and clumps at smaller scales. For the purpose of this paper, we will exclude the mergers identified as such in Romano et al. (2021), cross-checked with the "MER" class in Jones et al. (2021), which is a subset of mergers from Romano et al. (2021), and only consider the remaining population.

This "non-merging" ALPINE sample consists of 54 galaxies, 52 of which have [C II] detection, and 16 have FIR continuum detection (14 galaxies have both [C II] and FIR continuum detection). All 54 galaxies have UV observations with *HST*. 45 of these sources, covered by the COSMOS field,

have deep UltraVISTA observations in the K-band (the remaining 9 sources in ECDFS and GOODS-S are excluded as they are not detected or barely detected in K-band). 12 galaxies in COSMOS have detections in all four emissions. In Table 14.1, we show the distribution of the final sample, indicating the number of galaxies that have observations in the UV, optical, [C II], and FIR continuum.

# Chapter 15

# Methods

In this section, we describe the methods used in this work to calculate centroids of emission in the four emission tracers, and derive spatial offsets among them.

## 15.1 UV centroids

We used *HST* images taken with the ACS/F814W filter (see Sec. 14.1), tracing rest-frame UV emission at the redshift of our targets. The UV centroids were assumed as the *HST* RA and Dec coordinates from the Faisst et al. (2020) catalogue. For each galaxy, an astrometric correction is provided in this catalogue as $\delta$RA and $\delta$Dec values to be added to the *HST* coordinates so that the image is aligned with the Gaia DR2 (Mignard et al., 2018) catalogue. Faisst et al. (2020) find an additional scatter of $\sim$100 mas in both RA and Dec, which we use as the *HST* positional uncertainty. We therefore calculate the total UV centroid uncertainty as the sum in quadrature of uncertainty on RA and Dec, which amounts to $\sim$0.14 arcsec for all UV images.

## 15.2 Centroid fitting and uncertainty

For [C II], FIR continuum, and optical images, we find the centroid of emission and estimate uncertainties in the following way.

### 15.2.1 [C II] and FIR continuum

For each galaxy detected in [C II] or FIR continuum (or both), we crop the corresponding ALMA moment-0 and/or continuum maps into cutouts of $6.0 \times 6.0$ arcsec ($40 \times 40$ pixels) around the UV centroid position (see Sec. 15.1). To estimate the typical noise level in the image, we calculate the sigma clipped standard deviation of pixel values within an annulus of inner and outer radii of 4.5 and 9.0 arcsec (30 and 60 pixels). We use this to apply a $2\sigma$ masking to the cutout image and exclude pixels that are

below this significance level. For the pixels with significance $> 2\sigma$, we fit a two-dimensional, elliptical Gaussian of the form

$$f(x,y) = Ae^{-(a(x-x_0)^2+2b(x-x_0)(y-y_0)+c(y-y_0)^2)}, \tag{15.1}$$

where

$$a = \frac{\cos^2(\theta)}{2\sigma_x^2} + \frac{\sin^2(\theta)}{2\sigma_y^2}, \tag{15.2}$$

$$b = -\frac{\sin(2\theta)}{4\sigma_x^2} + \frac{\sin(2\theta)}{4\sigma_y^2}, \tag{15.3}$$

and

$$c = \frac{\sin^2(\theta)}{2\sigma_x^2} + \frac{\cos^2(\theta)}{2\sigma_y^2}. \tag{15.4}$$

Here, $x_0$, $y_0$ are the coordinates of the centre, $\sigma_x$, $\sigma_y$ are the Gaussian widths along each dimension, and $\theta$ is the counter-clockwise angle.

We use SCIPY.OPTIMIZE.CURVE_FIT (Virtanen et al., 2020) to perform the fitting. The initial guesses for the parameters $A$, $x_0$, and $y_0$ are obtained by finding the brightest pixel within a 1.5 arcsec (10 pixel) cutout around the coordinates of the UV centroids (see Sec. 15.1). The initial guesses for $\sigma_x$, $\sigma_y$ and $\theta$ are the same for all images, at 2 px, 2 px, and 0° respectively. Finally, we let CURVE_FIT fit a 2D Gaussian to the masked image starting with the above initial parameters. If the fit converges, the fit centroid is then defined as the centre of the 2D Gaussian, ($x_0$, $y_0$).

We find fit uncertainties using a bootstrapping method with 100 trials per galaxy. We first add random Gaussian (with mean $\sim$ 0 and $\sigma \sim$ noise level in the image) noise to each pixel in the input image for each trial, and create 100 "noisy images" per galaxy. For each noisy image, we repeat the 2D Gaussian fitting procedure described above, including the noise estimation, $2\sigma$ masking, initial guess, and Gaussian fit. We exclude trials where the fit fails to converge (which happens for $\lesssim$10 trials out of 100 in our analysis). Then the average centre position over all converged trials gives the final centroid position of the galaxy. The standard deviation among converged trials gives the $1\sigma$ fit uncertainty on the $x$ and $y$ positions of the centroid. The fit error is then obtained as the sum in quadrature of the $x$ and $y$ uncertainty.

As a sanity check, we also compare the brightest source pixel in each image (i.e., the "peak" pixel supplied as the initial guess on the $x$ and $y$ coordinates to the centroid fitting code) and the centre of light (SCIPY.NDIMAGE.CENTER_OF_MASS, Virtanen et al., 2020) with the centroid obtained from the fit. We find that the peak pixel and centre of light generally trace the fit centroid position.

One galaxy (DEIMOS_COSMOS_881725) shows multiple components in its FIR continuum image (see Fig. D.1 of Béthermin et al., 2020), which results in a 2D Gaussian fit without a well-defined centroid. We therefore exclude the FIR continuum emission of this galaxy from further analysis.

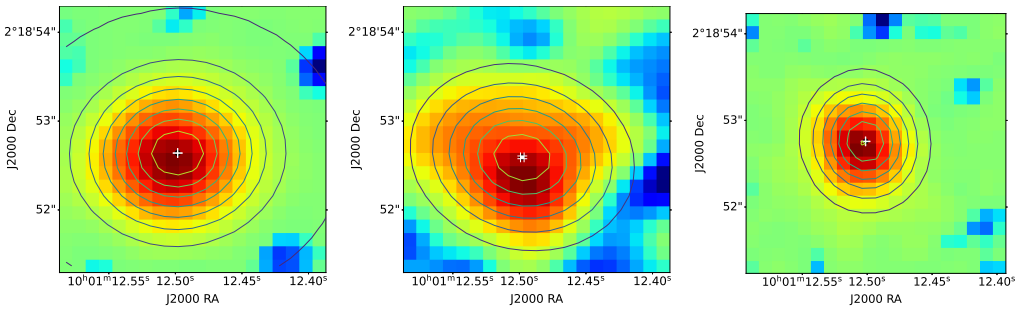


**(a)** [C II] fit **(b)** FIR continuum fit **(c)** Optical fit

**Figure 15.1:** 2D Gaussian fits (shown as contours) to find the centroids of (a) [C II], (b) FIR continuum, and (c) optical emission for the galaxy VUDS_COSMOS_5101218326. The fit uncertainty (without ALMA positional uncertainty; see Sec. 15.2) on the $x$ and $y$ position of the centroid is also indicated with black errorbars. ALMA and optical beamsizes are shown as filled white ellipses.

### 15.2.2 Optical

For optical images, we use the same procedure as we use for the [C II] and FIR continuum to find centroids and uncertainties, with the exception of the crop extent. We use various crop extents between 2.25 and 4.50 arcsec (15 and 30 pixels) to perform the optical centroid fits, so as to avoid other bright sources close to the target galaxy. Despite these measures, three galaxies (vuds_cosmos_510596653, vuds_cosmos_5101288969, and DEIMOS_COSMOS_843045) fail to fit or return a poor fit (either due to high noise in the image or the presence of a bright source very close to the target galaxy). We therefore exclude the optical emission of these galaxies from further analysis.

In Fig. 15.1, we show an example of centroid fits to emission in [C II], FIR continuum, and optical emission for the galaxy VUDS_COSMOS_5101218326.

### 15.2.3 Positional accuracy

In addition to the fit error, there is positional uncertainty associated with each ALMA pointing, which contributes to the uncertainty on the centroid position. The positional accuracy $\Delta p$ (in arcsec) is given by Eq. 3 of Faisst et al. (2020):

$$\Delta p = \frac{70\,000}{\nu B \sigma_{\rm peak}} \tag{15.5}$$

where $\nu$ is the observed frequency in GHz, $B$ is the maximum baseline length in kilometers, and $\sigma_{\rm peak}$ is the SNR of the peak emission pixel, which simplifies to

$$\Delta p = \frac{1060}{\sigma_{\rm peak}} \tag{15.6}$$

for the ALPINE data ($\nu = 330\,\mathrm{GHz}$, $B = 0.2\,\mathrm{km}$). We use this value as the positional uncertainty for the [C II] and FIR continuum centroids. The positional uncertainty for optical centroids is taken as 0.08 arcsec (McCracken et al., 2012).

### 15.2.4 Noise correlation at the beam scale

For ALMA images, noise is correlated on the scale of the beam (which is the same size as most of our marginally resolved objects), which introduces additional uncertainty in determining the centroid position. We estimate this uncertainty in the following way. We first inject several artificial 2D elliptical Gaussian galaxies of the same form as in Eq. 15.1 into each [C II] and FIR continuum image around the central source. The size of each of these simulated galaxies is between $\sim 1$ and 3.5 times the ALMA beam. In other words,

$$\sigma_x = k \times \frac{b_{\mathtt{maj}}}{2.355} \tag{15.7}$$

and

$$\sigma_y = k \times \frac{b_{\mathtt{min}}}{2.355}, \tag{15.8}$$

where $b_{\mathtt{maj}}$ and $b_{\mathtt{min}}$ are the full widths at half-maximum (FWHM) of the major and minor axes of the ALMA beam and $k$ is a scaling factor such that $\frac{k}{2.355}$ is a random number between 0.5 and 1.5.

The centre positions ($x_0$, $y_0$) of the simulated galaxies are also chosen at random within an annulus of 4.5 to 9.0 arcsec (30 to 60 pixels), around the centre of the image. We also ensure that no two simulated galaxies are within five standard deviations of each other so that the flux from one does not influence the fit of another.

Then, we fit each of these simulated galaxies in the same way as we fit the real galaxy (as described in Sec. 15.2) within a crop extent of 3.0 arcsec (20 pixels). We estimate the average centroid position over 100 trials. We calculate the difference between injected and fit centroid position for each simulated galaxy, and then the sigma clipped median of these differences for all the simulated galaxies in each image. This value is taken as the noise correlation uncertainty ( $_{\mathrm{NC}}$) for [C II] and FIR continuum centroids.

In Fig. 15.2, we show an example of an image with several simulated galaxies and the centroid fits for each. In Fig. 15.3, we plot $_{\mathrm{NC}}$ against the peak SNR of the image for [C II] and FIR continuum images. The plot follows an inverse relation, where the images with the lowest SNR show the largest deviation between injected and fit centroid positions. This is expected because given that the sizes of noise peaks and troughs are comparable to the ALMA beam, the morphology of a low SNR source will be more easily perturbed by the noise, resulting in a larger positional

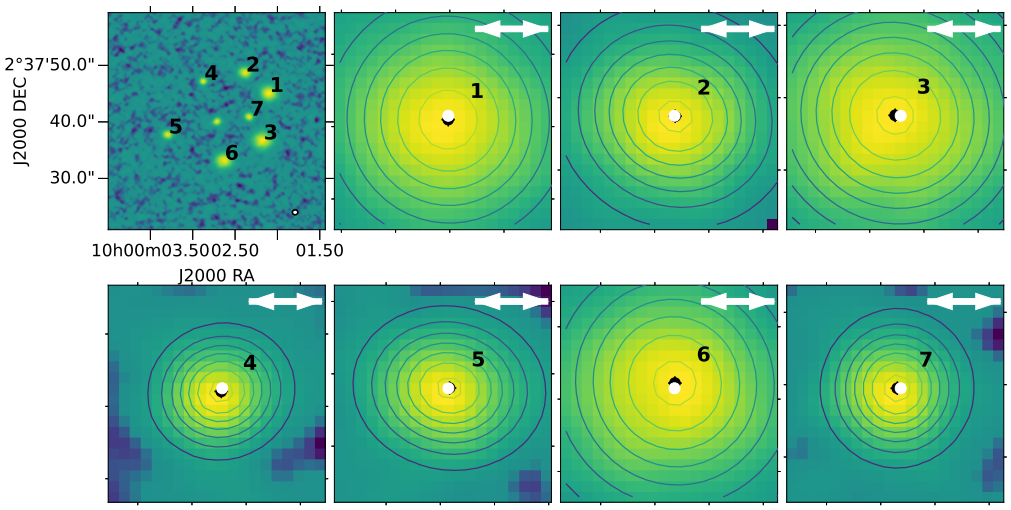


**Figure 15.2:** The ALMA [C II] image of the galaxy DEIMOS_COSMOS_873756 with several injected simulated galaxies (numbered) is shown in the first panel. The obtained centroid fits for each injected galaxy are shown in the remaining panels labelled with the corresponding number. The injected galaxy positions are shown in white, while the fit positions are shown in black (with fit errorbars). The white double headed arrows at the top right indicate 1 arcsec, shown for scale. The ALMA beam is shown in the first panel as a filled white ellipse.

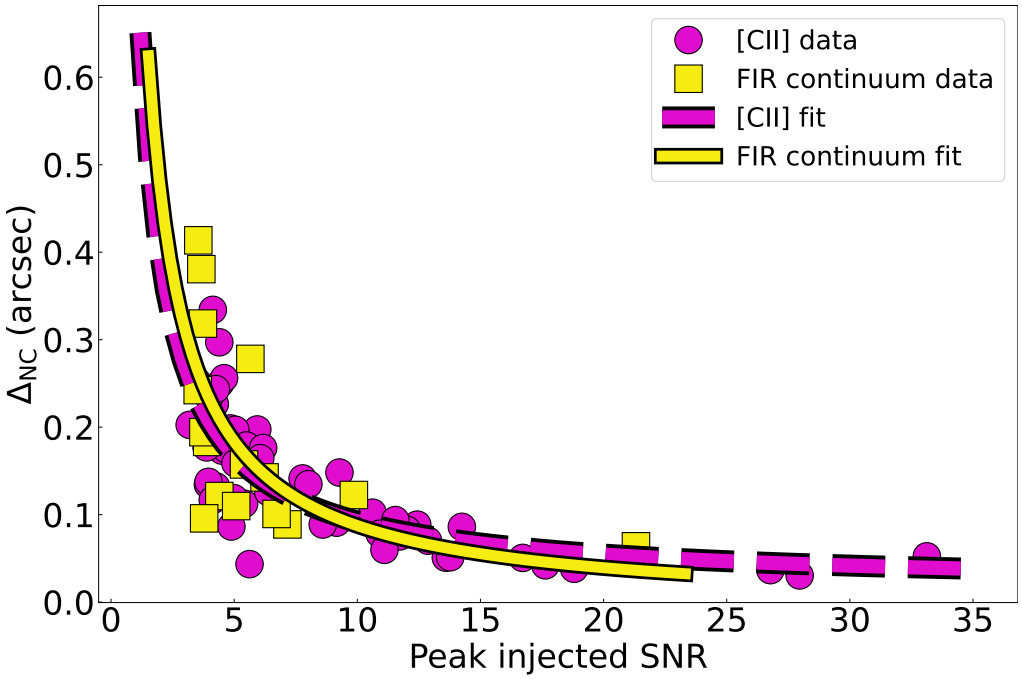


**Figure 15.3:** The inverse relationship between the noise correlation uncertainty ( $_{NC}$; see Sec. 15.2.4) and peak SNR of the injected Gaussian. The results for [C II] and FIR continuum images are shown in pink and yellow.

offset in the fit. Hence, the probability of positional offset of a fit has an anti-correlation with SNR.

### 15.2.5 Total uncertainty

The total uncertainty on the optical centroids is calculated as the sum in quadrature of the bootstrapped fit uncertainty (Sec. 15.2) and the positional uncertainty (Sec. 15.2.3). For the ALMA [C II] and FIR continuum centroids, the noise correlation term (Sec. 15.2.4) is also added in quadrature. In general, the positional and noise correlation uncertainties dominate over the fit uncertainty.

### 15.2.6 Spatial offsets

The spatial offset between any two emissions is defined as the spatial separation (in arcsec) between the calculated centroid positions of the two emissions. We use the ASTROPY (The Astropy Collaboration et al., 2022) function COORDINATES.SKYCOORD.SEPARATION to estimate this separation. The corresponding uncertainty on the offset is calculated as the sum in quadrature of the total positional uncertainties (see Sec. 15.2.5) on the centroids of the two emissions.

# Chapter 16

# Results

Given a Gaussian uncertainty $\sigma$ on each coordinate (RA and DEC), the expected distribution of offsets (r) is given by a 2D circular Gaussian of the form:

$$f(r)dr = 2\pi r \left(\frac{1}{2\pi\sigma^2}\right) e^{\left(-\frac{1}{2}\left(\frac{r}{\sigma}\right)^2\right)} dr \tag{16.1}$$

$$= \left(\frac{r}{\sigma^2}\right) e^{\left(-\frac{1}{2}\left(\frac{r}{\sigma}\right)^2\right)} dr \tag{16.2}$$

$$= \left(\frac{r}{\sigma}\right) e^{\left(-\frac{1}{2}\left(\frac{r}{\sigma}\right)^2\right)} d\left(\frac{r}{\sigma}\right) \tag{16.3}$$

Calculating the significance ($s$) as measured offset divided by the measured total uncertainty, i.e., $s = \frac{r}{\sigma}$, we have,

$$f(r)dr = se^{\left(-\frac{1}{2}s^2\right)} ds. \tag{16.4}$$

As the uncertainties for the various galaxies are not the same, we created a distribution in which each offset is normalised to its $\sigma$. We thus obtained an expected distribution of normalised offsets to compare with our observations (see Fig. 16.1). We adopt a $3\sigma$ threshold to identify offsets that are very likely to be real. In the following analysis, we will call these *significant* offsets. Based on the above expected distribution, the fraction of galaxies with no real offset having an observed significance of $s > 3$ should be 0.01. This corresponds to $0.01\times$ 54 (which is the total number of galaxies in our sample; see Sec. 14.2) $\sim 0.5$, i.e., less than 1 galaxy. Therefore, we can be confident that all the galaxies in our sample with $s > 3$ have significant offsets unlikely to occur by chance. It is important to note that a significant offset is not necessarily a *large* offset, but it is significant compared to the uncertainty. In other words, the sensitivity and accuracy of our analysis increases with SNR.

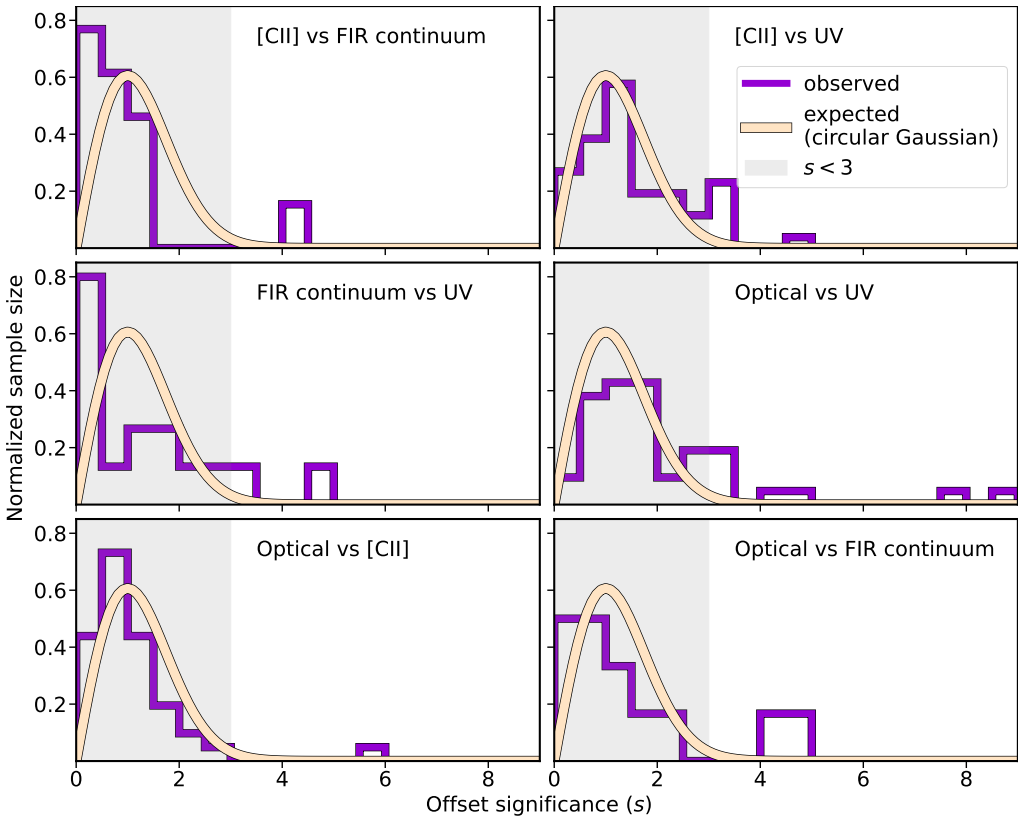


**Figure 16.1:** Normalised histograms of the significance ($s$) of observed spatial offsets between [C II]-UV, [C II]-FIR continuum, UV-FIR continuum, Optical-UV, Optical-FIR continuum, and Optical-[C II] emission are shown in violet. The cream-coloured curve is the expected distribution of offsets, modelled with a circular Gaussian (as described in Sec. 16)). Although the majority of galaxies lie within $3\sigma$ of the expected distribution (shown by the grey-shaded region), there still exists a tail of galaxies with significant offsets ($s > 3$).

## 16.1 Offset distributions

In Fig. 16.1, we show histograms of the significance of spatial offsets between combinations of [C II], UV, Optical, and FIR continuum. We plot the expected distribution as a normalised circular Gaussian (Eq. 16.4) and indicate our $3\sigma$ threshold using a grey shaded region. We find that for the majority of galaxies, the observed offsets could be caused by measurement uncertainties. However, some galaxies lie outside the expected distribution with a significance of $s > 3$.

Fig. 16.2 shows an example of one galaxy (DEIMOS_COSMOS_683613) with a significant offset ($s > 3$) and one (VUDS_COSMOS_5101218326) with no significant offset ($s < 3$). We see that one has all centroids close together (offsets $\lesssim 1.2$ kpc), while the other has FIR continuum centroid separated from the other centroids (offset $\sim$4 kpc). As the FIR continuum traces the dust, it appears that this second galaxy (DEIMOS_COSMOS_873756) has the bulk of its

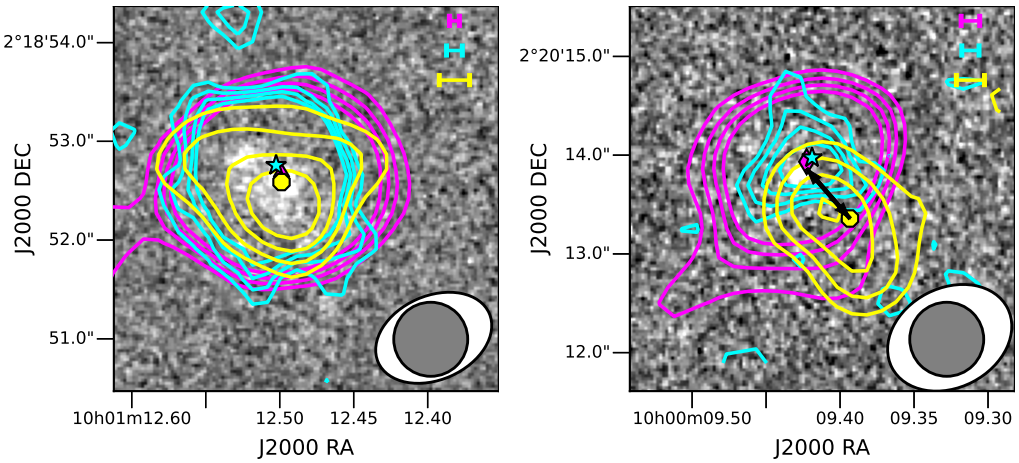


**(a)** No significant offset **(b)** Significant offset

**Figure 16.2:** (a) A galaxy (VUDS_COSMOS_5101218326) with no significant offset among any of the emissions (see Sec. 16) vs (b) a galaxy (DEIMOS_COSMOS_683613) with a significant offset between FIR continuum and all other emissions. UV *HST* image is shown as a grey-scale background with [C II] (fuchsia), optical (cyan), and FIR continuum (yellow) overlaid. The contours are drawn at 2, 3, 4, and 5 times the standard deviation (calculated in an annulus with radii of 4.5 and 9.0 arcsec (30 and 60 pixels), around the centre of the image). The centroids for each emission are marked in the same colour as the contours, and the spatial offset among them is indicated by a black double-headed arrow. The calculated total error (see Sec. 15.2.5) in each emission is indicated on the top right in the same colour as the contours. The ALMA ([C II] and FIR continuum) beam is shown as a filled white ellipse, and optical beam as a filled grey circle.

dust offset from stars and gas (both atomic and ionised gas as traced by [C II]). Several other significant offset galaxies are shown in Fig. A.1 of Appendix. A.1.

In Table 16.1, we show the number of galaxies in our sample that display such significant spatial offsets between pairs of emission tracers. We also specify the median offset and uncertainty for the full distributions of offsets, and the median of only the significant offsets in each distribution. We find the largest number of significant offsets between [C II]-UV and UV-optical. This may be because the uncertainties on centroids are smaller in UV and optical, and our sample size is largest in the UV, [C II], and optical. Overall, ∼25 per cent (14 galaxies) of our sample shows significant offsets between at least two emissions, while the remaining ∼75 per cent (40 galaxies) does not have significant offsets between any two emissions.

| Emission tracer pair | Median offset (arcsec) | Median uncertainty (arcsec) | Number of $s > 3$ galaxies (Total) | Median significant offset (arcsec) | (kpc) |
|---|---|---|---|---|---|
| [C II]-UV | 0.23 | 0.25 | 7 (52) | 0.35 | 2.19 |
| [C II]-FIR continuum | 0.11 | 0.18 | 1 (13) | 0.70 | 4.39 |
| FIR continuum-UV | 0.19 | 0.18 | 2 (15) | 0.53 | 3.32 |
| Optical-UV | 0.15 | 0.09 | 8 (42) | 0.36 | 2.26 |
| Optical-FIR continuum | 0.18 | 0.25 | 2 (12) | 0.65 | 4.08 |
| Optical-[C II] | 0.26 | 0.17 | 1 (41) | 0.60 | 3.76 |

**Table 16.1:** Number of galaxies with significant spatial offsets. The first column gives the two emission tracers between which we calculate the offset. Second and third columns give the sigma-clipped medians of the full distribution of offsets and uncertainties (Sec. 15.2) respectively. Fourth column gives the number of galaxies that show significant offsets (see Sec. 16) out of the number of galaxies for which we calculate this offset, and the last column gives the sigma-clipped median of only the significant offsets.

# Chapter 17

# Discussion

## 17.1 Relating spatial offsets to physical properties

Here we discuss several scenarios that may lead to the observation of spatial offsets in distant galaxies. Wherever possible, we plot galaxy physical properties such as specific star-formation rate (sSFR), stellar mass ($M_*$), UV continuum slope ($\beta$), etc. from the Faisst et al. (2020) and Béthermin et al. (2020) catalogues against the measured spatial offsets. We then look for trends in these plots that may reveal the phenomenon that is producing spatial offsets. These properties were derived using the `Le PHARE` fitting code (Arnouts et al., 1999; Ilbert et al., 2006; Arnouts & Ilbert, 2011) where galaxies with offsets were treated no differently than others. Although the ALMA data were not used in the SED fitting, if the offsets between short and long wavelengths are severe enough, it might affect the derived properties, which in turn would affect whether we observe correlations between offsets and physical properties. However, the implications that these extreme offsets have on SED fitting analysis and the galaxy properties derived are out of the scope of this paper.

In the following sections, we describe potential physical phenomena that may be driving the observation of spatial offsets (several of these effects may be related to each other). We start with the most likely scenarios, and then discuss other, less likely, but still plausible scenarios for completeness.

### 17.1.1 Feedback and outflows

Feedback from star formation, supernovae, or AGN might be physically pushing the enriched gas and/or dust away from the stars (Ceverino & Klypin, 2009; Maiolino et al., 2015; Vallini et al., 2017; Li et al., 2018; Torrey et al., 2020), which might then produce an observable spatial offset between UV/optical emission compared to the gas ([C II]) and dust emission (FIR continuum). Thus, we may expect a large offset in galaxies with high star-formation or AGN activity (assuming that enough time has

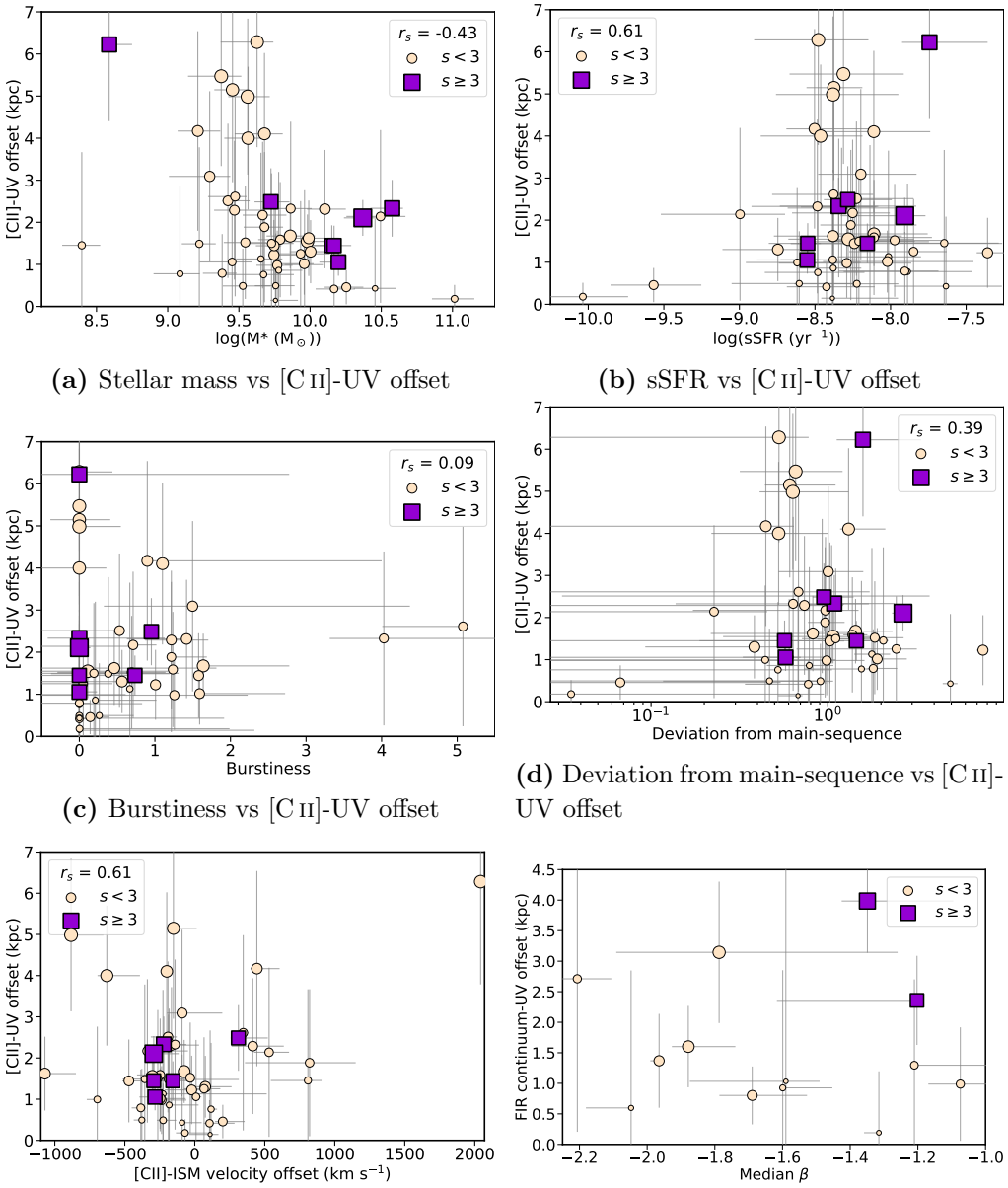


**(a)** Stellar mass vs [C II]-UV offset

**(b)** sSFR vs [C II]-UV offset

**(c)** Burstiness vs [C II]-UV offset

**(d)** Deviation from main-sequence vs [C II]-UV offset

**(e)** Velocity offset vs [C II]-UV offset

**(f)** Median $\beta$ vs FIR continuum-UV offset

**Figure 17.1:** Relating spatial offsets between [C II]-UV with galaxy physical properties: (a) Stellar mass vs [C II]-UV (b) SED-derived sSFR vs [C II]-UV (c) burstiness vs [C II]-UV (d) deviation from main-sequence vs [C II]-UV (e) Velocity offset between ISM absorption lines and [C II] vs [C II]-UV (f) median $\beta$ vs [C II]-UV. The measurements for the galaxies with significant offsets ($s \geq 3$; see Sec. 16) are shown as violet squares, while galaxies with no significant offsets ($s < 3$) are shown as cream-coloured circles (markersize is proportional to $s$). The uncertainties are plotted as grey lines. If there are three or more galaxies with significant offsets, the Spearman's rank coefficient $r_s$ for these is also given.

elapsed since the starburst for the feedback to push the gas/dust to large galactocentric distances). As the galaxies in ALPINE are selected to have low AGN activity (Shen et al., 2022), it is unlikely that the offsets seen here are due to AGN activity, but high star-formation activity can still clear out gas.

To test this idea, in Fig. 17.1b, we plot the total sSFR as a function of the [C II]-UV offset. We do not observe a clear trend between offset and sSFR. Carniani et al. (2017) study the spatial offset in BDF-3299, a Lyman-break galaxy at z=7.1 and compare it to other observations from literature (see fig. 6). They also do not find any clear correlations between SFR and spatial offset between [C II]/[O III] and UV.

In Fig. 17.1c, we now plot "burstiness" against the [C II]-UV offset. The burstiness parameter (Smit et al., 2016; Faisst et al., 2019; Atek et al., 2022) is calculated as a ratio between two SFR indicators: the Hα SFR obtained arising from young stars, and sensitive to star-formation on short-timescales (few Myr), and the UV SFR tracing the stellar continuum, which is sensitive to star-formation on longer timescales (few tens to hundreds of Myr). This parameter therefore measures how instantaneous the star formation is (Kennicutt & Evans, 2012), with a ratio above unity suggesting a recent burst, i.e., an episode of star-formation (Atek et al., 2022). Most of the ALPINE galaxies, and especially those with significant offsets, do not display burstiness (and even among the galaxies showing burstiness, we find no correlation with offset).

Next, in Fig. 17.1d, we plot the deviation from main-sequence against [C II]-UV offset. We compute the deviation as the ratio of the measured SFR vs that expected at the main-sequence, given the stellar mass, and assuming the Speagle et al. (2014) main-sequence relation at $z \sim 5$. We do not observe a clear correlation in any of these plots.

A consequence of strong feedback is gas outflow, which can be traced with [C II] emission (e.g. Cicone et al., 2015). Large-scale outflows (e.g. Bischetti et al., 2019; Ginolfi et al., 2020a; Pizzati et al., 2023) may be escaping the galaxy with enriched gas that glows in [C II] emission while the UV emission only traces the stars within the galaxy. Thus, the bulk of the [C II]-emitting metal-enriched gas may be located in a different region than the bulk of the UV-emitting stars. This may produce an observable offset much larger than the size (e.g. Baron et al., 2018) of the star-forming regions in the galaxy. In Fig. 17.1e, we plot the velocity offset between the [C II] and ISM absorption lines as a function of [C II]-UV spatial offset to check for correlation with outflow signatures. We again find no apparent trend.

### 17.1.2 Complex dust geometry and differential attenuation

The dust distribution across the galaxy may be non-uniform (Graziani et al., 2020; Sommovigo et al., 2020), with some highly obscured and some relatively dust-free regions. In this case, the UV/optical emission from the stars within the obscured regions is almost entirely absorbed by the dust, making them invisible to *HST* and VISTA. However, ALMA can still see the re-radiated light in FIR, and hence FIR continuum remains unaffected by the obscuration. Thus, we may observe an offset between the UV/optical emission probing only the dust-free regions compared to the FIR continuum emission probing obscured regions (e.g. Cochrane et al., 2021; Hodge et al., 2016; Behrens et al., 2018; Rivera et al., 2018). In Fig. 17.1f, we plot median UV continuum slope ($\beta$; measured using Calzetti et al. (2000) spectral range; see Faisst et al. (2020)) as a function of FIR continuum-UV offset to see if offsets correlate with dust obscuration. Although, it is important to note that since the $\beta$ slope is derived from UV emission, it cannot accurately measure the dust content of highly dust-obscured galaxies. Moreover, we currently only have two galaxies on this plot with significant offsets, so we require more dust continuum observations to produce large number statistics.

### 17.1.3 UV-dark or FIR-dark galaxies

Considering the situation of two galaxies in a close merger (not identified as such in kinematic analyses due to the limited spatial resolution), it may be that one of them has very low dust and metallicity and hence, only emits in UV-optical (e.g. Ouchi et al., 2013; Matthee et al., 2019; Romano et al., 2022), while the other is highly dust-obscured and thus, only emits in FIR (e.g. Bowler et al., 2018; Wang et al., 2019; Romano et al., 2020; Fudamoto et al., 2021; Talia et al., 2021; Fujimoto et al., 2022b). Hence, *HST* will only detect the UV emitting galaxy, whereas ALMA will only detect the FIR emitting galaxy. In such a scenario, not only would we fail to identify that there are two distinct galaxies in a close merger, introducing a bias in the estimation of the real merger fraction (Romano et al., 2021), we would also derive a "spatial offset" between the UV and FIR emission from two separate galaxies. If the derived offset is consistent with the size of a typical galaxy at $z \sim 5$, i.e., a few kpc (e.g. Fujimoto et al., 2020; Ribeiro et al., 2016), which is indeed the case for many of our $s > 3$ galaxies, then it is likely that we are talking about different regions within the same galaxy. This may be the complex dust geometry scenario discussed above or pristine gas inflows or past outflows with low metallicity and dust (hence invisible to ALMA), but with in-situ star formation (hence visible in UV), or accreting satellite clumps with obscured star-formation (visible in FIR)

nearby a less obscured galaxy (visible in UV) (Carniani et al., 2017).

### 17.1.4 Galaxy orientation and kinematics

The orientation of the galaxy on the sky may amplify the effects of uneven dust distribution. Some galaxies may be oriented on the sky such that we can directly observe the inner star-forming regions, e.g.: a face-on spiral with dust distributed evenly across the disk. Other galaxies might be partially dust-obscured from our point of view, e.g: an edge-on spiral with a dusty disk obscuring part of the central bulge. Whereas in the former case, centroids of the UV/optical emission and FIR continuum emission will be co-spatial, in the latter case, the UV/optical emission will arise from the unobscured part of the disk, while the FIR continuum centroid may be located near the part of the disk with the highest concentration of dust. Then, although both sources are physically the same kind of galaxy, we would interpret them as different kinds of objects based on the offset. We may be able to quantify the effects of galaxy orientation with higher spectral resolution by studying the [C II] line profile (e.g. Kohandel et al., 2019), or by observing the ALPINE galaxies across many wavelengths from UV to FIR. That said, at high-$z$, offset contribution from orientation effects should be small, especially given our resolution.

The kinematics of galaxies may also play a role in the observation of offsets. Two of our galaxies with significant offsets (DEIMOS_COSMOS_848185 and DEIMOS_COSMOS_873756) are classified as dispersion dominated in Jones et al. (2021). Some others (6 out of 14) were identified as having either compact or extended dispersion in Le Fèvre et al. (2020). Hence, there may be a correlation between the dispersion and spatial offset.

### 17.1.5 Uneven star-formation

Young and old stars are distributed differently in a galaxy (e.g. El Youssoufi et al., 2019); young stars are located only where current star-formation is taking place, while older stars (whose population grows as young stars age) are more spread out (Katz et al., 2017). This would produce an offset between UV and optical centroids. Another explanation for UV-optical offsets could be that in galaxies with non-uniform or clumpy star-formation (e.g. Guo et al., 2012; Hatsukade et al., 2015), UV light would trace the brightest star-forming regions (e.g. Papovich et al., 2005), whereas optical emission would include a more evenly distributed older stellar population, thereby producing an offset between the two emissions. We require higher resolution observations at longer wavelengths than UltraVISTA K-band (with e.g. *JWST*) to test these scenarios by observing an even older stellar population.

Overall, none of the plots in Fig. 17.1 show clear trends. Several more plots are presented in Appendix A.2, but in all cases, either the number of galaxies with significant offsets is too small to observe a correlation, or there is no apparent trend. Therefore, understanding which of these scenarios is driving the spatial offsets requires observations (e.g. Herrera-Camus et al., 2021; Chen et al., 2022) or simulations (e.g. Graziani et al., 2020; Rizzo et al., 2022; Pallottini et al., 2022) that resolve galaxies down to sub-arcsecond scales.

## 17.2 Consequences of significant spatial offsets

The prevalence of significant spatial offsets in high-$z$ galaxies may affect many commonly used relations at these redshifts. For instance, significant offsets between [C II] and UV emission could alter the [C II]-SFR relation (Schaerer et al., 2020; Romano et al., 2022; Ferrara et al., 2022) as the [C II] emission would arise from gas that is tracing a different region, away from the site of star formation. In Fig. 17.2, we plot the $L_{[\mathrm{CII}]}$-SFR relation and highlight the galaxies with significant [C II]-UV offsets. We see that the galaxies with significant offsets tend to lie above those without, thereby affecting the overall relation.

Similarly, FIR-UV offsets would affect the IRX-$\beta$ relation (e.g. Faisst et al., 2017; Popping et al., 2017; Narayanan et al., 2018; Fudamoto et al., 2020; Sommovigo et al., 2020; Boquien et al., 2022) as the UV emission may be tracing a different region of the galaxy compared to FIR emission (e.g. Casey et al., 2014; Gómez-Guijarro et al., 2018; Elbaz et al., 2018).

Furthermore, galaxy SED modelling codes, e.g. CIGALE (Burgarella et al., 2005; Noll et al., 2009; Boquien et al., 2019; Pacifici et al., 2023), MAGPHYS (Da Cunha et al., 2008), and FSPS (Conroy et al., 2009; Conroy & Gunn, 2010) assume an energy balance between UV and FIR emission. However, if the emission in FIR arises from a different region of the galaxy than the emission in UV (which may be a subset of the FIR emitting region), then the position and size of the aperture used for photometry must be carefully chosen to ensure that it encompasses both UV and FIR emitting components. Otherwise the energy balance does not hold in the presence of offsets, and SED-derived properties such as stellar mass and SFR would in turn be affected. Even for SED modelling where no energy balance is assumed, UV emission is used to get IRX-$\beta$, which is then assumed to be the dust content in FIR, but if emission does not originate in the same physical region in the galaxy, this assumption does not hold.

Sommovigo et al. (2022b) find that the SED derived SFR does not match the total UV and IR SFR for galaxies that have a high molecular index (Ferrara et al., 2022), which in turn may arise from spatially decou-

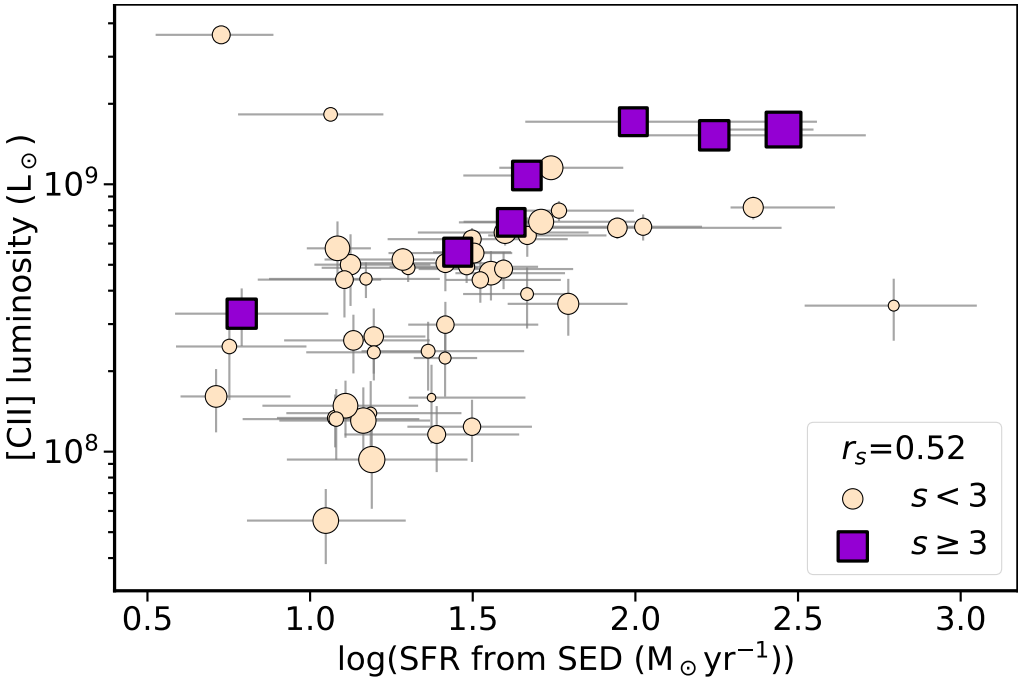


**Figure 17.2:** The $L_{[\mathrm{CII}]}$-SFR relation may be affected by the presence of significant spatial offsets. As in Fig. 17.1, the galaxies with a significant [C II]-UV offset are shown as violet squares, while those without significant offsets are shown as cream-coloured circles. Markersize increases with significance. The errorbars are shown in grey.

pled UV and IR emission. The galaxy with the largest discrepancy in their analysis (DEIMOS_COSMOS_873756; shown in Appendix Fig. A.1d) is one of the galaxies we find to have a significant spatial offset.

The deviations caused by spatial offset become even more prominent in the case of spatially resolved SED modelling (e.g. Wuyts et al., 2012; Sorba & Sawicki, 2018). Hence, the non co-spatial nature of emission should be accounted for in SED modelling to derive accurate physical properties.

The presence of offsets may also affect follow-up ALMA observations of *JWST* targets (or vice-versa). If there is a spatial offset, this should be considered when planning observations and interpreting data. For instance, *JWST*/NIRSpec has a slit width of only $\sim 0.2$ arcsec (Jakobsen et al., 2022), comparable to our median uncertainties, and much smaller than our median significant offsets (see Table 16.1). Large surveys with this instrument, e.g. Cosmic Evolution Early Release Science (CEERS Finkelstein et al., 2022), *JWST* Advanced Deep Extragalactic Survey (JADES Eisenstein et al., 2023), might only observe the UV emission, and miss the dusty component. Therefore, spatial offsets must be taken into account for all studies, not just spatially resolved galaxy modelling.

# Chapter 18

# Summary and Conclusions

We study a sample of main-sequence star-forming galaxies at $z \sim 4$–6 from the ALPINE dataset. We identify galaxies that were detected in [C II] and in FIR continuum emission in their ALMA data, UV emission in *HST* data, and optical emission in K-band UltraVISTA data, excluding galaxies that were mergers or multi-component systems based on Romano et al. (2021) and Jones et al. (2021).

We use the *HST* coordinates (with astrometric correction) from Faisst et al. (2020) as the UV centroids. To calculate [C II], FIR continuum, and optical centroids for the non-merging population of 54 galaxies, we fit 2D Gaussians to the detected emission and applied a bootstrapping technique to estimate fit centroids and uncertainties. We convolve the positional accuracy of the respective telescopes and ALMA noise correlation uncertainty with the fit uncertainty to calculate the total uncertainty. We then estimate the spatial offset between centroids of detected emission for each galaxy, along with offset significance ($s$), which is calculated as the measured offset divided by the total uncertainty on the offset.

- The (sigma-clipped) median of the measured offsets is 0.1–0.2 arcsec, which translates to ∼0.6–1.3 kpc at our median redshift of $z \sim 5$.
- We establish a cut-off of $s > 3$ to define *significant* offsets. These significant offsets are ∼0.3–0.7 arcsec, or ∼1–6 kpc.
- 14 galaxies (∼25 per cent of the sample) display significant offsets between one or more emission pairs, although none have all four emissions offset from each other. The remaining galaxies (∼75 per cent of the sample) have no significant offsets.
- We discuss several potential phenomena that may lead to the observation of spatial offsets, plotting corresponding galaxy physical properties against their measured spatial offsets wherever possible. We find no clear trends as the statistics are too low to make strong conclusions. The physical origin of the observed offsets is therefore still unclear.

The existence of significant spatial offsets in one out of every four galaxies in our sample indicates that it is possible for main-sequence galaxies at $z \sim 4$–6 to have the bulk of the stars spatially offset from the bulk of the interstellar medium. As this picture runs counter to the assumption of co-spatial emission in galaxy SED fitting codes, models must take into account that the emission observed across wavelengths may be coming from different, spatially segregated regions of the galaxy.

We require large number statistics and higher resolution observations and simulations to identify the processes driving spatial offsets. For instance, we could perform this analysis on the REBELS sample (already shown to have spatial offsets in Inami et al., 2022), which has different SFRs and M*, but similar angular resolution as ALPINE. *JWST*, with its superior angular resolution, may also be able to shed light on the origin of offsets (e.g. Bakx et al., 2023).

# Acknowledgements

The Cosmic Dawn Center is funded by the Danish National Research Foundation under grant number 140. This publication has received funding from the European Union's Horizon 2020 research and innovation programme under grant agreement No 101004719 (ORP). M.R. acknowledges support from the Narodowe Centrum Nauki (UMO-2020/38/E/ST9/00077). E.I. acknowledge funding by ANID FONDECYT Regular 1221846. GCJ acknowledges funding from the "FirstGalaxies" Advanced Grant from the European Research Council (ERC) under the European Union's Horizon 2020 research and innovation programme (Grant agreement No. 789056). M.B. acknowledges support from FONDECYT regular grant 1211000 and by the ANID BASAL project FB210003.

This paper is based on data obtained with the ALMA Observatory, under Large Program 2017.1.00428.L. ALMA is a partnership of ESO (representing its member states), NSF (USA) and NINS (Japan), together with NRC (Canada), MOST and ASIAA (Taiwan), and KASI (Republic of Korea), in cooperation with the Republic of Chile. The Joint ALMA Observatory is operated by ESO, AUI/NRAO and NAOJ. This paper makes use of archival data from the NASA/ESA *Hubble Space Telescope*. Based on data obtained with the European Southern Observatory Very Large Telescope, Paranal, Chile, under Large Program 185.A-0791, and made available by the VUDS team at the CESAM data centre, Laboratoire d'Astrophysique de Marseille, France. This work is based on observations taken by the 3D-*HST* Treasury Program (GO12177 and 12328) with the NASA/ESA *HST*, which is operated by the Association of Universities for Research in Astronomy, Inc., under NASA contract NAS5-26555. Based on data products from observations made with ESO Telescopes at the La Silla Paranal Observatory under ESO programme ID 179.A-2005 and on data products

produced by TERAPIX and the Cambridge Astronomy Survey Unit on behalf of the UltraVISTA consortium.

## Data Availability

The data used in the paper are available in the ALMA archive at https://almascience.nrao.edu. The derived data and models generated in this research will be shared on reasonable request to the corresponding author.

# Part IV

# Little Red Dots

This part of the thesis contains the following article:

## "Deciphering the UV–NIR spectrum of an early AGN host with *JWST*"

In preparation for submission to the journal of Astronomy and Astrophysics (A&A)

Authors: Meghana Killi, Darach Watson, Gabriel Brammer, Conor McPartland, Dan Coe, Katriona Gould, Natalie Allen

# Chapter 19

# Abstract

*Context:* Recently, *JWST* has revealed several curious objects, nicknamed "Little red dots", which are a class of extremely compact sources with rest-frame red optical/near-infrared (NIR) colours and blue ultraviolet (UV) colours. They are common at $z \sim 4-8$, and may represent an extremely numerous class of active galactic nuclei (AGN) with supermassive black holes of moderate mass.
*Aims:* We present the rest-frame UV–NIR spectrum and morphology of a prototypical example, MACS J0647−1045, at redshift $z = 4.5321^{+0.0001}_{-0.0001}$. The underlying continuum shows a clear break in the slope, changing from red in the optical/near-infrared (NIR) to blue in the optical-UV, consistent with two different components, possibly an AGN in the optical/NIR and the host galaxy in the UV. We aim to separate the emission from the AGN and the host, and study the properties of each.
*Methods:* We fit the *JWST*/NIRCam morphology with `GALFITM`, and the *JWST*/NIRSpec/PRISM spectrum with `lmfit`. We also estimate physical properties from nebular and broad line ratios.
*Results:* The morphology is unresolved ($r_e \lesssim 0.17\,\mathrm{kpc}$) in NIRCam long-wavelength filters, and extended ($r_e = 0.45 \pm 0.02\,\mathrm{kpc}$) in the short-wavelength filters. The red/blue appearance of the spectrum is not consistent with being due to a Balmer break from an older stellar population. Rather, the UV continuum likely arises from star-formation, whereas the red optical/NIR continuum appears to come from a highly obscured star-forming region with $\mathrm{A_V} = 5.73^{+0.11}_{-0.15}$. The H$\alpha$ and emission line requires the inclusion of both broad and narrow components. $\sim 38.1\%$ of the total observed H$\alpha$ flux arises from the broad component with a full width at half maximum (FWHM) of $4330^{+326}_{-274}\,\mathrm{km\,s^{-1}}$. The forbidden [O III] 5007Å line, which has a similar strength to H$\alpha$, is not broadened, demonstrating an AGN origin, rather than an outflow. We estimate the mass of the central black hole to be $1.2 \pm 0.2 \times 10^8\,\mathrm{M_\odot}$.
*Conclusions:* We conclude therefore that the observed spectrum and morphology are derived partly from the AGN and partly from a compact star-forming host galaxy.

# Chapter 20

# Introduction

*JWST* surveys have been found to contain abundant extragalactic red point, or near-point sources, sometimes referred to as "little red dots" (LRDs; Matthee et al., 2023)). These somewhat mysterious sources appear to be dominated by emission from active galactic nuclei (AGN) at $z \sim 4-9$. Estimates of their supermassive black hole (SMBH) masses based om their modestly broad (1200–4000 $\mathrm{km\,s^{-1}}$) H$\alpha$ (Kocevski et al., 2023; Matthee et al., 2023) and H$\beta$ emission lines (Larson et al., 2023; Kokorev et al., 2023), suggest low–moderate mass ($10^5$–$10^7$ $\mathrm{M_\odot}$). LRDs also exhibit an unusual "V-shaped" spectral energy distribution (SED), i.e. a spectrum with very red restframe optical colours and blue UV colours (e.g. Furtak et al., 2023a; Barro et al., 2023; Fujimoto et al., 2023a; Greene et al., 2023). The unusual SEDs suggest that LRDs might be something more exotic than a simple type 1 AGN.

Studies of high-$z$ AGN provide a window into the formation and growth of SMBH. SMBH with masses estimated to be in excess of a billion solar masses have now been found as early as 600 Myr after the Big Bang (e.g. Wang et al., 2021). This poses a serious challenge to black hole growth scenarios involving even the largest stellar mass black holes (Ohkubo et al., 2009; Chantavat et al., 2023) and even push the limits of the hypothesised direct-collapse black hole scenario (Bromm & Loeb, 2003b; Trinca et al., 2022; Natarajan et al., 2023; Schneider et al., 2023). Discovering a population of lower mass SMBH in the early universe such as LRDs that may be in a dust-obscured, rapid growth phase (e.g. Fujimoto et al., 2022b) is therefore important. The number of these LRD moderate-mass SMBHs far exceeds that expected from extrapolating UV luminosity functions, by up to a factor of 100 (Barro et al., 2023; Greene et al., 2023), suggesting that they are a significant population among early AGN.

While many LRDs do have a compact morphology, several show a spatially extended component as well (Harikane et al., 2023). Together with the unusual SED shape, this indicates that the contribution of the host galaxies to LRD spectra and morphology is non-negligible. LRDs therefore provide a unique opportunity to study not only the numbers and level

of activity of early AGN, but also the host galaxies and their relation to the central AGN. This simultaneous view into early, young, obscured AGN and their hosts can tell us about the larger environment that SMBH growth took place in, and how this in turn affected the host, including properties such as star formation rate, spatial extent, dust obscuration, and gas composition and ionisation.

A downside is that as contribution from the host increases and dominates over that from the AGN, it becomes increasingly difficult to identify the source as an AGN (Onoue et al., 2023). Several authors have pointed out that the broadness in Balmer emission lines is currently the only reliable method to detect these obscured, low-mass AGN (Kocevski et al., 2023; Matthee et al., 2023). This detectablity in turn has implications for the estimated number counts of AGN. It has thus become crucial to understand the nature of these objects, estimate the contribution of the AGN and host to their observed properties, and trace their evolution from the early Universe to the present.

In this paper, we study MACS J0647−1045, a prototypical example of an LRD at $z = 4.5321^{+0.0001}_{-0.0001}$, with a low-resolution (but high signal-to-noise ratio; SNR) NIRSpec prism spectrum. We consider the origin of the various spectral features in an AGN or star-forming host galaxy using the spectral shape, line ratios and widths, as well as the morphology in various NIRCam bands to guide our conclusions.

We assume a cosmology based on the Planck 2018 data (Aghanim et al., 2020). Stellar masses and star-formation rates are based on a Chabrier initial mass function (Chabrier, 2003). All magnitudes reported are in the AB system.

# Chapter 21

# Methods

## 21.1 Observations and Data

MACS J0647−1045 was observed in the MACS0647 (Ebeling et al., 2010) galaxy cluster lensing field as part of the *JWST* Cycle 1 General Observers (GO) program (ID: GO-1433; PI: Dan Coe), including *JWST*/NIRCam imaging and high SNR *JWST*/NIRSpec prism spectroscopy. The NIRCam images in filters F115W, F150W, F200W, F277W, F356W, F444W, and NIRSpec MSA spectra were obtained from the DAWN *JWST* Archive[1] (DJA) presented by Brammer et al. (in prep.). NIRSpec spectra were extracted from the telescope exposures using `MsaExp v.0.6.7` (Brammer, 2023), with standard wavelength, flat-field, and photometric calibrations. The reduction is described in detail in Heintz et al. (2023a). The 2D and 1D spectra (optimally extracted following Horne, 1986) are shown in Fig. 21.2. The NIRSpec PRISM resolution varies across the spectrum with a minimum of R$\sim$ 30 at 1.2µm, rising to a maximum of R$\sim$ 320 towards the NIR end (Jakobsen et al., 2022). These resolution values are for uniform illumination of the slit and are likely to be higher for a compact source. We return to this subject below. The photometry from the six NIRCam filters in a 0.5 arcsec aperture is overplotted on the 1D spectrum. As the photometry and spectrum match, slit losses appear to be minimal for this source, obviating the need for flux rescaling. Additionally, since MACS J0647−1045 is located at the outskirts of the lensing field, and its magnification is expected to be small, we do not apply a magnification correction.

## 21.2 Morphology

We model the galaxy's morphology in the six NIRCam filters using `GALFITM` (Bamford et al., 2011; Häußler et al., 2013; Vika et al., 2013), a modified version of `GALFIT` 3.02 (Peng et al., 2002, 2010) that can simultaneously fit multiple bands. Since `GALFITM` requires pixel matched images, we

[1] https://dawn-cph.github.io/dja/index.html

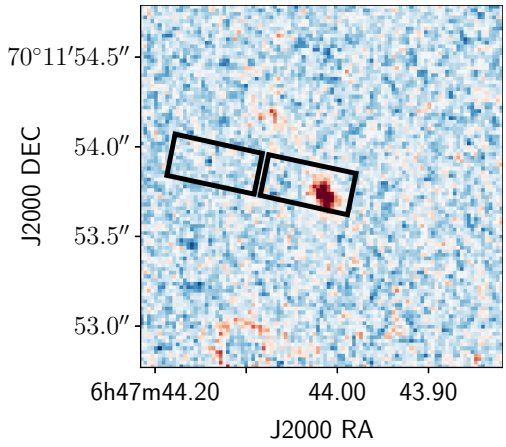


**Figure 21.1:** A cutout of the F115W NIRCam filter image in the MACS J0647 field, showing the position of MACS J0647−1045, along with the NIRSpec slits overlaid.

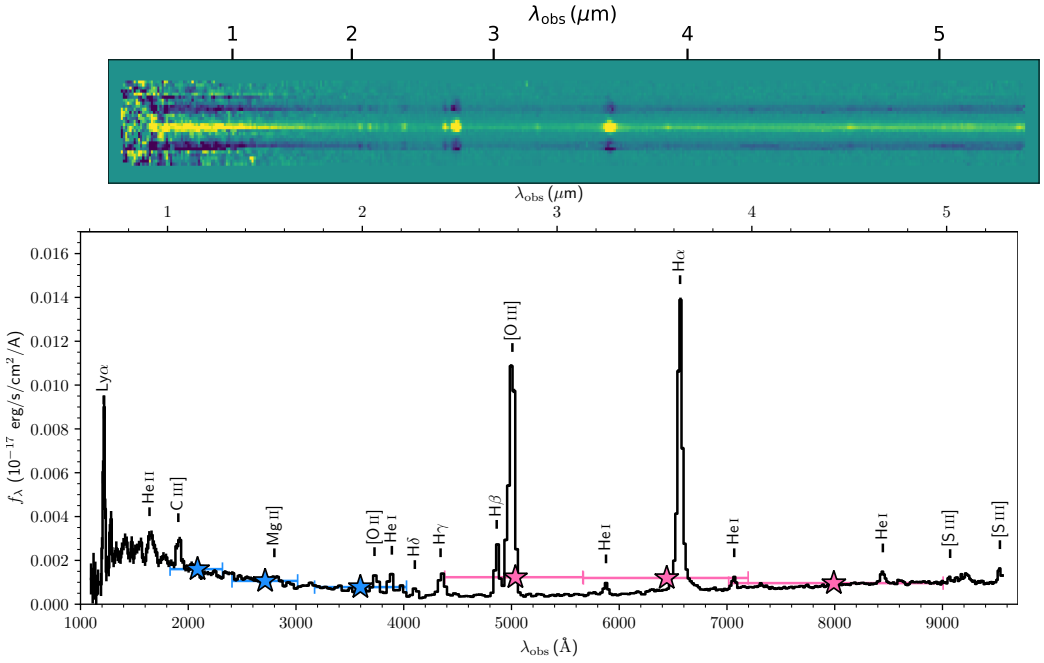


**Figure 21.2:** *Top:* 2D NIRSpec PRISM spectrum of MACS J0647−1045 showing the bright Hα, [O III], and Hβ emission. *Bottom:* 1D spectrum with some identified lines labelled. The observed wavelengths are shown in μm on the top axis, while the rest-frame wavelengths are plotted in Å on the bottom axis. The NIRCam photometry fluxes (along with measurement errors) in a 0.5 arcsec diameter aperture in the UV filters F115W, F150W, and F200W are shown as blue stars with the NIRCam bands shown as errorbars. Optical/NIR filters F277W, F356W, and F444W are similarly shown as pink stars with errorbars.

model the 20 mas short wavelength UV bands (F115W, F150W, F200W) separately from the 40 mas long wavelength optical/NIR bands (F277W, F356W, F444W). Each set of images are fit with three models: a point source, a Sérsic profile, and a Sérsic profile with a central point source. Point spread function (PSF) models for each band are generated with `WebbPSF`(Perrin et al., 2012, 2014). Sigma images were derived from the weight maps provided by DJA. Object masks for background sources are created by dilating the DJA segmentation map by three pixels. Initial model parameters and sky background estimates are drawn from the DJA photometric catalogue for the MACS J0647 field.

## 21.3 Spectroscopy

Our spectroscopic model should account for the following features observed in LRDs: broad components in Hα and possibly Hβ, narrow line emission, a blue continuum on the UV side, and a red continuum on the optical/NIR side.

We treat the UV and optical/NIR continuum as having different origins, modelled by two independent continuum components with different dust extinctions. We simultaneously fit narrow Gaussians for all lines, along with broad Gaussian components for Hα and Hβ (see Sec. 21.3.1). In order to have control over the redshifts and velocity widths of individual components of each line, the properties of the two continuum components, and account for the instrumental resolution, we use a fitting algorithm based on `lmfit` (Newville et al., 2014).

We correct the 1D spectrum for galactic extinction using the `PlanckGNILC` map from the `dustmaps` library (Green, 2018). To fit the continuum, we use two power laws with distinct power law slopes extinguished by the Small Magellanic Cloud (SMC) dust extinction law (Gordon et al., 2003). We choose SMC extinction because with a power law model, we find that the observed continuum requires a steeper slope than the Calzetti curve provides (Calzetti et al., 2000)). However, a steepened Calzetti attenuation curve provides an equally good fit (Salim et al., 2018). The power law is of the form $f(\lambda) \propto \lambda^{-\beta}$, with $\beta$ constrained to be above -3 (and below 0) (Bouwens et al., 2016, 2023). Even with a fixed slope dust extinction law such as the SMC, there is a strong degeneracy between the intrinsic power-law slope and the dust reddening.

To fit emission lines, we identify the list of typical strong lines in star-forming galaxies in the wavelength region of our spectrum ($\sim$ 1000–9700 Å; restframe). Each of these lines we model with a single Gaussian, with freely variable normalisation. For close doublet lines, we tie the Gaussian heights based on intrinsic line ratios. For instance, we set the [O III] 5007 to 4959 Å ratio to be 2.98 (Storey & Zeippen, 2000).

The expected line centre is obtained by multiplying the restframe wavelength ($\lambda_{\rm rest}$) by ($1+z_{\texttt{msa}}$), where $z_{\texttt{msa}}$ is the redshift estimate obtained from a preliminary `MsaExp v. 0.6.7` (Brammer, 2023) fitting. We then allow the central wavelengths (and thereby the redshift) to vary between $\pm0.01\mu$m of

$\lambda_{\rm rest}\,(1+z_{\texttt{msa}})$. All the narrow line redshifts are tied together. We model all narrow lines by constraining the Gaussian width to be above $100\,{\rm km\,s^{-1}}$, while the broad Gaussian widths are constrained to be above $1000\,{\rm km\,s^{-1}}$ (an arbitrary large value of

$10\,000\,{\rm km\,s^{-1}}$ is set as the maximum for both). To obtain the Gaussian width of resolution-broadened lines, we convolve the input velocity widths with the *JWST* prism resolution from Jakobsen et al. (2022). We scale the resolution by a constant factor of 1.3 to account for the improved resolution for compact sources in the NIRSpec slit (see de Graaff et al. 2023; Greene et al. 2023).

We estimate fit uncertainties by running an MCMC chain using the `emcee` fitting module in `lmfit`, with the initial values set to the minimised result from our `lmfit` fit above. Given the large number of free parameters, we use 100 walkers, 10 000 steps, and a burn rate of 100 to ensure that the chain is long enough to sample a sufficient portion of the parameter space.

### 21.3.1 Analysis of line widths

We conduct an analysis of emission line widths by fitting Gaussians of varying widths to individual lines. Given the low and uncertain resolution, we are unable to distinguish line widths below $\sim 1000\,{\rm km\,s^{-1}}$. Even in the highest resolution region of our spectrum towards the NIR end, we are limited to widths above $\sim 700\,{\rm km\,s^{-1}}$. Indeed, it has been seen that the width of emission lines from point-like sources in the low resolution NIRSpec spectrum can vary by $\sim 1$ wavelength bin (Christensen et al., 2023). Hence, we cannot realistically distinguish between lines produced by star-formation ($\lesssim 350\,{\rm km\,s^{-1}}$) and AGN narrow line region (NLR) emission ($\lesssim 1000\,{\rm km\,s^{-1}}$). Nonetheless, we can measure broadness $\gtrsim 1000\,{\rm km\,s^{-1}}$, such as from an AGN BLR. We find that H$\alpha$ shows a clear signature of broad emission (see Appendix B.1). We try fitting a broad component to the H$\beta$ line as well, however we find no evidence for a broad H$\beta$ component and therefore do not include broad components for the other Balmer lines in the final fit.

# Chapter 22

# Results

## 22.1 Morphology

We show our best-fit GALFIT model and residual in Fig. 22.1. The source appears to consist of a central component with extended irregular matter around it in all bands. The best fit is obtained with a Sérsic profile and a central point source, indicating the presence of a central compact core within an extended structure, an AGN within a host galaxy, for instance. We calculate the Bayesian information criterion (BIC) for these fits, and find $\Delta$BIC to be 86 between the Sersic and Sersic+PSF and 2 290 between PSF and Sersic+PSF fit for the UV bands. Similarly, we find $\Delta\mathrm{BIC} \sim 1\,568$ between the Sersic and Sersic+PSF and 8 992 between PSF and Sersic+PSF for the optical/NIR bands. The improvement in the fit is therefore more pronounced in the UV images than the optical/NIR. While this may be due to a smaller PSF in the former, it may also be an intrinsic feature of the morphology where the central AGN dominates towards the NIR, while the host galaxy contributes more to the continuum in the UV.

## 22.2 Spectrum

The best fit to the spectrum is shown in Fig. 22.2. This fit was obtained by fitting two SMC-extinguished power laws for the continuum, one for the UV, and one for the optical/NIR side of the spectrum. All lines are modelled with narrow Gaussian profiles with an additional broad Gaussian component added to the H$\alpha$ line. We find that there is no appreciable velocity offset between the broad and narrow H$\alpha$ lines when the H$\alpha$ complex is fit separately, so we also tie these together for the full fit. In addition, we find that the fit is not able to obtain a constraint on the [N II] doublet (6549 and 6585 Å) flux in the H$\alpha$ complex (see Appendix Fig. B.1). We therefore do not include the [N II] doublet in the fit.

We find that a significant fraction of the residuals in our best-fit model are a result of the uncertainty on the dispersion function for the spectrograph. Hence, we fit several line complexes individually to obtain accurate

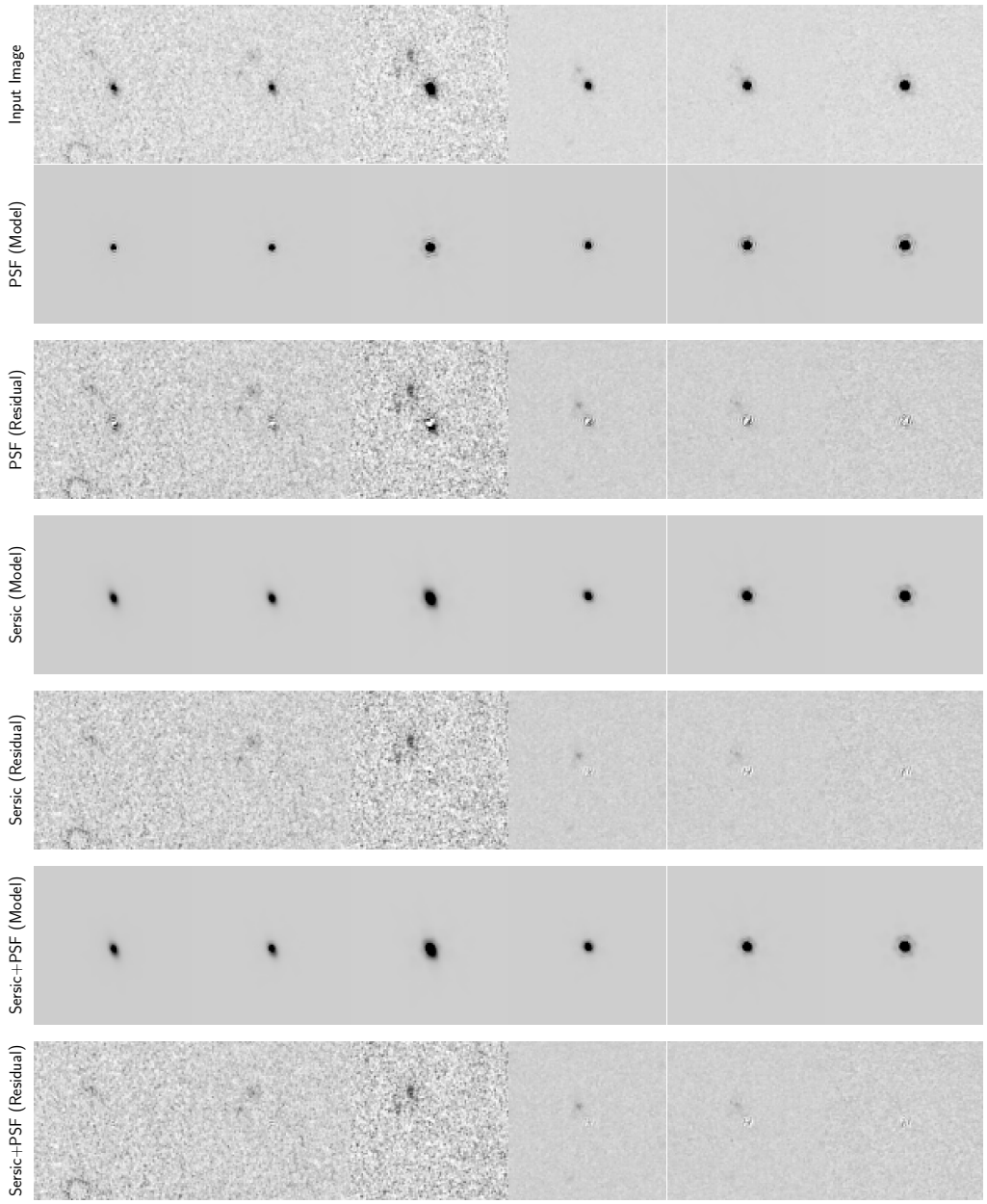


**Figure 22.1:** GALFIT models and residuals in the six NIRCam bands using PSF, Sersic, and combined Sersic+PSF models. The PSF fit shows clear residuals, especially in the UV bands. The fit improves considerably with the addition of a Sersic component. The best fit is obtained when both Sersic and PSF components are used, with $\Delta$BIC indicating a significant improvement in all bands (Sec. 22.1).

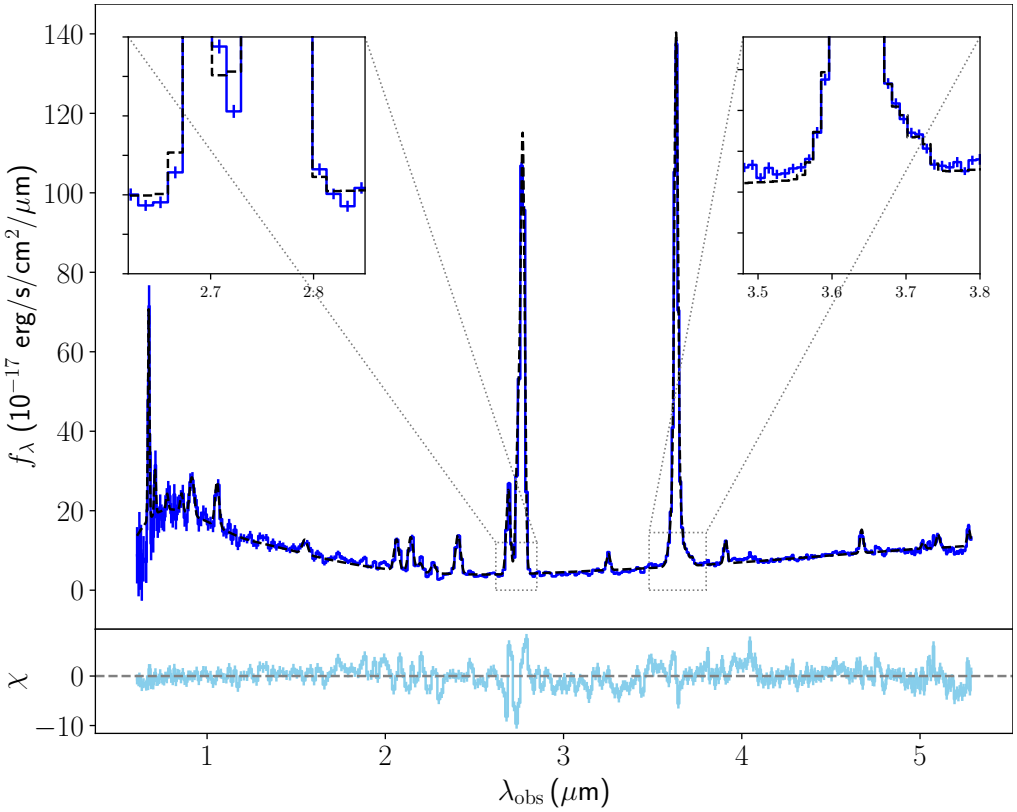


**Figure 22.2:** The best-fit model (black dashed curve) to the data (blue step curve), along with zoom-in cutouts of [O III] and Hα regions. The residuals are shown in the bottom panel.

line fluxes, and avoid being influenced by variations in the continuum and instrument dispersion. We show these fits in Fig. 22.3. The best-fit results from all the above are summarised in Table 22.1.

## 22.3 Physical properties

Using our best-fit model, we estimate the luminosity of narrow and broad emission lines. We also estimate the continuum luminosity at restframe 1500 Å ($L_{1500}$) and 5100 Å ($L_{5100}$). These values are all reported in Table 22.1. We estimate the Balmer decrement from the narrow Hα/Hβ ratio following the prescription in Momcheva et al. (2013), finding $A_V$ of 1.1±0.2, and use this to report extinction-corrected narrow line luminosities. We correct the $L_{1500,\rm UV}$ luminosity by an $A_V$ of 0.54±0.01 from the SMC extinction on the best-fit on the UV power law.We also report extinction-corrected Hα broad line and $L_{5100,\rm NIR}$ luminosities, corrected by the extinction derived from the optical/NIR fit ($A_{V,\rm NIR} = 5.7 \pm 0.2$). The Balmer decrement of the broad Hα/Hβ (using the upper limit on broad Hβ) gives an $A_V > 4.1$, which is consistent with the optical/NIR continuum fit. In other words, the optical/NIR extinction is sufficient to suppress a broad Hβ component (see Sec. 23.1).

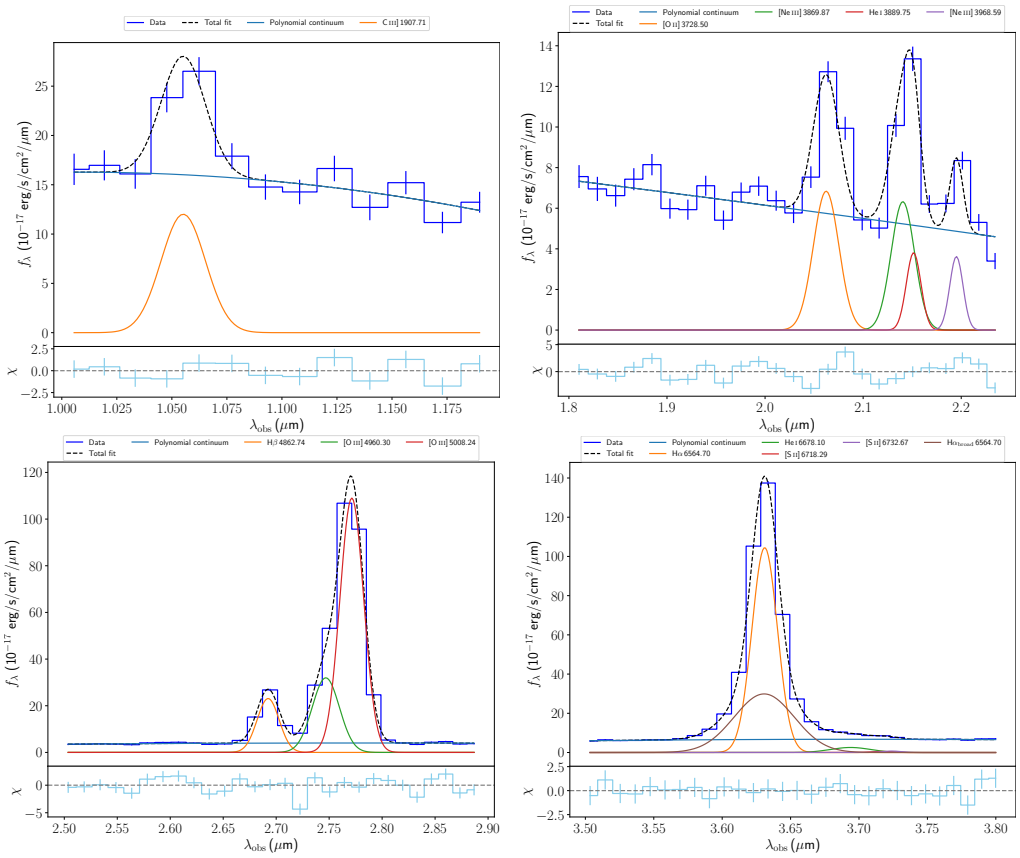


**Figure 22.3:** Best-fits to line complexes across the spectrum. The individual lines are indicated with coloured curves. The data, best-fit, and residual curves follow the same colour scheme as Fig. 22.2.

| **Continuum** | | |
|---|---|---|
| $A_{V,UV}$ | $0.54^{+0.01}_{-0.01}$ | |
| $\beta_{UV}$ | $-2.99^{+0.01}_{-0.00}$ | |
| $A_{V,NIR}$ | $5.73^{+0.11}_{-0.15}$ | |
| $\beta_{NIR}$ | $-2.90^{+0.15}_{-0.07}$ | |
| Wavelength (Å),fit | Flux ($10^{-17}$ erg s$^{-1}$ cm$^{-2}$ Å$^{-1}$) | Luminosity ($10^{26}$ erg s$^{-1}$) |
| 1500,UV | $18.15^{+0.17}_{-0.16}$ | $41.48^{+0.89}_{-0.87}$ |
| 1500,NIR | 0 | $4.42^{+0.80}_{-1.23} \times 10^{3}$ |
| 1500,total | $18.15^{+0.17}_{-0.16}$ | $4.46^{+0.80}_{-1.23} \times 10^{3}$ |
| 5100,UV | $2.85^{+0.05}_{-0.05}$ | $1.07^{+0.02}_{-0.02}$ |
| 5100,NIR | $1.63^{+0.07}_{-0.07}$ | $126.48^{+11.02}_{-17.40}$ |
| 5100,total | $4.48^{+0.07}_{-0.07}$ | $127.54^{+11.02}_{-17.40}$ |
| **Line** | | |
| Line wavelength (Å) | Flux ($10^{-17}$ erg s$^{-1}$ cm$^{-2}$ Å$^{-1}$) | Luminosity ($10^{26}$ erg s$^{-1}$) |
| Ly$\alpha$ 1215.40 | $0.81^{+0.01}_{-0.01}$ | $123.49^{+248.72}_{-82.49}$ |
| C IV 1549.48 | $0.17^{+0.02}_{-0.02}$ | $3.45^{+3.97}_{-1.85}$ |
| C III] 1907.71 | $0.31^{+0.04}_{-0.04}$ | $2.37^{+1.99}_{-1.09}$ |
| Mg II] 2799.12 | $0.10^{+0.04}_{-0.04}$ | $0.19^{+0.13}_{-0.09}$ |
| [O II] 3728.50 | $0.25^{+0.04}_{-0.04}$ | $0.27^{+0.11}_{-0.08}$ |
| [Ne III] 3869.87 | $0.26^{+0.05}_{-0.05}$ | $0.28^{+0.11}_{-0.08}$ |
| [Ne III] 3968.59 | $0.09^{+0.02}_{-0.02}$ | $0.09^{+0.03}_{-0.02}$ |
| H$\delta$ 4102.94 | $0.06^{+0.03}_{-0.03}$ | $0.05^{+0.04}_{-0.03}$ |
| H$\gamma$ 4341.73 | $0.20^{+0.05}_{-0.05}$ | $0.17^{+0.07}_{-0.05}$ |
| [O III] 4364.44 | $0.21^{+0.05}_{-0.06}$ | $0.17^{+0.07}_{-0.06}$ |
| H$\beta$ 4862.74 | $0.60^{+0.04}_{-0.04}$ | $0.42^{+0.07}_{-0.06}$ |
| [O III] 4960.30 | $1.03^{+0.01}_{-0.01}$ | $0.70^{+0.15}_{-0.12}$ |
| [O III] 5008.24 | $3.06^{+0.04}_{-0.04}$ | $2.06^{+0.43}_{-0.35}$ |
| H$\alpha$ 6564.70 | $2.56^{+0.08}_{-0.08}$ | $1.21^{+0.19}_{-0.17}$ |
| [S II] 6718.29 | $0.02^{+0.00}_{-0.00}$ | $9.58^{+1.87}_{-1.62} \times 10^{-3}$ |
| [S II] 6732.67 | $0.04^{+0.01}_{-0.01}$ | $0.02^{+0.01}_{-0.01}$ |
| He I 7067.10 | $0.17^{+0.02}_{-0.02}$ | $0.07^{+0.01}_{-0.01}$ |
| He I 8446.70 | $0.16^{+0.02}_{-0.02}$ | $0.06^{+0.01}_{-0.01}$ |
| H$\alpha_{broad}$ 6564.70 | $1.58^{+0.06}_{-0.06}$ | $0.75^{+0.10}_{-0.09}$ |

**Table 22.1:** All narrow line properties have been corrected for dust extinction of $A_V = 1.1 \pm 0.2$ from the Balmer decrement, and broad line and continuum properties are corrected using the corresponding $A_V$ from the fit.

We obtain broad velocity width of $4330^{+326}_{-274}\,\mathrm{km\,s^{-1}}$ for the Hα line. From the broad Hα luminosity and FWHM, we estimate the SMBH mass to be $1.2 \pm 0.2 \times 10^8\,\mathrm{M_\odot}$ (Greene & Ho, 2005; Kocevski et al., 2023). If we assume that the continuum emission at 5100 Å restframe is dominated by the AGN, we can also derive the mass from $L_{5100}$, total continuum luminosity at 5100 Å (Kaspi et al., 2000; Kocevski et al., 2023). This results in an SMBH mass of $5.2^{+0.9}_{-0.8} \times 10^8\,\mathrm{M_\odot}$. These values agree within the uncertainty range for single-epoch measurements of SMBH mass (Denney et al., 2009; Park et al., 2012; Campitiello et al., 2020), but also allow for some of the $L_{5100}$ to be contributed by the host galaxy.

The differences in inferred SFRs may be an indication that the narrow lines are not all contributed to by star-formation. We discuss this further below in Sec. 23.1.

We calculate gas-phase metallicity (Z) following the R23, O32, and O2 formulations in Sanders et al. (2023), and find 12+log(O/H)$\sim$ 7.8. Finally, we estimate the gas temperature using the ratio of the [O III] 4363 Å to the [O III] 4959+5007 Å doublet luminosity (Nicholls et al., 2020). We obtain a value of $5 \pm 2 \times 10^4$ K, which is the typical temperature of ionised regions in AGN environments (e.g. Larson et al., 2023).

# Chapter 23

# Discussion

The origin of the emission in LRDs is perhaps the biggest open question currently. Based mostly on Hα lines with widths of about 1200–4000 km/s, and on the very compact nature of these sources, AGN activity has been inferred. Here we discuss the origin of the UV/blue and red/NIR continua, as well as the narrow and broad emission lines in MACS J0647−1045, and consider several models that could reasonably fit the observed spectrum.

## 23.1 Alternate Models

First, we check whether the broadness in the emission lines could be from star-formation-related activity rather than and AGN. One possibility for line broadening is a merging system with multiple components at different redshifts (e.g. Maiolino et al., 2023a). To test this, we fit two sets of Gaussian lines each with common velocity widths $<1000\,\mathrm{km\,s^{-1}}$ around the Hα line region. The two sets have different redshifts, and the line centres in each are together allowed to vary within ±0.01μm of their respective redshifts. The resulting model fails to fit the broad Hα feature (see Appendix Fig. B.1).

In some cases with star-formation in environments where the column density of atomic hydrogen is high, Raman scattering may broaden the Balmer lines to many thousands of km/s without strong Doppler broadening (e.g. Dopita et al., 2016). Such wings can be very broad in environments with very high column densities, but are likely to be relatively weak and have Lorentzian shapes (Kokubo et al., 2023). Given the damped Lyman$\alpha$ absorbers with very high column densities observed in other high-redshift galaxies (Heintz et al., 2023a) and the compactness of LRDs, such extreme [H I] columns might be present. We therefore tested an instrumentally-broadened Lorentzian profile to the Hα line, but this did not fit the data well.

The Hα line is best-fit with an unresolved narrow component and a broad component nearly 5000km/s – a width much higher than expected from stellar activity, including extreme supernova-driven outflows (Fabian,

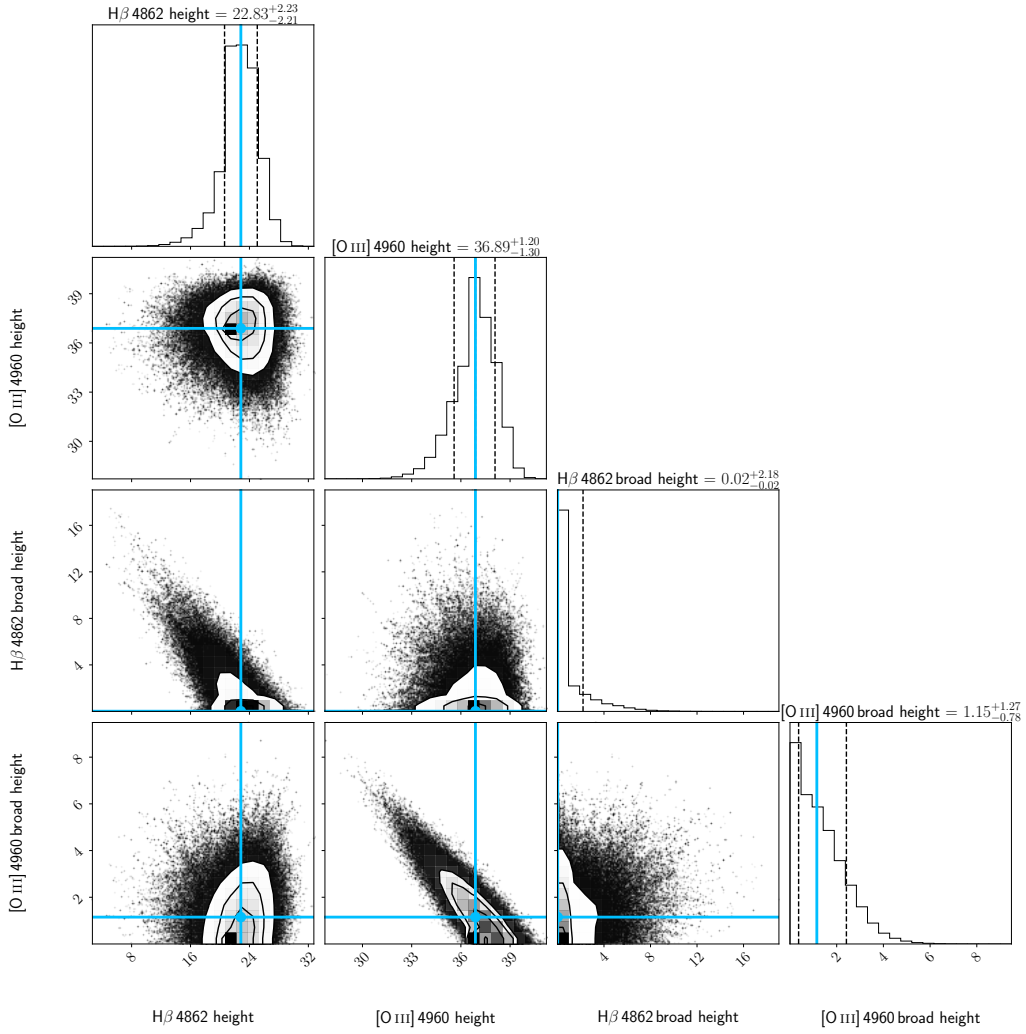


**Figure 23.1:** Corner plot showing the MCMC results for broad component fits to Hβ and [O III] doublet (4959 and 5007 Å) lines. Broad component height is arbitrarily small for both [O III] and Hβ.

2012; Baldassare et al., 2016; Davies et al., 2019). We also find no significant offset between the narrow and broad Hα components, which would be expected for an outflow. Moreover, we do not find any evidence of broadness in the [O III] doublet at the same width and strength (relative to the narrow component) as the broad Hα component. We show the results of our MCMC analysis in Fig. 23.1, by which we exclude the possibility of a broad [O III] line. We therefore conclude that the most likely origin for the broad Hα line is AGN activity.

Curiously, we fail to find any significant broad component in Hβ (Fig. 23.1). This is not due to the relatively lower SNR of the Hβ line compared to Hα. The Hα/Hβ ratio using the broad Hβ upper limit from the MCMC fit is $\gtrsim 13$. This ratio translates to an $A_V$ of $\gtrsim 4.1$ for an SMC extinction curve. We find an $A_V$ of $5.7\pm0.2$ for the optical/NIR continuum from our best-fit model, suggesting that there exists at least a model whereby the broad lines and red/NIR continuum is extinguished by a similar dust column. In contrast, the narrow Hα/Hβ ratio is only $\sim 4$, which gives an $A_V$ of $1\pm0.3$. From our best-fit model, we find an $A_V$ of $0.54\pm0.01$ for the UV continuum using the same curve and a fixed power-law slope. A slightly bluer slope would result in greater extinction. In other words, the UV continuum and narrow emission lines have similar modest dust obscuration, much lower than the red/NIR continuum and broad emission lines. We conclude that there seem to be two distinct origins for the narrow and broad emission lines, consistent with the blue/UV and red/NIR continua respectively.

Motivated by the compact-dominated nature of the morphology in the long wavelength bands, we consider whether the optical/NIR continuum could be modelled as direct thermal dust emission from the inner edge an AGN torus, i.e. a blackbody curve instead of a power law. We also add variable SMC extinction, just as we did for our best-fit power-law model. The model fits the optical/NIR continuum data well. We determine a dust temperature of $T_b \sim 2500\,\mathrm{K}$ with no significant extinction required or allowed on the optical/NIR side (see Appendix Fig. B.2). This temperature is significantly hotter than type 1 AGN dust tori, which are typically closer to 1400 K (Kishimoto et al., 2007; Hönig & Kishimoto, 2010). And it is even hotter than models of carbon grain thermal sublimation temperatures, which are around 2000 K (Kobayashi et al., 2009). Although we would expect there to be significant dust-obscuration by the outer dust of the blackbody emission from the inner BLR region, the dust-obscuration obtained from our SMC-extinguished blackbody fit is very low. This may be possible at certain viewing angles of the AGN, where the blackbody emission from the inner dust torus is directly transmitted to the observer without being screened by the outer dusty regions. However, if this were the case, we would not expect to see obscuration of the broad lines, and certainly not an obscuration factor of 13 between broad Hα and Hβ. For

this reason, while the continuum fit is good, the high temperature and inconsistency of the dust extinction with the broad Balmer lines, means that we do not favour the possibility that the optical/NIR continuum arises from thermal emission from an AGN dust torus.

The extreme blueness of the dust-corrected UV slope seems hard to explain, whether for an AGN (Hjorth et al., 2013) or for a young star-forming population (Bouwens et al., 2016), with $\beta$ slopes approaching $-3$ favoured by the fit ($F_\lambda \propto \lambda^\beta$). However, fixing the power-law slope to $-2.7$ does yield an acceptable fit. Another curious aspect of the continuum, which we do not test this in this paper, is the rollover on the UV side of the spectrum around the Ly$\alpha$ emission line, which we could not be replicate using dust attenuation, but may indicate Ly$\alpha$ damping in addition to dust attenuation (Heintz et al., 2023a), though the presence of the Ly$\alpha$ line in emission could be difficult to explain in that case.

The apparently 'V'-shaped SEDs of LRDs, with breaks in the rest-frame optical, have been suggested to be due to an AGN observed in dust-obscured direct emission and low-extinction scattered emission (Labbe et al., 2023), or obscured star-formation with the blue component due to direct AGN emission (Kocevski et al., 2023). Another possibility considered by the UNCOVER team is a partial cover, with a small fraction of low-extinction emission (A. Goulding, priv. comm.). A Balmer break was also proposed (Labbe et al., 2023) but seems unlikely to produce the observed features in our case.

## 23.2 Diagnostic diagrams

The BPT diagram (Baldwin et al., 1981; Kewley et al., 2013) is a common diagnostic used to separate AGN and star-forming sources. As our best-fit model is unable to recover the [N II] flux (Sec. 22.2), we can only obtain an upper limit on the [N II]/H$\alpha$ ratio. The BPT diagram (Fig. 23.2) suggests an extreme star-formation origin for the narrow lines in MACS J0647−1045. However, this may not be definitive since several studies find that the BPT diagram mis-classifies LRDs due to their low metallicity (e.g. Harikane et al., 2023). The OHNO diagram has been proposed as an alternative (Kocevski et al., 2023). We plot both in Fig. 23.2 and compare with $z \sim 0$ galaxies from the Sloan Digital Sky Survey (SDSS). The OHNO diagram also suggests a hard radiation field for the narrow lines in MACS J0647−1045, but on the AGN side of the boundary for $z = 0$ galaxies. This hints at our broader conclusion, which is that the narrow line emission in MACS J0647−1045 may be a combination of the star-formation in the galaxy and light from the AGN narrow-line region. Indeed, the SFR inferred from the narrow component of H$\alpha$ alone is an order of magnitude greater than the SFR inferred from the $L_{1500}$. While this could be due to the different timescales of these SF indicators, the fact

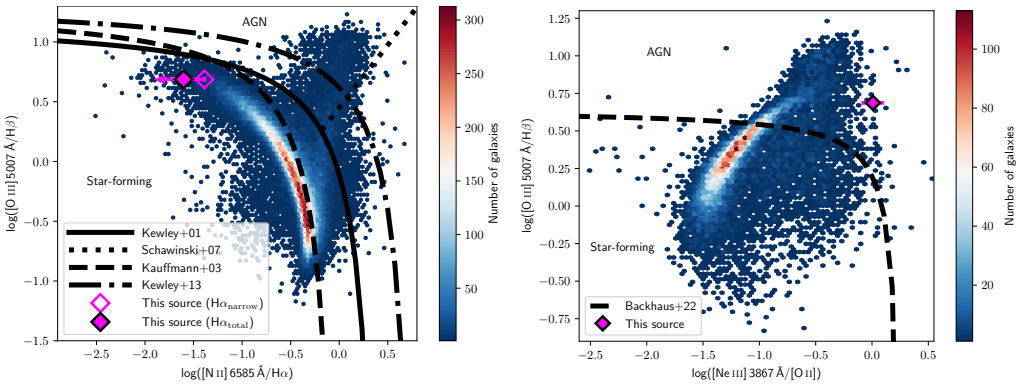


**Figure 23.2:** *Left:* BPT diagram of log([N II]/Hα) flux vs log([O III]/Hβ) flux of SDSS galaxies. [N II] flux is an upper limit of the 6585 Å line, [O III] flux is the sum of the (4959, 5007 Å) doublet, and [He I] flux is for the 5876 Å line. The position of this source is shown as a magenta diamond with errorbars (based on the AGN fit). The Hα flux for this object is the sum of narrow and broad component fluxes. The cutoff curves for AGN and galaxies from Kewley et al. (2001); Schawinski et al. (2007); Kauffmann et al. (2003), and the redshift-dependent curve from Kewley et al. (2013) are shown as black solid, dotted, dashed, and dash-dot lines respectively. *Right:* OHNO diagram of log([Ne III]/[O II]) vs log([O III]/Hβ) flux of SDSS galaxies. The curve separating AGN and star-formation from Backhaus et al. (2022) is plotted as a black dashed line. [O II] luminosity shown is the sum of the (3726, 3729 Å) doublet, modelled as a single Gaussian in our fit.

that the metallicity-corrected [O II] SFR is also much lower than the Hα SFR, hints that AGN activity may contribute to the narrow line fluxes. Furthermore, while we cannot definitively argue that the narrow lines are broader than 300 km s$^{-1}$ due to the uncertain instrumental dispersion, our best fits lie above about 600 km s$^{-1}$. Finally, the electron temperature we infer from the [O III] lines, as discussed in Sec. 22, is very high and may more likely be explained with a combination of a moderately high temperature and very high density, again, hinting at an AGN contribution to these lines.

MACS J0647−1045 simultaneously exhibits features of both AGN and star-formation, i.e. the broad Hα line and the spatially extended emission, possibly indicating the current stage of evolution of a young AGN that will eventually grow and dominate over the galaxy flux (Fujimoto et al., 2022b; Matthee et al., 2023). LRDs at $z \sim 4$–8 may evolve into the AGN-dominated, bright blue quasars we see at lower redshifts, which requires a black hole mass increase of nearly two orders of magnitude. This would entail near-Eddington or super-Eddington accretion rates or mergers over the next few billion years. It may, on the contrary, be possible that LRDs evolve into completely obscured AGN hosts or quiescent galaxies.

LRDs could be a unique class of objects such as obscured AGN with unusual scattering, or star-forming galaxies with a specific and separate population of dust-free young stars. Regardless, LRDs will require their

own template in SED fitting so that we may group similar objects under a new, more appropriate classification.

# Chapter 24

# Summary and Conclusion

We present the *JWST* NIRCam images and NIRSpec spectrum of MACS J0647−1045, a gravitationally lensed compact source with an unusual "V-shaped" continuum. We fit both the morphology and spectrum using various models, describing outflows, mergers, dust-obscured star-formation, AGN activity, and AGN dust torus emission. We find that the best-fit to the spectrum is obtained by assuming two distinct components for the UV and optical/NIR sides of the spectrum, with different power law slopes and dust extinctions. We also find that while nearly all emission lines fit well with a Gaussian of width 940±67, the H$\alpha$ line shows evidence of AGN-broadening with a velocity width of $4330^{+326}_{-274}\,\mathrm{km\,s^{-1}}$. Our modelling favours a scenario where the UV continuum arises from a star-forming region with low obscuration, narrow emission lines may arise either from star-formation or AGN NLR, and the optical/NIR continuum and broad line emission arise from the AGN and the surrounding BLR. The morphology, extended in the UV, and more compact towards the NIR, supports the domination of extended star-formation in the UV and compact AGN emission towards the NIR. We therefore conclude that the system is a highly obscured AGN within a less obscured star-forming host galaxy.

There are several potential future opportunities to expand the research on LRDs. One possibility is to conduct large *JWST* surveys targeting this population, which can help set constraints on the AGN number counts in the early Universe. Preliminary efforts in this direction have already proven promising (e.g. Greene et al., 2023; Maiolino et al., 2023a; Harikane et al., 2023). In addition, deeper data can reveal if there are broad components in other emission lines besides the Balmer lines, or at least set limits on the strength of the AGN and the extent of dust extinction. High resolution spectroscopy will identify whether emission lines are from AGN or stellar activity, and will also resolve doublets for better estimates of line luminosities, and in turn physical properties (e.g. Kocevski et al., 2023). IFS data as in Parlanti et al. (2023) would help map the relative spatial extent of broad H$\alpha$ and narrow [O III]. Further, as time variable measurements provide much more accurate SMBH properties than single-epoch deriva-

tions, observing LRDs at periodic intervals to study their variation over time would provide better constraints on SMBH masses for early black hole growth models.

## Acknowledgements

The data products presented herein were retrieved from the Dawn *JWST* Archive (DJA), an initiative of the Cosmic Dawn Center. The Cosmic Dawn Center is funded by the Danish National Research Foundation under grant number 140. DW is supported in part by Independent Research Fund Denmark grant DFF-7014-00017.

# Part V

# Future perspectives and conclusion

# Chapter 25

# Further work

Since its launch in 1990, *HST* has revolutionised the field of astronomy. ALMA has done the same for FIR astronomy over the last decade. Now, *JWST* is beginning to challenge our ideas yet again. With ambitious future projects such as the Extremely Large Telescope (ELT), we are well on our way to ushering in a new era of incredible discovery. Here, I offer some potential directions of future research that build on the work that I have described in Parts II–IV.

## 25.1 Large survey of high-$z$ FIR metallicities and DTMs

The next step forward in the study of metal enrichment of early galaxies is an ALMA large program targeting the [C II], [O III], and [N II] emission lines of $z > 6$ galaxies. In fact, the current highest redshift with such statistical studies is only $z \sim 3$ (e.g. Curti et al., 2020), and these metallicity measurements come from UV/optical emission, which may be heavily affected by dust obscuration. FIR metallicity estimates from ALMA are necessary to probe dust-obscured regions that UV/optical telescopes such as *JWST* fail to see through. As ALMA can measure the dust content simultaneously via the FIR continuum, the DTG and DTM can also be estimated to understand the evolution of dust, and efficiency of its production and destruction across cosmic time.

In addition, given the significant scatter in the FMR and MZR relations, a large survey of ALMA metallicities for $z > 3$ galaxies would place better constraints on the metal enrichment in the early Universe rather than a single galaxy such as A1689-zD1. Recent results hint that the nitrogen overabundance, on which our metallicity measurement depends, may in fact be a feature of early galaxies (Bunker et al., 2023b). Large surveys of high-$z$ elemental abundances and metallicities are therefore crucial to map the evolution of metallicity with redshift, and establish a timeline of metal enrichment in the Universe.

Further, comparing ALMA metallicities with those from *JWST* (e.g.

Sanders et al., 2023) for galaxies at similar redshifts would reveal the effect of dust attenuation on UV/optical metallicity estimates, and aid in calibrating our models accordingly.

## 25.2 Resolved studies of high-$z$ ISM

Since there seems to be a significant fraction of galaxies in the Cosmic Morning (and at high-$z$ in general) with stars and ISM spatially offset, there might be some physics occurring in early star-forming galaxies that we do not yet understand. One possible (albeit observationally expensive) way to shed light on this matter is to obtain high resolution ALMA imaging of galaxies that we have shown to display significant offsets. As an alternative, we may conduct resolved studies of gravitationally-lensed (and therefore, magnified) systems. Several works have achieved this either with galaxies at $z < 4$ (e.g. González-López et al., 2017), or with individual galaxies at $z > 4$ (e.g. Fujimoto et al., 2021; Wong et al., 2022), but resolved studies of large statistical samples at high-$z$ are yet to come.

Some recent ALMA programs such as CRISTAL (Cycle 8 Large Program; PI: Herrera-Camus) have succeeded in observing a select few ALPINE galaxies at high spatial resolution. Although their sample was not selected for offset significance, studying this data may reveal the inner workings of galaxies in the Cosmic Morning. Mapping out the relative morphology in UV, optical, and FIR (including dust and enriched gas) at kpc or even sub-kpc resolutions would give us an idea of the exact distribution of dust, gas, and stars, and how they interact with and affect each other. For the more luminous sources, we may expand the study of spatial morphology and offsets to atomic and molecular gas using emission from [C I], CO, [C I] (Valentino et al., 2020; Lee et al., 2021, e.g.). This would provide a detailed layout of the gas, star-formation, and metal composition in early galaxies.

## 25.3 LRDs from *HST*

In Part IV, I discussed the curious case of a compact AGN/galaxy composite, and the more general class of LRDs, observed with *JWST*. *JWST* is in fact, not the first to discover enigmatic compact sources; there exists a population of bright, compact objects in archival *HST* data with potentially similar properties to the *JWST* LRDs. I studied a sample of 17 of these *HST* objects at $z \sim 3.5$–$6.5$ in my Master's thesis, which in light of the *JWST* results seem even more interesting.

The 17 sources were selected based on strong Ly$\alpha$ emission, from a parent sample of over 1000 Lyman-break galaxies (LBGs) observed with *HST*'s G800L slitless grism on the Advanced Camera for Surveys (ACS).

As the wavelength coverage of *HST* does not extend to the optical for high-$z$ targets, we only had information on the Ly$\alpha$ emission. Follow-up of these objects with *JWST* is already underway as they are some of the brightest targets in the well-studied Cosmic Assembly Near-infrared Deep Extragalactic Legacy Survey (CANDELS) fields. When this data becomes available, we will have measurements of the H$\alpha$ emission line, which may show broadness just as with MACS J0647−1045 and other LRDs. If these objects are indeed also LRDs, then archival data from *HST* and other telescopes may reveal many more LRD candidates for *JWST* follow-up. This would place further constraints on the AGN mass function in the Cosmic Morning.

# Conclusions

Galaxy formation and evolution began early, with the first galaxies forming over 13 billion years ago, followed by an almost immediate build up of dust and metals. Our study of A1689-zD1 in Part II shows that metal enrichment, at least in some galaxies, may have begun earlier and quicker than previously believed. Recent *JWST* results also seem to support an early formation and evolution scenario (e.g. Robertson et al., 2023; Curtis-Lake et al., 2023). The unexpectedly quick metal enrichment seems to be mirrored in that of dust, with a significant dust mass already in place by $z \sim 7$, although our study suggests that the dust build-up may have lagged behind that of metals. More ALMA metallicity and dust measurements will reveal the exact extent and timeline of this enrichment in the first galaxies.

After the initial assembly of galaxies came a period of transformation from reionisation-era structures into modern galaxies. My work in Part 14.1 on ALPINE data shows that at least a fraction of galaxies (25% in our study) during this period have a disturbed morphology with stars and ISM spatially offset. Such a chaotic internal structure and composition may result from uneven dust production/destruction, or strong stellar feedback and outflows. Together with the larger body of work on ALPINE galaxies, this points to a period of turbulent galaxy growth through heavily dust-obscured star-formation, mergers, and dynamic exchange of gas, dust, and metals with the IGM and CGM. All this activity perhaps was what regulated the metal content of already enriched galaxies, while also allowing metal build-up of metal-poor systems over the next few billion years. Spatially resolved observations at these redshifts can shed light on the true internal structure and physics involved in these transforming systems.

Concurrently with galaxy transformation, black hole growth progressed from early seeds into incredibly numerous obscured AGN. The newly discovered *JWST* LRDs, including the object we study in Part IV, represent this hitherto unexplored class of compact objects with signatures both of AGN and dust-obscured star-formation. The fact that neither spectrum nor morphology of MACS J0647−1045 can be explained with just a star-forming galaxy, or just an AGN alone, and instead requires composite models, shows the tight co-evolution of AGN and their host galaxies during Cosmic Morning. Eventually, either through accretion or mergers, LRDs may form not only heavier SMBH, but also the more massive galaxies seen

at Cosmic Noon. Considering the number of *JWST* LRDs, and that of similarly compact and bright objects in archival *HST* data, the total number of LRDs in the early Universe may be vast indeed. Such high number counts imply a change in the AGN luminosity function, which may alter our theories of cosmic reionisation and SMBH growth. High resolution and integral field spectroscopy may help separate the exact contribution of AGN and host galaxy to observed LRD spectra and morphology, helping us pinpoint the stage of evolution of these systems, so that we may better constrain early BH growth models.

These have been three very small pieces of the astronomical puzzle of galaxy evolution. Now that we have entered the era of extremely powerful telescopes such as ALMA and *JWST*, and with ELT just on the horizon, we may soon be able to map out the exact details of how our modern Universe came to be.

# Extra Material

# Appendix A

# ALPINE Appendices

## A.1 Galaxies with significant offsets

## A.2 Offsets vs selected physical properties

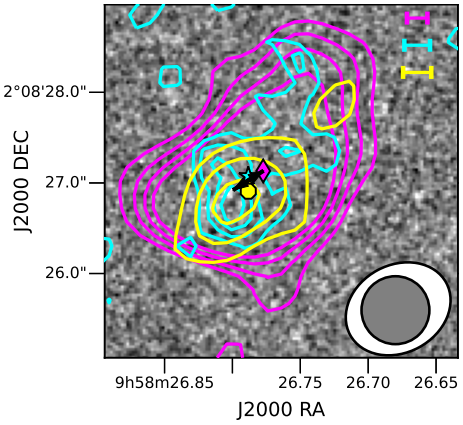


**(a)** Significant [C II]-UV offset in DEIMOS_COSMOS_552206

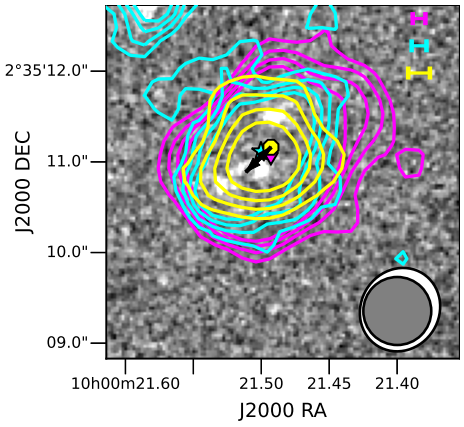


**(b)** Significant offset between UV and [C II]/FIR continuum emission in DEIMOS_COSMOS_848185

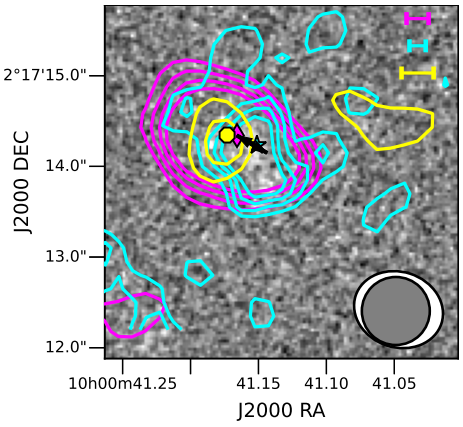


**(c)** Significant [C II]-UV offset in vuds_cosmos_5100994794

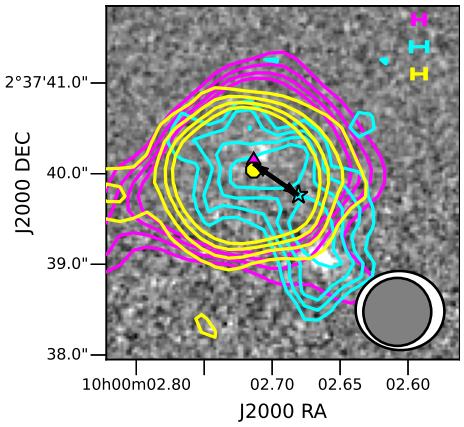


**(d)** Significant offset between Optical and [C II]/FIR continuum emission in DEIMOS_COSMOS_873756

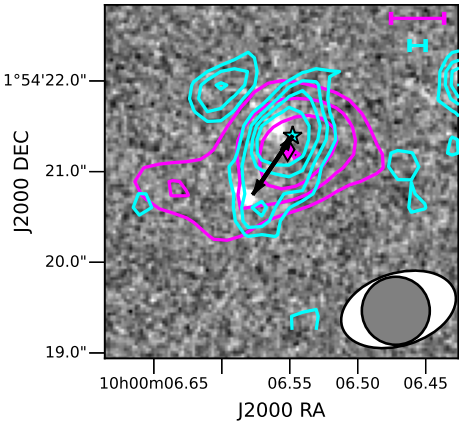


**(e)** Significant Optical-UV offset in DEIMOS_COSMOS_403030

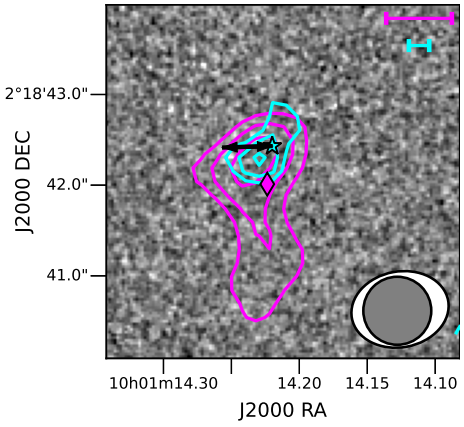


**(f)** Significant Optical-UV offset in DEIMOS_COSMOS_665626

**Figure A.1:** Galaxies with significant offsets. Colour scheme is the same as Fig. 16.2.

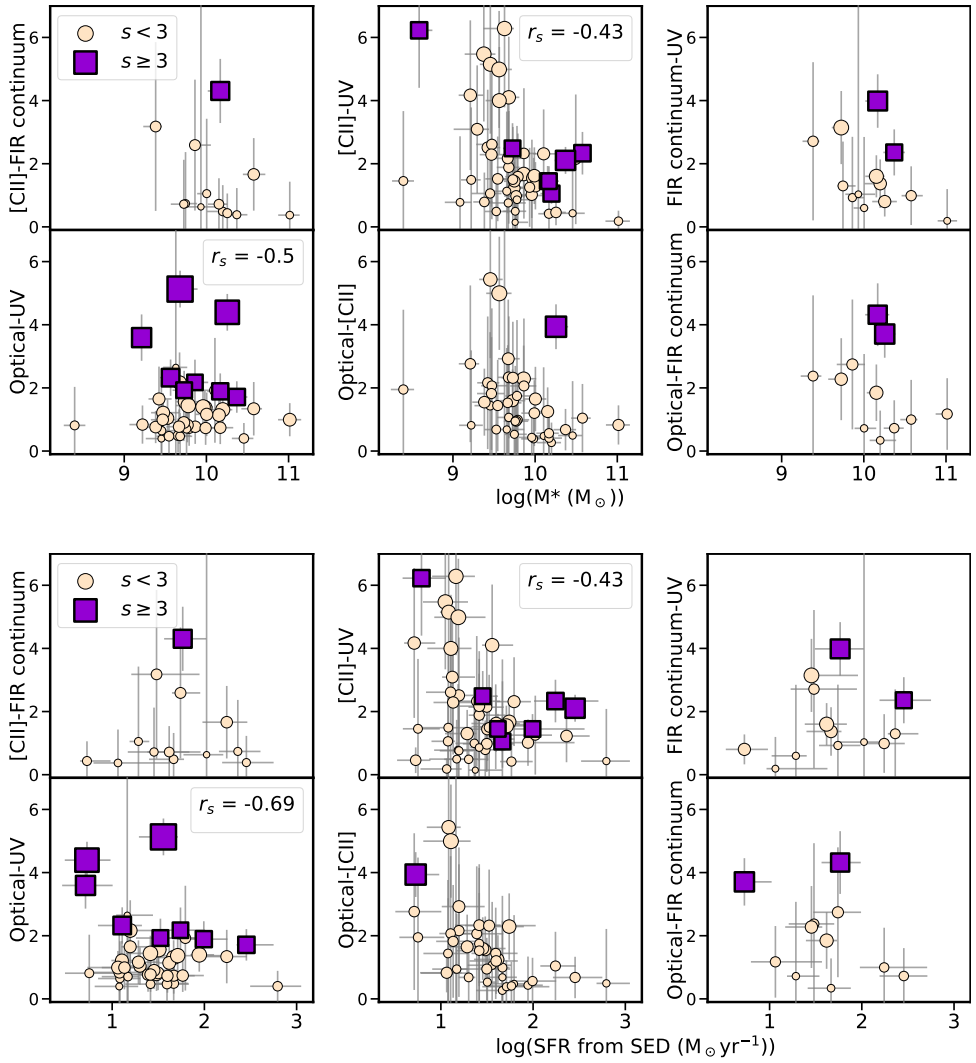


**Figure A.2:** Offsets (in kpc) vs physical properties a) log(Stellar mass) b) Total SFR. Colour scheme and parameters are the same as in Fig. 17.1.

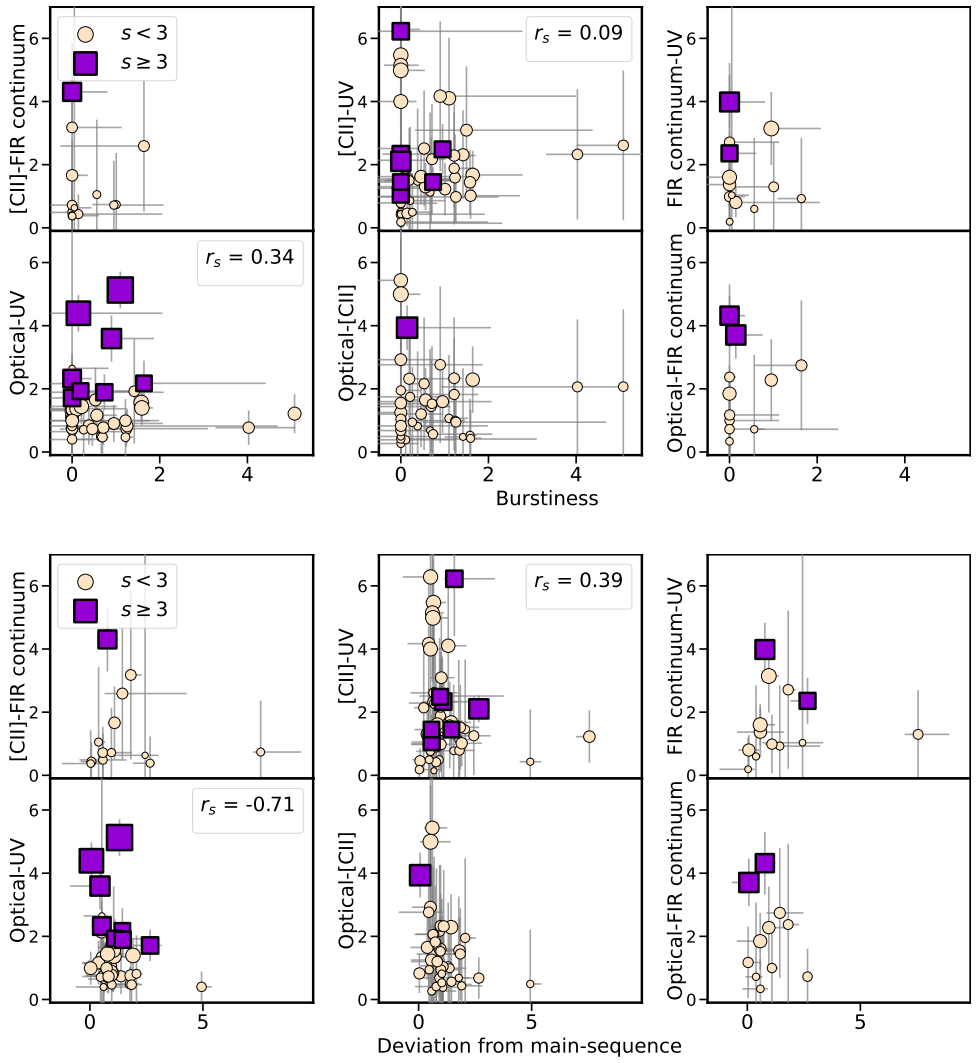


**Figure A.2:** (contd.) c) Burstiness (as in Fig. 17.1c) d) deviation from main-sequence (as in Fig. 17.1d)

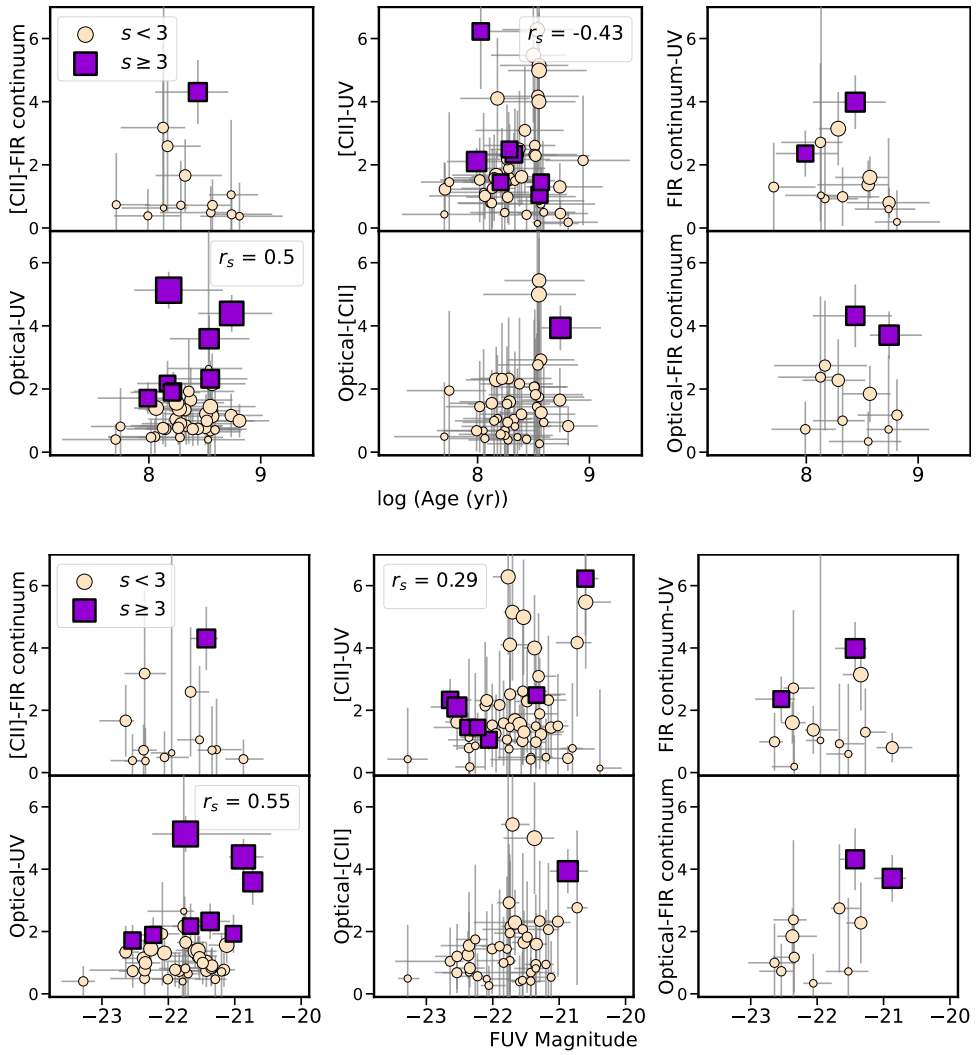


**Figure A.2:** (contd.) e) log(Age) f) FUV magnitude

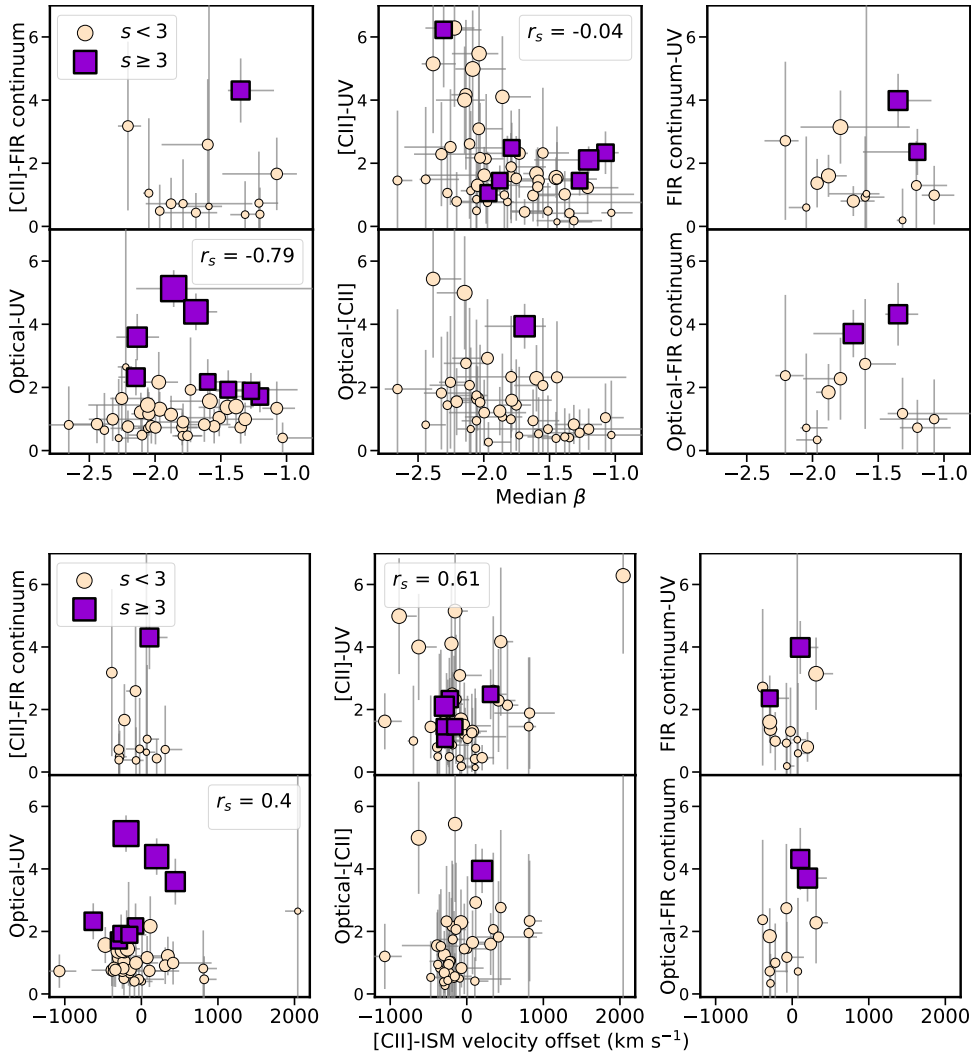


**Figure A.2:** (contd.) g) median UV continuum slope $\beta$ (as in Fig. 17.1f), h) Ly$\alpha$-[C II] velocity offset (as in Fig. 17.1e)

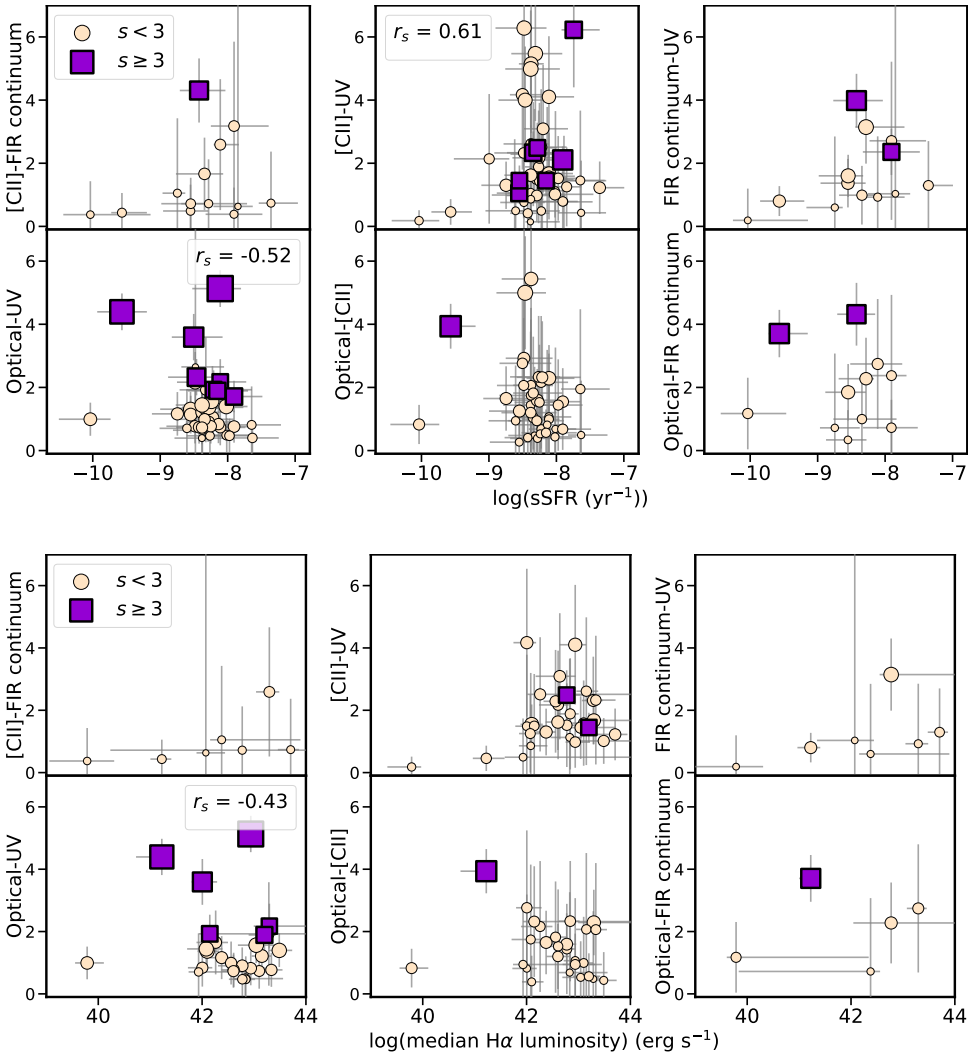


**Figure A.2:** (contd.) i) Total specific SFR, j) median Hα luminosity

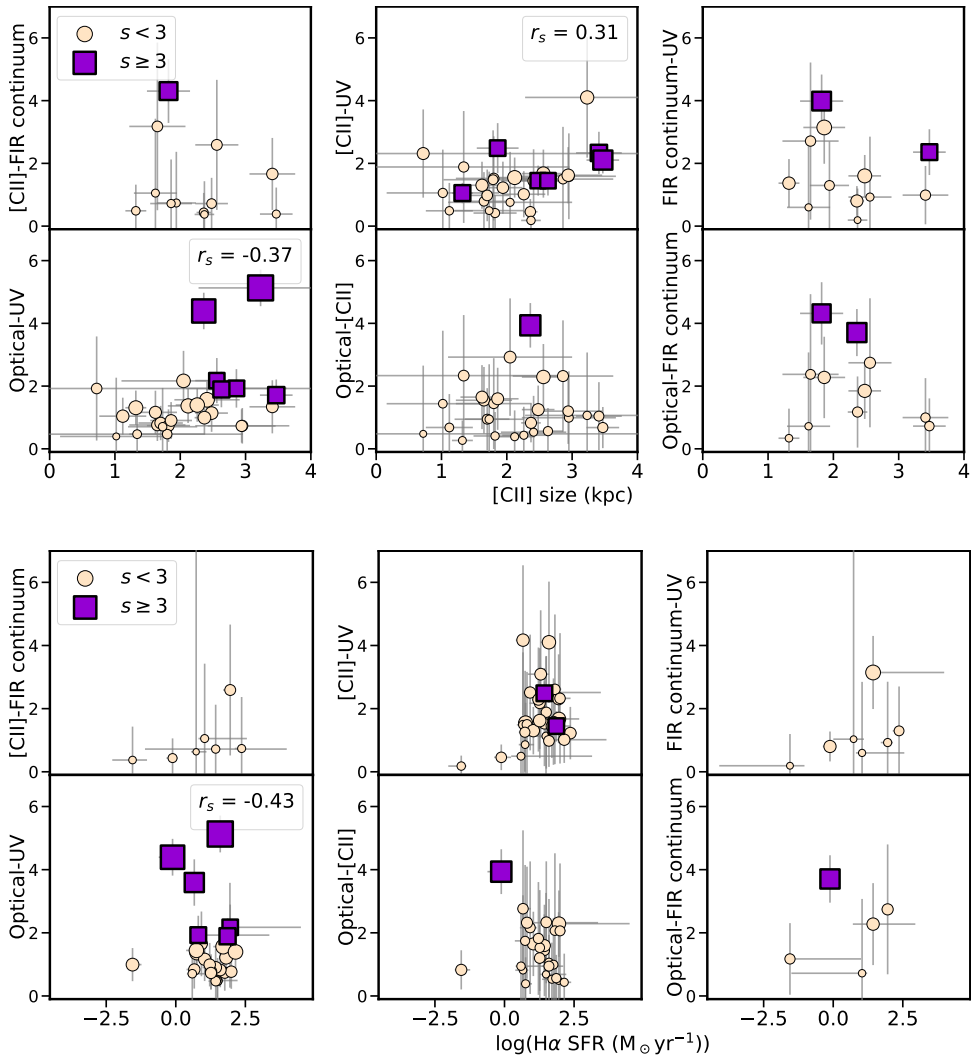


**Figure A.2:** (contd.) k) [C II] size in kpc l) Hα SFR in $M_\odot$ $yr^{-1}$

# Appendix B

# *JWST* Appendix

## B.1 Hα fits to assess line broadness

## B.2 Optical/NIR continuum fit with a blackbody

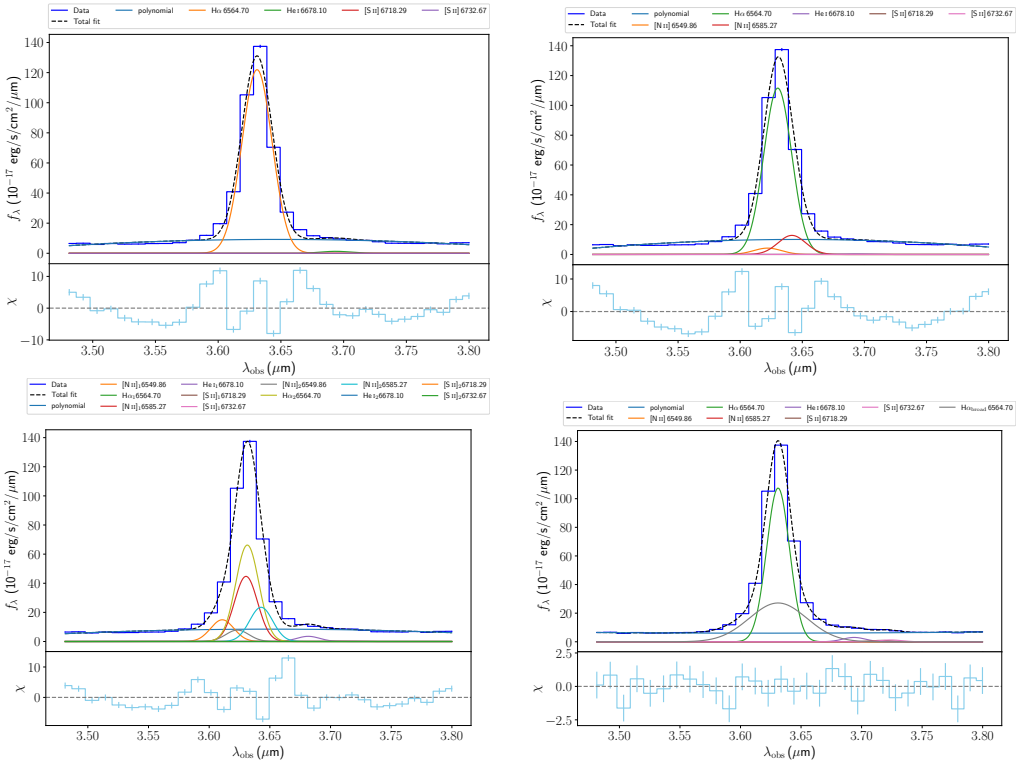


**Figure B.1:** Fits to the Hα line under various assumptions: *Top left:* A narrow Gaussian for Hα, [He I], and [S II] doublet lines, showing significant residuals. The continuum is fit with a simple second order polynomial. *Top right:* Same as left panel, but including the [N II] doublet; the fit does not improve. *Bottom left:* Two sets of narrow Gaussians at different redshifts for all lines including [N II], simulating a merging system. Residuals are still very significant. *Bottom right:* Narrow Gaussians for all emission lines, but adding a broad Hα component. The residuals are much improved. This model also includes the [N II] doublet, but the fit completely suppresses it in favour of broad Hα emission.

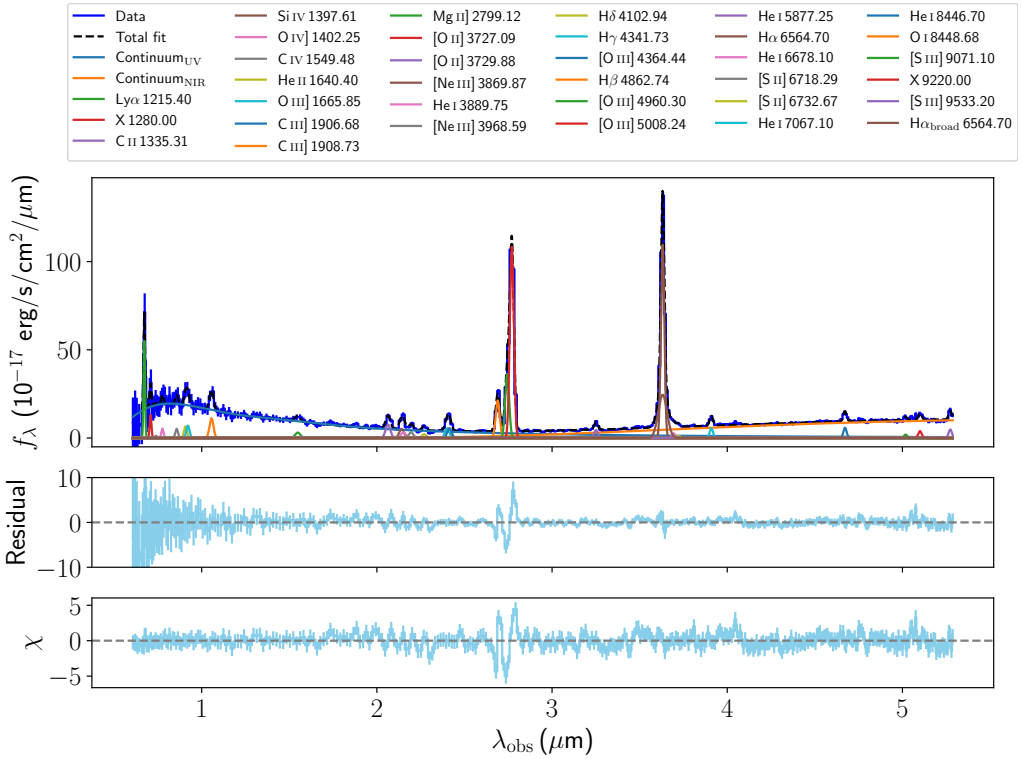


**Figure B.2:** The same as the best fit model shown in Fig. 22.2, but with a blackbody Planck function instead of a power law to model the optical/NIR continuum. We find a blackbody termperature of $T_b$ of $\sim$ 2500 K. We find no extinction on this curve ($A_V \sim 0$).

# Bibliography


Adler S. L., 2021, IJMPD, 31, 2242007

Aghanim N., et al., 2020, Astronomy and Astrophysics, 641

Akins H., et al., 2022, The Astrophysical Journal

Akiyama K., et al., 2019, The Astrophysical Journal, 875, L1

Alvarez M. A., Finlator K., Trenti M., 2012, Astrophysical Journal Letters, 759

Antonucci R., Antonucci Robert 1993, ARA&A, 31, 473

Antonucci R., Antonucci R. 2012, A&AT, 27, 557

Arata S., Yajima H., Nagamine K., Li Y., Khochfar S., 2018, MNRAS, 488, 2629

Arnouts S., Ilbert O., 2011, Astrophysics Source Code Library, record ascl:1108.009, p. ascl:1108.009

Arnouts S., Cristiani S., Moscardini L., Matarrese S., Lucchin F., Fontana A., Giallongo E., 1999, ascl, 310, ascl:1108.009

Asano R. S., Takeuchi T. T., Hirashita H., Inoue A. K., 2013, Earth, Planets and Space, 65, 213

Atek H., Furtak L., Oesch P., van Dokkum P., Reddy N., Contini T., Illingworth G., Wilkins S., 2022, Monthly Notices of the Royal Astronomical Society, 511, 4464

Backhaus B. E., et al., 2022, The Astrophysical Journal, 926, 161

Bakx T. J. L. C., et al., 2020, Monthly Notices of the Royal Astronomical Society, 493, 4294

Bakx T. J. L. C., et al., 2021, Monthly Notices of the Royal Astronomical Society: Letters, 508, L58–L63

Bakx T. J. L. C., et al., 2023, Monthly Notices of the Royal Astronomical Society, 519, 5076

Baldassare V. F., et al., 2016, The Astrophysical Journal, 829, 57

Baldwin J. A., Phillips M. M., Terlevich R., 1981, PASP, 93, 5

Bamford S. P., Häußler B., Rojas A., Borch A., Bamford S. P., Häußler B., Rojas A., Borch A., 2011, ASPC, 442, 479

Bañados E., et al., 2018, The Astrophysical Journal, 856, L25

Barchiesi L., et al., 2023, Astronomy & Astrophysics, 675, A30

Barkana R., Loeb A., 2001, Physics Reports, 349, 125

Baron D., et al., 2018, Monthly Notices of the Royal Astronomical Society, 480, 3993

Barro G., et al., 2023, Extremely red galaxies at $z=5-9$ with MIRI and NIRSpec: dusty galaxies or obscured AGNs?, http://arxiv.org/abs/2305.14418

Barrufet L., et al., 2023, MNRAS, 522, 3926

Behrens C., Pallottini A., Ferrara A., Gallerani S., Vallini L., 2018, Monthly Notices of the Royal Astronomical Society, 477, 552

Bentz M. C., Manne-Nicholas E., 2018, The Astrophysical Journal, 864, 146

Bentz M. C., et al., 2013, Astrophysical Journal, 767, 149

Béthermin M., et al., 2016, Astronomy and Astrophysics, 586, L7

Béthermin M., et al., 2020, Astronomy & Astrophysics, 643, A2

Bianchi S., et al., 2022, Astronomy & Astrophysics, 664, A187

Birkin J. E., et al., 2023, JWST's TEMPLATES for Star Formation: The First Resolved Gas-Phase Metallicity Maps of Dust-Obscured Star-Forming Galaxies at $z$ $\sim$ 4, http://arxiv.org/abs/2307.10412

Bischetti M., Maiolino R., Carniani S., Fiore F., Piconcelli E., Fluetsch A., 2019, Astronomy & Astrophysics, 630, A59

Blandford R. D., McKee C. F., Blandford R. D., McKee C. F., 1982, ApJ, 255, 419

Boquien M., Burgarella D., Roehlly Y., Buat V., Ciesla L., Corre D., Inoue A. K., Salas H., 2019, Astronomy and Astrophysics, 622, A103

Boquien M., et al., 2022, Astronomy and Astrophysics, 663

Boselli A., Gavazzi G., Lequeux J., Pierini D., 2002, Astronomy and Astrophysics, 385, 454

Bosman S. E., Fan X., Jiang L., Reed S., Matsuoka Y., Becker G., Haehnelt M., 2018, Monthly Notices of the Royal Astronomical Society, 479, 1055

Bosman S. E. I., et al., 2023, First rest-frame infrared spectrum of a z>7 quasar: JWST/MRS observations of J1120+0641, http://arxiv.org/abs/2307.14414

Bouché N., et al., 2010, Astrophysical Journal, 718, 1001

Bouwens R., et al., 2016, The Astrophysical Journal, 833, 72

Bouwens R. J., et al., 2022, The Astrophysical Journal, 931, 160

Bouwens R. J., et al., 2023, Monthly Notices of the Royal Astronomical Society, 523, 1036

Bowler R. A., Bourne N., Dunlop J. S., McLure R. J., McLeod D. J., 2018, Monthly Notices of the Royal Astronomical Society, 481, 1631

Bowler R. A. A., Cullen F., McLure R. J., Dunlop J. S., Avison A., 2022, Monthly Notices of the Royal Astronomical Society, 510, 5088

Bradley L. D., et al., 2008, The Astrophysical Journal, 678, 647

Brammer G., 2023, msaexp: NIRSpec analyis tools, doi:10.5281/ZENODO.8233475, https://zenodo.org/record/8233475

Brauher J. R., Dale D. A., Helou G., 2008, The Astrophysical Journal Supplement Series, 178, 280

Bromm V., Loeb A., 2003a, Nature, 425, 812

Bromm V., Loeb A., 2003b, The Astrophysical Journal, 596, 34

Bromm V., Coppi P. S., Larson R. B., 2002, The Astrophysical Journal, 564, 23

Buat V., Ciesla L., Boquien M., Małek K., Burgarella D., 2019, Astronomy and Astrophysics, 632, A79

Bunker A. J., et al., 2023a, JADES NIRSpec Initial Data Release for the Hubble Ultra Deep Field Redshifts and Line Fluxes of Distant Galaxies from the Deepest JWST Cycle 1 NIRSpec Multi-Object Spectroscopy, https://archive.stsci.edu/hlsp/jades

Bunker A. J., et al., 2023b, A&A, 677, A88

Burgarella D., Buat V., Iglesias-Paramo J., 2005, MNRAS, 360, 1413

Burgarella D., Nanni A., Hirashita H., Theulé P., Inoue A. K., Takeuchi T. T., 2020, Astronomy and Astrophysics, 637, A32

Cackett E. M., Bentz M. C., Kara E., 2021, iScience, 24, 102557

Calabrò A., et al., 2022, Astronomy and Astrophysics, 664, A75

Calzetti D., Armus L., Bohlin R. C., Kinney A. L., Koornneef J., Storchi-Bergmann T., 2000, The Astrophysical Journal, 533, 682

Campitiello S., Celotti A., Ghisellini G., Sbarrato T., 2020, Astronomy and Astrophysics, 640, A39

Capak P. L., et al., 2015, Nature, 522, 455

Cardamone C. N., et al., 2010, The Astrophysical Journal Supplement Series, 189, 270

Carilli C., Walter F., 2013, Annual Review of Astronomy and Astrophysics, 51, 105

Carniani S., et al., 2013, Astronomy and Astrophysics, 559

Carniani S., et al., 2017, Astronomy and Astrophysics, 605, A42

Carniani S., et al., 2018, Monthly Notices of the Royal Astronomical Society, 478, 1170

Carniani S., et al., 2020, Monthly Notices of the Royal Astronomical Society, 499, 5136

Carraro R., et al., 2020, Astronomy and Astrophysics, 642, A65

Casey C. M., et al., 2014, Astrophysical Journal, 796, 95

Cassata P., et al., 2020, Astronomy & Astrophysics, 643, A6

Ceverino D., Klypin A., 2009, The Astrophysical Journal, 695, 292

Chabrier G., 2003, Publications of the Astronomical Society of the Pacific, 115, 763

Chantavat T., Chongchitnan S., Silk J., 2023, Monthly Notices of the Royal Astronomical Society, 522, 3256

Chartab N., et al., 2022, Nature Astronomy

Chen Z., Stark D. P., Endsley R., Topping M., Whitler L., Charlot S., 2022, Monthly Notices of the Royal Astronomical Society, 518, 5607

Chen Y., et al., 2023, MNRAS, 519, 6199

Cherchneff I., Dwek E., 2010, Astrophysical Journal, 713, 1

Chornock R., et al., 2014, arXiv, p. arXiv:1405.7400

Christensen L., et al., 2023, Metal enrichment and evolution in four z > 6.5 quasar sightlines observed with JWST/NIRSpec, http://arxiv.org/abs/2309.06470

Cicone C., et al., 2015, Astronomy & Astrophysics, 574, A14

Cid Fernandes R., Stasińska G., Schlickmann M. S., Mateus A., Vale Asari N., Schoenell W., Sodré L., 2010, Monthly Notices of the Royal Astronomical Society, 403, 1036

Clark C. J. R., et al., 2019, Monthly Notices of the Royal Astronomical Society, 489, 5256

Cochrane R. K., et al., 2021, Monthly Notices of the Royal Astronomical Society, 503, 2622

Collin S., Boisson C., Mouchet M., Dumont A. M., Coupé S., Porquet D., Rokaki E., 2002, Astronomy and Astrophysics, 388, 771

Conroy C., Gunn J. E., 2010, Astrophysical Journal, 712, 833

Conroy C., Gunn J. E., White M., 2009, Astrophysical Journal, 699, 486

Conselice C. J., 2014, https://doi.org/10.1146/annurev-astro-081913-040037, 52, 291

Corazza L. C., Miranda O. D., Wuensche C. A., 2022, Astronomy and Astrophysics, 668, A191

Cormier D., et al., 2019, Astronomy & Astrophysics, 626, A23

Cowie L. L., Barger A. J., 2008, ApJ, 686, 72

Crain R. A., Voort F. v. d., 2023, https://doi.org/10.1146/annurev-astro-041923-043618, 61

Croxall K. V., et al., 2013, ApJ, 777, 96

Cullen F., et al., 2023, MNRAS, 520, 14

Curti M., et al., 2020, Monthly Notices of the Royal Astronomical Society, 492, 821

Curti M., et al., 2022, Monthly Notices of the Royal Astronomical Society, p. stac2737

Curtis-Lake E., et al., 2023, Nature Astronomy, 7, 622

Da Cunha E., Charlot S., Elbaz D., 2008, Monthly Notices of the Royal Astronomical Society, 388, 1595

Datta K. K., Bharadwaj S., Choudhury T. R., 2007, Monthly Notices of the Royal Astronomical Society, 382, 809

Davé R., Finlator K., Oppenheimer B. D., 2011, Monthly Notices of the Royal Astronomical Society, 416, 1354

Davé R., Finlator K., Oppenheimer B. D., 2012, Monthly Notices of the Royal Astronomical Society, 421, 98

Davé R., Finlator K., Oppenheimer B. D., Hartwig T., Yoshida N., 2019, ApJL, 870, L3

Davies R. L., et al., 2019, The Astrophysical Journal, 873, 122

Dayal P., Ferrara A., Dunlop J. S., 2013, Monthly Notices of the Royal Astronomical Society, 430, 2891

Dayal P., Ferrara A., Dayal P., Ferrara A., 2018, PhR, 780, 1

De Breuck C., et al., 2014, Astronomy and Astrophysics, 565, A59

De Cia A., Ledoux C., Mattsson L., Petitjean P., Srianand R., Gavignaud I., Jenkins E. B., 2016, Astronomy and Astrophysics, 596

De Looze I., et al., 2014, Astronomy and Astrophysics, 568, A62

De Rossi M. E., Bromm V., 2017, Monthly Notices of the Royal Astronomical Society, 465, 3668

De Vis P., et al., 2019, Astronomy & Astrophysics, 623, A5

Decarli R., et al., 2019a, The Astrophysical Journal, 880, 157

Decarli R., et al., 2019b, The Astrophysical Journal, 882, 138

Dekel A., Mandelker N., 2014, Monthly Notices of the Royal Astronomical Society, 444, 2071

Dekel A., et al., 2009, Nature, 457, 451

Dekel A., Sarkar K. C., Birnboim Y., Mandelker N., Li Z., 2023, Monthly Notices of the Royal Astronomical Society, 523, 3201

Denney K. D., Peterson B. M., Dietrich M., Vestergaard M., Bentz M. C., 2009, Astrophysical Journal, 692, 246

Dessauges-Zavadsky M., et al., 2020, Astronomy and Astrophysics, 643, A5

Ding X., et al., 2020, The Astrophysical Journal, 888, 37

Donevski D., et al., 2020, A&A, 644, A144

Donnan C. T., et al., 2022, Monthly Notices of the Royal Astronomical Society, 518, 6011

Dopita M. A., Nicholls D. C., Sutherland R. S., Kewley L. J., Groves B. A., 2016, The Astrophysical Journal, 824, L13

Dors O. L., Agarwal B., Hägele G. F., Cardaci M. V., Rydberg C. E., Riffel R. A., Oliveira A. S., Krabbe A. C., 2018, Monthly Notices of the Royal Astronomical Society, 479, 2294

Draine B. T., 2009. http://arxiv.org/abs/0903.1658

Dunne L., et al., 2009, Monthly Notices of the Royal Astronomical Society, 394, 1307

Dwek E., 1998, The Astrophysical Journal, 501, 643

Ebeling H., Edge A. C., Mantz A., Barrett E., Henry J. P., Ma C. J., van Speybroeck L., 2010, Monthly Notices of the Royal Astronomical Society, Volume 407, Issue 1, pp. 83-93., 407, 83

Eisenstein D. J., et al., 2023, Overview of the JWST Advanced Deep Extragalactic Survey (JADES), https://arxiv.org/abs/2306.02465v1

El Youssoufi D., et al., 2019, Monthly Notices of the Royal Astronomical Society, 490, 1076

Elbaz D., et al., 2018, Astronomy and Astrophysics, 616, A110

Fabian A. C., 2012, ARA&A, 50, 455

Faisst A. L., et al., 2017, The Astrophysical Journal, 847, 21

Faisst A. L., Capak P. L., Emami N., Tacchella S., Larson K. L., 2019, The Astrophysical Journal, 884, 133

Faisst A. L., et al., 2020, The Astrophysical Journal Supplement Series, 247, 61

Fan X., Carilli C. L., Keating B., 2006, https://doi.org/10.1146/annurev.astro.44.051905.092514, 44, 415

Farina E. P., et al., 2022, The Astrophysical Journal, 941, 106

Feltre A., Charlot S., Gutkin J., 2016, Monthly Notices of the Royal Astronomical Society, 456, 3354

Ferrara A., et al., 2022, Monthly Notices of the Royal Astronomical Society, 512, 58

Ferrarese L., Merritt D., 2000, The Astrophysical Journal, 539, L9

Ferrarotti A. S., Gail H. P., Ferrarotti A. S., Gail H. P., 2006, A&A, 447, 553

Finkelstein S. L., et al., 2022, The Astrophysical Journal Letters, Volume 946, Issue 1, id.L13, <NUMPAGES>35</NUMPAGES> pp., 946, L13

Fiore F., et al., 2017, Astronomy and Astrophysics, 601, A143

Fluetsch A., et al., 2019, Monthly Notices of the Royal Astronomical Society, 483, 4586

Forgan D. H., Rowlands K., Gomez H. L., Gomez E. L., Schofield S. P., Dunne L., Maddox S., 2017, Monthly Notices of the Royal Astronomical Society, 472, 2289

Förster Schreiber N. M., Wuyts S., 2020, https://doi.org/10.1146/annurev-astro-032620-021910, 58, 661

Fudamoto Y., et al., 2020, Astronomy and Astrophysics, 643

Fudamoto Y., et al., 2021, Nature, 597, 489

Fudamoto Y., Inoue A. K., Sugahara Y., 2023, Monthly Notices of the Royal Astronomical Society, 521, 2962

Fujimoto S., et al., 2020, The Astrophysical Journal, 900, 1

Fujimoto S., et al., 2021, The Astrophysical Journal, 911, 99

Fujimoto S., et al., 2022a, arXiv, p. arXiv:2212.06863

Fujimoto S., et al., 2022b, Nature, 604, 261

Fujimoto S., et al., 2023a, CEERS Spectroscopic Confirmation of NIRCam-Selected z $>$ 8 Galaxy Candidates with JWST/NIRSpec: Initial Characterization of their Properties, doi:10.3847/2041-8213/acd2d9, http://arxiv.org/abs/2301.09482http://dx.doi.org/10.3847/2041-8213/acd2d9

Fujimoto S., et al., 2023b, arXiv, p. arXiv:2309.07834

Fumagalli M., O'Meara J. M., Prochaska J. X., 2011, Science, 334, 1245

Furlanetto S. R., Loeb A., 2003, The Astrophysical Journal, 588, 18

Furlanetto S. R., Zaldarriaga M., Hernquist L., 2004, The Astrophysical Journal, 613, 1

Furtak L. J., et al., 2023a, arXiv, p. arXiv:2308.05735

Furtak L. J., et al., 2023b, Monthly Notices of the Royal Astronomical Society, 522, 5142

Galametz M., Madden S. C., Galliano F., Hony S., Bendo G. J., Sauvage M., 2011, A&A, 532, A56

Gall C., Hjorth J., Andersen A. C., 2011, Astronomy and Astrophysics Review, 19, 43

Galliano F., Madden S. C., Jones A. P., Wilson C. D., Bernard J. P., 2005, Astronomy and Astrophysics, 434, 867

Galliano F., Galametz M., Jones A. P., 2018, Annual Review of Astronomy and Astrophysics, 56, 673

Garnett D. R., 2002, ApJ, 581, 1019

Gebhardt K., et al., 2000, The Astrophysical Journal, 539, L13

Giallongo E., et al., 2015, Astronomy & Astrophysics, 578, A83

Giavalisco M., Team t. G., 2003, The Astrophysical Journal, 600, L93

Ginolfi M., Graziani L., Schneider R., Marassi S., Valiante R., Dell'Agli F., Ventura P., Hunt L. K., 2018, Monthly Notices of the Royal Astronomical Society, 473, 4538

Ginolfi M., et al., 2020a, Astronomy & Astrophysics, 633, A90

Ginolfi M., et al., 2020b, A&A, 643, A7

Ginsburg A., et al., 2019, radio-astro-tools/spectral-cube: v0.4.4, doi:10.5281/ZENODO.2573901, `https://zenodo.org/record/2573901`

Gnedin N. Y., Madau P., Org P., 2022, Living Reviews in Computational Astrophysics 2022 8:1, 8, 1

Gómez-Guijarro C., et al., 2018, The Astrophysical Journal, 856, 121

González-López J., et al., 2017, Astronomy and Astrophysics, 597

Gordon K. D., Clayton G. C., Misselt K. A., Landolt A. U., Wolff M. J., 2003, The Astrophysical Journal, 594, 279

Graziani L., de Bennassuti M., Schneider R., Kawata D., Salvadori S., 2017, Monthly Notices of the Royal Astronomical Society, 469, 1101

Graziani L., Schneider R., Ginolfi M., Hunt L. K., Maio U., Glatzle M., Ciardi B., 2020, Monthly Notices of the Royal Astronomical Society, 494, 1071

Green G., 2018, Journal of Open Source Software, 3, 695

Greene J. E., Ho L. C., 2005, The Astrophysical Journal, 630, 122

Greene J. E., et al., 2023, UNCOVER spectroscopy confirms a surprising ubiquity of AGN in red galaxies at $z>5$, http://arxiv.org/abs/2309.05714

Gruppioni C., et al., 2020, Astronomy and Astrophysics, 643, A8

Guhathakurta P., Draine B. T., 1989, The Astrophysical Journal, 345, 230

Guo Y., Giavalisco M., Ferguson H. C., Cassata P., Koekemoer A. M., 2012, Astrophysical Journal, 757, 120

Haemmerlé L., Mayer L., Klessen R. S., Hosokawa T., Madau P., Bromm V., 2020, Space Science Reviews, 216, 48

Harikane Y., et al., 2020, The Astrophysical Journal, 896, 93

Harikane Y., et al., 2023, JWST/NIRSpec First Census of Broad-Line AGNs at z=4-7: Detection of 10 Faint AGNs with M_BH~10^6-10^7 M_sun and Their Host Galaxy Properties, http://arxiv.org/abs/2303.11946

Hashimoto T., et al., 2018, Nature, 557, 392

Hashimoto T., et al., 2019, Publications of the Astronomical Society of Japan, 71, 71

Hatcher C., et al., 2021, The Astronomical Journal, 162, 65

Hatsukade B., Tamura Y., Iono D., Matsuda Y., Hayashi M., Oguri M., 2015, Publications of the Astronomical Society of Japan, 67

Häußler B., et al., 2013, Monthly Notices of the Royal Astronomical Society, 430, 330

Hayes M., et al., 2010, Natur, 464, 562

Heintz K. E., Watson D., Oesch P. A., Narayanan D., Madden S. C., 2021, The Astrophysical Journal, 922, 147

Heintz K. E., et al., 2023a, arXiv, p. arXiv:2306.00647

Heintz K. E., et al., 2023b, The Astrophysical Journal Letters, 944, L30

Henry R. B. C., Edmunds M. G., Köppen J., 2000, The Astrophysical Journal, 541, 660

Henry A., et al., 2013, Astrophysical Journal Letters, 776, L27

Herrera-Camus R., et al., 2015, The Astrophysical Journal, 800, 1

Herrera-Camus R., et al., 2021, Astronomy and Astrophysics, 649

Hirashita H., Ferrara A., Dayal P., Ouchi M., 2014, Monthly Notices of the Royal Astronomical Society, 443, 1704

Hjorth J., Vreeswijk P. M., Gall C., Watson D., 2013, ApJ, 768, 173

Hodge J. A., da Cunha E., 2020, Royal Society Open Science, 7, 200556

Hodge J. A., Carilli C. L., Walter F., De Blok W. J., Riechers D., Daddi E., Lentati L., 2012, Astrophysical Journal, 760, 11

Hodge J. A., et al., 2016, The Astrophysical Journal, 833, 103

Hollenbach D. J., Tielens A. G. G. M., Hollenbach D. J., Tielens A. G. G. M., 1999, RvMP, 71, 173

Hönig S. F., Kishimoto M., 2010, Astronomy and Astrophysics, 523, A27

Hopkins P. F., Hernquist L., Cox T. J., Kereš D., 2008, The Astrophysical Journal Supplement Series, 175, 356

Horne K., 1986, Publications of the Astronomical Society of the Pacific, 98, 609

Hoyle F., Fowler W. A., Hoyle F., Fowler W. A., 1963, MNRAS, 125, 169

Hoyle F., Wickramasinghe N. C., Hoyle F., Wickramasinghe N. C., 1970, Natur, 226, 62

Hsu Y. M., Hirashita H., Lin Y. H., Camps P., Baes M., 2023, Monthly Notices of the Royal Astronomical Society, 519, 2475

Hu E. M., Cowie L. L., McMahon R. G., Capak P., Iwamuro F., Kneib J.-P., Maihara T., Motohara K., 2002, The Astrophysical Journal, 568, L75

Hubble P. E., 1925, PA, 33, 252

Hubble E. P., Hubble P. E., 1926, ApJ, 64, 321

Hutchison T. A., et al., 2019, The Astrophysical Journal, 879, 70

Hygate A. P. S., et al., 2023, Monthly Notices of the Royal Astronomical Society, 524, 1775

Ilbert O., et al., 2006, Astronomy and Astrophysics, 457, 841

Inami H., et al., 2022, Monthly Notices of the Royal Astronomical Society, 515, 3126

Inayoshi K., Visbal E., Haiman Z., 2020, Annual Review of Astronomy and Astrophysics, 58, 27

Inoue A. K., Shimizu I., Tamura Y., Matsuo H., Okamoto T., Yoshida N., 2014, Astrophysical Journal Letters, 780, L18

Isobe Y., et al., 2023, arXiv, p. arXiv:2307.00710

Jakobsen P., et al., 2022, arXiv:2202.03305 [astro-ph]

Jeon M., Bromm V., Pawlik A. H., Milosavljević M., 2015, Monthly Notices of the Royal Astronomical Society, 452, 1152

Jeon J., Bromm V., Finkelstein S. L., 2022, Monthly Notices of the Royal Astronomical Society, 515, 5568

Johnson J. W., Weinberg D. H., Vincenzo F., Bird J. C., Griffith E. J., 2022, MNRAS, 520, 782

Jones G. C., et al., 2020a, Monthly Notices of the Royal Astronomical Society: Letters, 491, L18

Jones T., Sanders R., Roberts-Borsani G., Ellis R. S., Laporte N., Treu T., Harikane Y., 2020b, The Astrophysical Journal, 903, 150

Jones G. C., et al., 2021, Monthly Notices of the Royal Astronomical Society, 507, 3540

Jones T., et al., 2023, The Astrophysical Journal Letters, 951, L17

Kaasinen M., et al., 2023, Astronomy & Astrophysics, 671, A29

Kacprzak G. G., et al., 2016, The Astrophysical Journal, 826, L11

Kahre L., et al., 2018, The Astrophysical Journal, 855, 133

Kashino D., Lilly S. J., Matthee J., Eilers A.-C., Mackenzie R., Bordoloi R., Simcoe R. A., 2023, The Astrophysical Journal, 950, 66

Kaspi S., Smith P. S., Netzer H., Maoz D., Jannuzi B. T., Giveon U., 2000, The Astrophysical Journal, 533, 631

Katz H., Kimm T., Sijacki D., Haehnelt M. G., 2017, Monthly Notices of the Royal Astronomical Society, 468, 4831

Katz H., et al., 2019, Monthly Notices of the Royal Astronomical Society, 487, 5902

Katz H., et al., 2021, MNRAS, 510, 5603

Katz H., et al., 2023, Monthly Notices of the Royal Astronomical Society, 518, 592

Kauffmann G., et al., 2003, MNRAS, 346, 1055

Kennicutt R. C., Evans N. J., 2012, Annual Review of Astronomy and Astrophysics, 50, 531

Kewley L. J., Dopita M. A., 2002, The Astrophysical Journal Supplement Series, 142, 35

Kewley L. J., Dopita M. A., Sutherland R. S., Heisler C. A., Trevena J., 2001, The Astrophysical Journal, 556, 121

Kewley L. J., Maier C., Yabe K., Ohta K., Akiyama M., Dopita M. A., Yuan T., 2013, The Astrophysical Journal, 774, L10

Kewley L. J., Nicholls D. C., Sutherland R. S., 2019, Annual Review of Astronomy and Astrophysics, 57, 511

Khusanova Y., et al., 2021, Astronomy and Astrophysics, 649, A152

Killi M., et al., 2023, Monthly Notices of the Royal Astronomical Society

Kim D., et al., 2015, Astrophysical Journal, Supplement Series, 216, 17

Kim J.-h., Wise J. H., Abel T., Jo Y., Primack J. R., Hopkins P. F., 2019, The Astrophysical Journal, 887, 120

Kirby E. N., Martin C. L., Finlator K., 2011, Astrophysical Journal Letters, 742, L25

Kishimoto M., Hoenig S. F., Beckert T., Weigelt G., 2007, A&A, 476, 713

Knudsen K. K., Watson D., Frayer D., Christensen L., Gallazzi A., Michalowski M. J., Richard J., Zavala J., 2017, Monthly Notices of the Royal Astronomical Society, 466, 138

Kobayashi H., Watanabe S. i., Kimura H., Yamamoto T., 2009, Icarus, Volume 201, Issue 1, p. 395-405., 201, 395

Kobayashi C., Karakas A. I., Lugaro M., 2020, The Astrophysical Journal, 900, 179

Kobulnicky H. A., Kennicutt Jr. R. C., Pizagno J. L., 1999, The Astrophysical Journal, 514, 544

Kocevski D. D., et al., 2023, 20 ANTONELLO CALABRÒ, 10, 23

Koekemoer A. M., et al., 2007, The Astrophysical Journal Supplement Series, 172, 196

Koekemoer A. M., et al., 2011, The Astrophysical Journal Supplement Series, 197, 36

Kohandel M., Pallottini A., Ferrara A., Zanella A., Behrens C., Carniani S., Gallerani S., Vallini L., 2019, Monthly Notices of the Royal Astronomical Society, 487, 3007

Kojima T., Ouchi M., Nakajima K., Shibuya T., Harikane Y., Ono Y., 2017, Publications of the Astronomical Society of Japan, 69

Kokorev V., et al., 2023, Bingjie Wang, 19, 17

Kokubo M., Kokubo Mitsuru 2023, arXiv, 000, arXiv:2308.04959

Kolborg A. N., Martizzi D., Ramirez-Ruiz E., Pfister H., Sakari C., Wechsler R. H., Soares-Furtado M., 2022, The Astrophysical Journal Letters, 936, L26

Kormendy J., Ho L. C., 2013, https://doi.org/10.1146/annurev-astro-082708-101811, 51, 511

Kriek M., et al., 2011, ApJ, 743, 168

Kumar S., Dewangan G. C., Singh K. P., Gandhi P., Papadakis I. E., Tripathi P., Mallick L., 2023, The Astrophysical Journal, 950, 90

Kunth D., et al., 1998, A&A, 334, 11

Labbe I., et al., 2023, UNCOVER: Candidate Red Active Galactic Nuclei at 3<z<7 with JWST and ALMA, http://arxiv.org/abs/2306.07320

Lagache G., Cousin M., Chatzikos M., 2017, Astronomy & Astrophysics, Volume 609, id.A130, <NUMPAGES>19</NUMPAGES> pp., 609, A130

Langeroodi D., et al., 2022, arXiv, p. arXiv:2212.02491

Laporte N., et al., 2017, The Astrophysical Journal, 837, L21

Laporte N., Meyer R. A., Ellis R. S., Robertson B. E., Chisholm J., Roberts-Borsani G. W., 2021, Monthly Notices of the Royal Astronomical Society, 505, 3336

Lara-López M. A., et al., 2010, Astronomy and Astrophysics, 521, L53

Larson R. B., Larson B. R., 1974, MNRAS, 169, 229

Larson R. L., et al., 2023, ApJL, 953, L29

Latif M. A., Whalen D., Khochfar S., 2022, The Astrophysical Journal, 925, 28

Le Fèvre O., et al., 2020, Astronomy & Astrophysics, 643, A1

Lee M. M., et al., 2021, The Astrophysical Journal, 913, 41

Lemaux B. C., et al., 2014, Astronomy and Astrophysics, 572, A90

Li Y.-P., et al., 2018, The Astrophysical Journal, 866, 70

Li Q., Narayanan D., Davé R., 2019, Monthly Notices of the Royal Astronomical Society, 490, 1425

Li J., et al., 2020, The Astrophysical Journal, 900, 131

Li J. T., Wang F., Yang J., Bregman J. N., Fan X., Zhang Y., 2021, Monthly Notices of the Royal Astronomical Society, 504, 2767

Li Z., et al., 2022, The Astrophysical Journal Letters, 929, L8

Liang Y. C., Yin S. Y., Hammer F., Deng L. C., Flores H., Zhang B., 2006, The Astrophysical Journal, 652, 257

Lilly S. J., Carollo C. M., Pipino A., Renzini A., Peng Y., 2013, ApJ, 772, 119

Lin Y., Zu Y., 2023, Monthly Notices of the Royal Astronomical Society, 521, 411

Lin C.-H., Chen K.-J., Hwang C.-Y., Lin C.-H., Chen K.-J., Hwang C.-Y., 2023, ApJ, 952, 121

Liu B., Bromm V., 2022, The Astrophysical Journal Letters, 937, L30

Liu Y., Jiang D. R., Gu M. F., 2005, ApJ, 637, 669

Liu H.-Y., Liu W.-J., Dong X.-B., Zhou H., Wang T., Lu H., Yuan W., 2019, The Astrophysical Journal Supplement Series, 243, 21

Loiacono F., et al., 2021, Astronomy and Astrophysics, 646, A76

López I. E., et al., 2023, Astronomy and Astrophysics, 672, A137

Lu N., et al., 2018, ApJ, 864, 38

Lu T.-Y., et al., 2022, MNRAS, 517, 1264

Lu J., Shen S., Yuan F.-T., Zeng Q., 2023, The Astrophysical Journal Letters, 946, L7

Ly C., Malkan M. A., Rigby J. R., Nagao T., Bian F., Kewley L. J., Dopita M. A., Blanc G. A., 2017, ApJ, 834, 51

Lynden-Bell D., 1969, Nature 1969 223:5207, 223, 690

Ma X., Hopkins P. F., Faucher-Giguère C. A., Zolman N., Muratov A. L., Kereš D., Quataert E., 2016, Monthly Notices of the Royal Astronomical Society, 456, 2140

Ma X., et al., 2019, Monthly Notices of the Royal Astronomical Society, 487, 1844

Madau P., Dickinson M., 2014, Annual Review of Astronomy and Astrophysics, 52, 415

Madau P., Haardt F., 2015, Astrophysical Journal Letters, 813, L8

Magorrian J., et al., 1998, The Astronomical Journal, 115, 2285

Maier C., Lilly S. J., Carollo C. M., Meisenheimer K., Hippelein H., Stockton A., 2005, ApJ, 639, 858

Maiolino R., Mannucci F., 2019, The Astronomy and Astrophysics Review, 27, 3

Maiolino R., et al., 2015, Monthly Notices of the Royal Astronomical Society, 452, 54

Maiolino R., et al., 2023a, JADES. The diverse population of infant Black Holes at 4<z<11: merging, tiny, poor, but mighty, http://arxiv.org/abs/2308.01230

Maiolino R., et al., 2023b, arXiv, p. arXiv:2305.12492

Malhotra S., et al., 1997, ApJL, 491, L27

Mannucci F., et al., 2009, Monthly Notices of the Royal Astronomical Society, 398, 1915

Mannucci F., Cresci G., Maiolino R., Marconi A., Gnerucci A., 2010, Monthly Notices of the Royal Astronomical Society, 408, 2115

Mao Y. W., Kong X., Lin L., 2014, Astrophysical Journal, 789, 76

Marassi S., Schneider R., Limongi M., Chieffi A., Bocchio M., Bianchi S., 2015, Monthly Notices of the Royal Astronomical Society, 454, 4250

Marconi A., Hunt L. K., 2003, The Astrophysical Journal, 589, L21

Marrone D. P., et al., 2018, Nature, 553, 51

Marziani P., Sulentic J. W., 2012, New Astronomy Reviews, 56, 49

Matsuura M., et al., 2009, Monthly Notices of the Royal Astronomical Society, 396, 918

Matsuura M., et al., 2019, Monthly Notices of the Royal Astronomical Society, 482, 1715

Matthee J., et al., 2019, The Astrophysical Journal, 881, 124

Matthee J., Mackenzie R., Simcoe R. A., Kashino D., Lilly S. J., Bordoloi R., Eilers A.-C., 2023, The Astrophysical Journal, 950, 67

McCracken H. J., et al., 2012, Astronomy and Astrophysics, 544

McGaugh S. S., McGaugh S. S., 1991, ApJ, 380, 140

McGreer I. D., Mesinger A., D'Odorico V., 2015, Monthly Notices of the Royal Astronomical Society, 447, 499

McMullin J. P., Waters B., Schiebel D., Young W., Golap K., 2007, Astronomical Data Analysis Software and Systems XVI, 376, 127

Merloni A., Heinz S., Di Matteo T., 2003, Monthly Notices of the Royal Astronomical Society, 345, 1057

Merloni A., et al., 2009, ApJ, 708, 137

Mignard F., et al., 2018, Astronomy & Astrophysics, 616, A14

Momcheva I. G., Lee J. C., Ly C., Salim S., Dale D. A., Ouchi M., Finn R., Ono Y., 2013, The Astronomical Journal, 145, 47

Moneti A., et al., 2019, ESO Science Archive Facility - Phase 3 Data Release Description

Moneti A., et al., 2023, VizieR Online Data Catalog, p. II/373

Morishita T., Ichikawa T., Noguchi M., Akiyama M., Patel S. G., Kajisawa M., Obata T., 2015, The Astrophysical Journal, 805, 34

Mortlock D. J., et al., 2011, Nature, 474, 616

Mullaney J. R., et al., 2012, Astrophysical Journal Letters, 753, L30

Nagao T., Maiolino R., Marconi A., Matsuhara H., 2011, Astronomy & Astrophysics, 526, A149

Nagao T., Maiolino R., De Breuck C., Caselli P., Hatsukade B., Saigo K., 2012, Astronomy and Astrophysics, 542, L34

Nakajima K., Ouchi M., 2014, Monthly Notices of the Royal Astronomical Society, 442, 900

Nakajima K., et al., 2023, arXiv, p. arXiv:2301.12825

Narayanan D., et al., 2010, Mon. Not. R. Astron. Soc, 407, 1701

Narayanan D., Davé R., Johnson B. D., Thompson R., Conroy C., Geach J., 2018, Monthly Notices of the Royal Astronomical Society, 474, 1718

Natarajan P., et al., 2023, arXiv, p. arXiv:2308.02654

Neistein E., Netzer H., 2013, Mon. Not. R. Astron. Soc, 000, 1

Netzer H., 2015, https://doi.org/10.1146/annurev-astro-082214-122302, 53, 365

Neufeld D. A., Neufeld A. D., 1991, ApJL, 370, L85

Newville M., Stensitzki T., Allen D. B., Ingargiola A., 2014, LMFIT: Non-Linear Least-Square Minimization and Curve-Fitting for Python, doi:10.5281/ZENODO.11813, https://zenodo.org/record/11813

Nicholls D. C., Kewley L. J., Sutherland R. S., Nicholls D. C., Kewley L. J., Sutherland R. S., 2020, PASP, 132, 033001

Noeske K. G., et al., 2007, The Astrophysical Journal, 660, L43

Noguchi M., 2023, Monthly Notices of the Royal Astronomical Society, 522, 4691

Noll S., Burgarella D., Giovannoli E., Buat V., Marcillac D., Munoz-Mateos J. C., 2009, A&A, 507, 1793

Novak M., et al., 2019, The Astrophysical Journal, 881, 63

Oesch P. A., et al., 2016, The Astrophysical Journal, 819, 129

Ohkubo T., Nomoto K., Umeda H., Yoshida N., Tsuruta S., 2009, Astrophysical Journal, 706, 1184

Omori K. C., Takeuchi T. T., 2022, Astronomy and Astrophysics, 660, A145

Onoue M., et al., 2023, The Astrophysical Journal Letters, 942, L17

Ota K., et al., 2014, Astrophysical Journal, 792

Ouchi M., et al., 2013, The Astrophysical Journal, 778, 102

Pacifici C., et al., 2023, The Astrophysical Journal, 944, 141

Pacucci F., et al., 2023, JWST CEERS & JADES Active Galaxies at z = 4-7 Violate the Local $M_\bullet-M_\star$ Relation at $>3\sigma$: Implications for Low-Mass Black Holes and Seeding Models, doi:10.48550/ARXIV.2308.12331, https://ui.adsabs.harvard.edu/abs/2023arXiv230812331P/abstract

Padilla A. F. R., Wang L., van der Tak F. F. S., Trager S., 2022, Astronomy and Astrophysics

Palay E., Nahar S. N., Pradhan A. K., Eissner W., 2012, Monthly Notices of the Royal Astronomical Society, 423, L35–L39

Pallottini A., Ferrara A., Gallerani S., Salvadori S., D'odorico V., 2014, Monthly Notices of the Royal Astronomical Society, 440, 2498

Pallottini A., et al., 2019, Monthly Notices of the Royal Astronomical Society, 487, 1689

Pallottini A., et al., 2022, Monthly Notices of the Royal Astronomical Society, 513, 5621

Papovich C., Dickinson M., Giavalisco M., Conselice C. J., Ferguson H. C., 2005, The Astrophysical Journal, 631, 101

Papovich C., et al., 2016, Nature Astronomy, 1, 0003

Park D., et al., 2012, Astrophysical Journal, 747, 30

Parlanti E., et al., 2023, GA-NIFS: Early-stage feedback in a heavily obscured AGN at z = 4.76

Pavesi R., et al., 2016, The Astrophysical Journal, 832, 151

Peng C. Y., Ho L. C., Impey C. D., Rix H.-W., 2002, The Astronomical Journal, 124, 266

Peng C. Y., Ho L. C., Impey C. D., Rix H. W., 2010, Astronomical Journal, 139, 2097

Pentericci L., et al., 2016, The Astrophysical Journal, 829, L11

Pereira-Santaella M., Rigopoulou D., Farrah D., Lebouteiller V., Li J., 2017, Monthly Notices of the Royal Astronomical Society, 470, 1218

Pérez-Montero E., Contini T., 2009, Monthly Notices of the Royal Astronomical Society, 398, 949

Péroux C., Howk J. C., 2020, Annual Review of Astronomy and Astrophysics, 58, 363

Perrin M. D., et al., 2012, SPIE, 8442, 84423D

Perrin M. D., Sivaramakrishnan A., Lajoie C.-P., Elliott E., Pueyo L., Ravindranath S., Albert L., 2014, SPIE, 9143, 91433X

Peterson B. M., Peterson M. B., 1993, PASP, 105, 247

Pezzulli E., Valiante R., Schneider R., Pezzulli E., Valiante R., Schneider R., 2016, MNRAS, 458, 3047

Pilyugin L. S., Grebel E. K., Kniazev A. Y., 2014, The Astronomical Journal, 147, 131

Pizzati E., Ferrara A., Pallottini A., Sommovigo L., Kohandel M., Carniani S., 2023, Monthly Notices of the Royal Astronomical Society, 519, 4608

Planck Collaboration et al., 2016, Astronomy & Astrophysics, 594, A13

Poggianti B. M., Barbaro G., Poggianti B. M., Barbaro G., 1997, A&A, 325, 1025

Polimera M. S., et al., 2022, The Astrophysical Journal, 931, 44

Popesso P., et al., 2022, Monthly Notices of the Royal Astronomical Society, 519, 1526

Popping G., Puglisi A., Norman C. A., 2017, Monthly Notices of the Royal Astronomical Society, 472, 2315

Posses A. C., et al., 2023, Astronomy and Astrophysics, 669, A46

Pozzi F., et al., 2021, Astronomy & Astrophysics, 653, A84

Priestley F. D., Arias M., Barlow M. J., De Looze I., 2022, Monthly Notices of the Royal Astronomical Society, 509, 3163

Puertas S. D., Vilchez J. M., Iglesias-Páramo J., Mollá M., Pérez-Montero E., Kehrig C., Pilyugin L. S., Zinchenko I. A., 2022, Astronomy and Astrophysics, 666, A186

Qin J., et al., 2022, Monthly Notices of the Royal Astronomical Society, 511, 765

Queyrel J., et al., 2009, A&A, 506, 681

Ramburuth-Hurt T., et al., 2023, Astronomy and Astrophysics, 672, A68

Ramos Padilla A. F., Wang L., Małek K., Efstathiou A., Yang G., 2022, Monthly Notices of the Royal Astronomical Society, 510, 687

Rauch M., Rauch Michael 1998, ARA&A, 36, 267

Reddy N. A., Topping M. W., Sanders R. L., Shapley A. E., Brammer G., 2023, ApJ, 952, 167

Reines A. E., Volonteri M., 2015, Astrophysical Journal, 813, 82

Rémy-Ruyer A., et al., 2014, Astronomy and Astrophysics, 563, A31

Ren Y. W., et al., 2023, The Astrophysical Journal, 945, 69

Ribeiro B., et al., 2016, A&A, 593, 22

Rigopoulou D., Pereira-Santaella M., Magdis G. E., Cooray A., Farrah D., Marques-Chaves R., Perez-Fournon I., Riechers D., 2018, Monthly Notices of the Royal Astronomical Society, 473, 20

Rivera G. C., et al., 2018, The Astrophysical Journal, 863, 56

Rizzo F., Kohandel M., Pallottini A., Zanella A., Ferrara A., Vallini L., Toft S., 2022, Astronomy & Astrophysics, 667, A5

Rizzo F., et al., 2023, The ALMA-ALPAKA survey I: high-resolution CO and [CI] kinematics of star-forming galaxies at z = 0.5-3.5, http://arxiv.org/abs/2303.16227

Robertson B. E., 2022, Annual Review of Astronomy and Astrophysics, 60, 121

Robertson B. E., Ellis R. S., Furlanetto S. R., Dunlop J. S., 2015, Astrophysical Journal Letters, 802, L19

Robertson B. E., et al., 2023, NatAs, 7, 611

Rodighiero G., et al., 2011, Astrophysical Journal Letters, 739, L40

Rodighiero G., et al., 2015, Astrophysical Journal Letters, 800, L10

Rodríguez-Ardila A., Mazzalay X., 2006, Monthly Notices of the Royal Astronomical Society: Letters, 367, L57

Romano M., et al., 2020, Monthly Notices of the Royal Astronomical Society, 496, 875

Romano M., et al., 2021, Astronomy and Astrophysics, 653, A111

Romano M., et al., 2022, C. Lemaux, 18, 13

Saintonge A., Catinella B., 2022, Annual Review of Astronomy and Astrophysics, 60, 319

Salim S., Boquien M., Lee J. C., 2018, The Astrophysical Journal, 859, 11

Salpeter E. E., Salpeter E. E., 1964, ApJ, 140, 796

Salvadori S., Dayal P., Ferrara A., 2010, Monthly Notices of the Royal Astronomical Society: Letters, 407, L1

Salvaterra R., 2015, Journal of High Energy Astrophysics, 7, 35

Sánchez S. F., et al., 2018, RMxAA, 54, 217

Sanders R. L., et al., 2021, The Astrophysical Journal, 914, 19

Sanders R. L., Shapley A. E., Topping M. W., Reddy N. A., Brammer G. B., 2023, eprint arXiv:2303.08149, p. arXiv:2303.08149

Sassano F., Schneider R., Valiante R., Inayoshi K., Chon S., Omukai K., Mayer L., Capelo P. R., 2021, Monthly Notices of the Royal Astronomical Society, 506, 613

Savaglio S., et al., 2005, ApJ, 635, 260

Schaerer D., Boone F., Zamojski M., Staguhn J., Dessauges-Zavadsky M., Finkelstein S., Combes F., 2015, Astronomy and Astrophysics, 574, A19

Schaerer D., et al., 2020, Astronomy & Astrophysics, 643, A3

Schaerer D., Marques-Chaves R., Barrufet L., Oesch P., Izotov Y. I., Naidu R., Guseva N. G., Brammer G., 2022, Astronomy & Astrophysics, 665, L4

Schawinski K., Thomas D., Sarzi M., Maraston C., Kaviraj S., Joo S.-J., Yi S. K., Silk J., 2007, Mon. Not. R. Astron. Soc, 000, 1

Schmidt M. 1963, Natur, 197, 1040

Schneider R., Omukai K., Inoue A., Ferrara A., 2006, MNRAS, 369, 1437

Schneider R., Valiante R., Ventura P., Agli F. d., Di Criscienzo M., Hirashita H., Kemper F., 2014, MNRAS, 442, 1440

Schneider R., et al., 2023, MNRAS, 000, 1

Schouws S., et al., 2022a, arXiv, p. arXiv:2202.04080

Schouws S., et al., 2022b, The Astrophysical Journal, 928, 31

Schulz S., Popping G., Pillepich A., Nelson D., Vogelsberger M., Marinacci F., Hernquist L., 2020, Monthly Notices of the Royal Astronomical Society, 497, 4773

Scoville N., et al., 2006a, The Astrophysical Journal Supplement Series, 172, 1

Scoville N., et al., 2006b, The Astrophysical Journal Supplement Series, 172, 38

Scoville N., et al., 2016, The Astrophysical Journal, 820, 83

Scoville N., et al., 2017, The Astrophysical Journal, 837, 150

Shakura N. I., Sunyaev R. A., Shakura I. N., 1973, SvA, 16, 756

Shapley A. E., Cullen F., Dunlop J. S., McLure R. J., Kriek M., Reddy N. A., Sanders R. L., 2020, The Astrophysical Journal, 903, L16

Sharda P., et al., 2023, arXiv, 000, arXiv:2303.15853

Shen Y., et al., 2019, The Astrophysical Journal, 873, 35

Shen L., et al., 2022, ApJ, 935, 177

Sherman S., et al., 2020, Monthly Notices of the Royal Astronomical Society, 499, 4239

Sijacki D., Vogelsberger M., Genel S., Springel V., Torrey P., Snyder G. F., Nelson D., Hernquist L., 2015, Monthly Notices of the Royal Astronomical Society, 452, 575

Silk J., Rees M. J., Silk J., Rees M. J., 1998, A&A, 331, L1

Slavin J. D., Dwek E., Jones A. P., 2015, Astrophysical Journal, 803, 7

Smit R., Bouwens R. J., Labbé I., Franx M., Wilkins S. M., Oesch P. A., 2016, The Astrophysical Journal, 833, 254

Somerville R. S., Davé R., 2015, Annual Review of Astronomy and Astrophysics, 53, 51

Sommovigo L., Ferrara A., Pallottini A., Carniani S., Gallerani S., Decataldo D., 2020, Monthly Notices of the Royal Astronomical Society, 497, 956

Sommovigo L., Ferrara A., Carniani S., Zanella A., Pallottini A., Gallerani S., Vallini L., 2021, Monthly Notices of the Royal Astronomical Society, 503, 4878

Sommovigo L., et al., 2022a, MNRAS, 513, 3122

Sommovigo L., et al., 2022b, Monthly Notices of the Royal Astronomical Society, 517, 5930

Sorba R., Sawicki M., 2018, Monthly Notices of the Royal Astronomical Society, 476, 1532

Speagle J. S., Steinhardt C. L., Capak P. L., Silverman J. D., 2014, Astrophysical Journal, Supplement Series, 214

Spilker J. S., et al., 2022, The Astrophysical Journal Letters, 929, L3

Spitoni E., Calura F., Matteucci F., Recchi S., 2010, Astronomy and Astrophysics, 514, A73

Stacey G. J., et al., 1991, ApJ, 373, 423

Stasińska G., Cid Fernandes R., Mateus A., Sodré L., Asari N. V., 2006, Monthly Notices of the Royal Astronomical Society, 371, 972

Steinhardt C. L., et al., 2014, Astrophysical Journal Letters, 791, L25

Steinhardt C. L., et al., 2022, The Astrophysical Journal, 931, 58

Storchi-Bergmann T., Schnorr-Müller A., 2019, Nature Astronomy, 3, 48

Storey P. J., Zeippen C. J., 2000, Monthly Notices of the Royal Astronomical Society, 312, 813

Stott J. P., et al., 2013, Monthly Notices of the Royal Astronomical Society, 436, 1130

Sugahara Y., et al., 2021, The Astrophysical Journal, 923, 5

Suh H., Civano F., Trakhtenbrot B., Shankar F., Hasinger G., Sanders D. B., Allevato V., 2020, The Astrophysical Journal, 889, 32

Sun M., et al., 2015, Astrophysical Journal, 802, 14

Sun F., et al., 2023, ApJ, 953, 53

Sutter J., et al., 2019, The Astrophysical Journal, 886, 60

Suzuki T. L., et al., 2021, The Astrophysical Journal, 908, 15

Tacconi L. J., et al., 2013, Astrophysical Journal, 768

Tacconi L. J., Genzel R., Sternberg A., 2020, Annual Review of Astronomy and Astrophysics, 58, 157

Talia M., Cimatti A., Giulietti M., Zamorani G., Bethermin M., Faisst A., Fèvre O. L., Smolçić V., 2021, The Astrophysical Journal, 909, 23

Tamura Y., et al., 2019, The Astrophysical Journal, 874, 27

Tang M., et al., 2023, MNRAS, 000, 1

Tazaki R., Ichikawa K., 2020, The Astrophysical Journal, 892, 149

The Astropy Collaboration et al., 2022, The Astrophysical Journal, 935, 167

Tielens A. G. G. M., Hollenbach D., Tielens A. G. G. M., Hollenbach D., 1985, ApJ, 291, 747

Torrey P., et al., 2018, Monthly Notices of the Royal Astronomical Society: Letters, 477, L16–L20

Torrey P., et al., 2020, Monthly Notices of the Royal Astronomical Society, 497, 5292

Trebitsch M., et al., 2021, A&A, 653, 154

Tremonti C. A., et al., 2004, ApJ, 613, 898

Treu T., et al., 2023, The Astrophysical Journal Letters, 942, L28

Triani D. P., Sinha M., Croton D. J., Pacifici C., Dwek E., 2020, Monthly Notices of the Royal Astronomical Society, 493, 2490

Trinca A., et al., 2022, cosp, 44, 1828

Tripodi R., et al., 2023, The Astrophysical Journal Letters, 946, L45

Trump J. R., et al., 2011, Astrophysical Journal, 733

Tumlinson J., Peeples M. S., Werk J. K., 2017, Annual Review of Astronomy and Astrophysics, 55, 389

Übler H., et al., 2023, arXiv, p. arXiv:2302.06647

Urquhart S. A., et al., 2022, Monthly Notices of the Royal Astronomical Society, 511, 3017

Urry C. M., Padovani P., 1995, Publications of the Astronomical Society of the Pacific, 107, 803

Vaidya S., Stacey G., Peng B., Ball C., Vaidya S., Stacey G., Peng B., Ball C., 2023, AAS, 55, 277.02

Valentino F., et al., 2020, The Astrophysical Journal, 890, 24

Vallini L., Gallerani S., Ferrara A., Baek S., 2013, Monthly Notices of the Royal Astronomical Society, 433, 1567

Vallini L., Ferrara A., Pallottini A., Gallerani S., 2017, Monthly Notices of the Royal Astronomical Society, 467, 1300

Vanderhoof B. N., et al., 2022, Monthly Notices of the Royal Astronomical Society, 511, 1303

Veilleux S., Maiolino R., Bolatto A. D., Aalto S., 2020, The Astronomy and Astrophysics Review 2020 28:1, 28, 1

Venemans B. P., et al., 2017, The Astrophysical Journal, 851, L8

Vignali C., Mignoli M., Gilli R., Comastri A., Iwasawa K., Zamorani G., Mainieri V., Bongiorno A., 2014, Astronomy and Astrophysics, 571

Vijayan A. P., Clay S. J., Thomas P. A., Yates R. M., Wilkins S. M., Henriques B. M., 2019, Monthly Notices of the Royal Astronomical Society, 489, 4072

Vika M., Bamford S. P., Häußler B., Rojas A. L., Borch A., Nichol R. C., 2013, Monthly Notices of the Royal Astronomical Society, 435, 623

Villarroel B., Korn A., Matsuoka Y., Villarroel B., Korn A., Matsuoka Y., 2012, arXiv, p. arXiv:1211.0528

Vincenzo F., Belfiore F., Maiolino R., Matteucci F., Ventura P., 2016, Monthly Notices of the Royal Astronomical Society, 458, 3466

Virtanen P., et al., 2020, Nature Methods 2020 17:3, 17, 261

Vizgan D., Heintz K. E., Greve T. R., Narayanan D., Davé R., Olsen K. P., Popping G., Watson D., 2022, Investigating the [C$\,{\rm \scriptsize II}$]-to-H$\,{\rm \scriptsize I}$ conversion factor and the H$\,{\rm \scriptsize I}$ gas budget of galaxies at $z\approx 6$ with hydrodynamical simulations, http://arxiv.org/abs/2210.03584

Volonteri M., Dubois Y., Pichon C., Devriendt J., 2016, Monthly Notices of the Royal Astronomical Society, 460, 2979

Wang J. M., et al., 2014, Astrophysical Journal, 793, 108

Wang T., et al., 2019, Nature, 572, 211

Wang F., et al., 2021, The Astrophysical Journal Letters, 907, L1

Wang K., Wang X., Chen Y., 2023, ApJ, 951, 66

Watson D., 2011, Astronomy & Astrophysics, 533, A16

Watson D., Denney K. D., Vestergaard M., Davis T. M., 2011, Style (DeKalb, IL), p. 5

Watson D., Christensen L., Knudsen K. K., Richard J., Gallazzi A., Michałowski M. J., 2015, Nature, 519, 327

Whitler L., Endsley R., Stark D. P., Topping M., Chen Z., Charlot S., 2022, Monthly Notices of the Royal Astronomical Society, 519, 157

Willott C. J., Carilli C. L., Wagg J., Wang R., 2015, Astrophysical Journal, 807

Wise J. H., Regan J. A., O'Shea B. W., Norman M. L., Downes T. P., Xu H., 2019, Nature, 566, 85

Wiseman P., Schady P., Bolmer J., Krühler T., Yates R. M., Greiner J., Fynbo J. P., 2017, Astronomy and Astrophysics, 599, A24

Witstok J., et al., 2022, Monthly Notices of the Royal Astronomical Society, 515, 1751

Witstok J., et al., 2023a, arXiv, p. arXiv:2302.05468

Witstok J., et al., 2023b, arXiv, p. arXiv:2306.04627

Wolfire M. G., et al., 1995, ApJ, 443, 152

Wolfire M. G., Vallini L., Chevance M., 2022, Annual Review of Astronomy and Astrophysics, 60, 247

Wong Y. H. V., et al., 2022, The Astrophysical Journal, 929, 161

Wu Y.-Z., Zhang S.-N., Zhao Y.-H., Zhang W., 2016, MNRAS, 457, 2929

Wuyts S., et al., 2012, Astrophysical Journal, 753, 114

Yabe K., et al., 2015, Publications of the Astronomical Society of Japan, 67, 102

Yajima H., Li Y., Zhu Q., Abel T., Gronwall C., Ciardullo R., 2012, The Astrophysical Journal, 754, 118

Yan L., et al., 2020, ApJ, 905, 147

Yang S., Lidz A., 2020, Monthly Notices of the Royal Astronomical Society, 499, 3417

Yang S., Lidz A., Popping G., 2021, Monthly Notices of the Royal Astronomical Society, 504, 723

Yao Y., et al., 2022, The Astrophysical Journal, 926, 57

Yoshida N., Omukai K., Hernquist L., 2008, Science, 321, 669

Zafar T., Watson D., 2013, Astronomy & Astrophysics, Volume 560, id.A26, NUMPAGES7/NUMPAGES pp., 560, A26

Zanella A., et al., 2018, Monthly Notices of the Royal Astronomical Society, 481, 1976

Zaritsky D., Kennicutt Robert C. J., Huchra J. P., Zaritsky D., Kennicutt Robert C. J., Huchra J. P., 1994, ApJ, 420, 87

Zavala J. A., et al., 2021, The Astrophysical Journal, 909, 165

Zavala J. A., et al., 2023, The Astrophysical Journal Letters, 943, L9

Zhang Z.-Y., et al., 2018, Monthly Notices of the Royal Astronomical Society, 481, 59

Zhang T. C., Guo Q., Qu Y., Gao L., 2021, Research in Astronomy and Astrophysics, 21, 212

Zhu B., et al., 2023, MNRAS, 524, 5787

de Graaff A., et al., 2023, Ionised gas kinematics and dynamical masses of $z\gtrsim6$ galaxies from JADES/NIRSpec high-resolution spectroscopy, http://arxiv.org/abs/2308.09742

den Brok J. S., et al., 2020, Monthly Notices of the Royal Astronomical Society, 495, 1874

# Thesis Acknowledgements

I am extremely grateful to my supervisor Darach Watson for his kindness, patience, and invaluable guidance over the last 5 years.

I am also immensely thankful to Gabriel Brammer for always entrusting me with new opportunities, and for helping me whenever I needed it.

I sincerely thank my supervisors at ESO, Gergö Popping and Michele Ginolfi for their constant encouragement and mentorship.

I extend my sincere gratitude to Guarn, Helena, Francesca, Victoria, Charlotte, Sune, Johan, Charles, Peter, Kasper, my fellow PhD students Clara, Kate, Vadim, Natalie, Dazhi, Guozhen, Albert, and Ting-Yi, and everyone else in the DAWN team, who were always there to support me in any way they could.

I am truly grateful for my time at ESO with Ivanna, Joshua, Tony, and the wonderful GESO team.

I also thank all my international collaborators, including Francesco Valentino, Seiji Fujimoto, Luca Di Mascolo, Yuichi Harikane, Michele Cirasuolo, for teaching me how to be part of a team.

Finally, I am grateful to my family who stood by me every step of the way - my Dad with his guidance and encouragement, my Sister with her constant support, reassurance, and faith in my abilities, and my Mom with her infinite patience, understanding, and optimism.